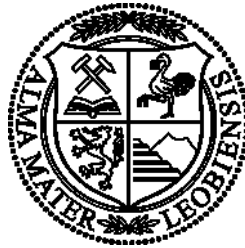# Master Thesis

Polymer Injection into Horizontal Wells, Effects on Injectivity and Sweep Efficiency

Montanuniversität Leoben

Department of Petroleum Engineering

Written by:
Solomon Ofori, BSc
Department of Reservoir
Engineering

University Advisor:
Univ.-Prof. Dipl.-Phys. Dr.rer.nat. Holger Ott
Industrial Advisor:
Dipl.-Ing. Dr. Torsten Clemens
Dipl.-Ing. Dr. Martin Sieberer

Leoben, March 2017

EIDESSTATTLICHE ERKLÄRUNG

Ich erkläre an Eides statt, dass ich die vorliegende Diplomarbeit selbständig und ohne fremde Hilfe verfasst, andere als die angegebenen Quellen und Hilfsmittel nicht benutzt und die den benutzten Quellen wörtlich und inhaltlich entnommenen Stellen als solche erkenntlich gemacht habe.

Leoben, March 2017　　　　　Solomon Ofori

AFFIDAVIT

I hereby declare that the content of this work is my own composition and has not been submitted previously for any higher degree. All extracts have been distinguished using quoted references and all information sources have been acknowledged.

Leoben, March 2017   Solomon Ofori

Acknowledgement

Kurzfassung

Die Ausbeutung von Erdöl mittels Polymerinjektion ist eine Methode, um die Erdölproduktion zu steigern. Bedingt durch die hohe Viskosität der Polymer–Wasserlösung ist eine hohe Verdrängung des Öls in der Lagerstätte gegeben. Das niedrige Mobilitätsverhältnis, das zwischen der Polymer–Wasserlösung und dem Öl entsteht, erzeugt eine stabilere Verdrängungsfront im Vergleich zur Wasserinjektion. Injektionen die in horizontale Bohrungen erfolgen, haben einen nachweisbar besseren Wirkungsgrad, als Injektionen durch vertikale Bohrungen. Eine horizontale Bohrung erlaubt höhere Fließraten in die Lagerstätte, welche bei vertikalen Bohrungen nicht möglich sind.

Der erste Teil der Arbeit befasst sich mit der Injektion von Polymer – Wasserlösungen durch die Bohrung in die Formation, während sich der zweite Teil auf die optimale Anordnung der Bohrungen konzentriert, um den Wirkungsgrad zu optimieren. Die Untersuchungen im ersten Teil sind notwendig, weil sich die Viskosität der Polymere als Nichtnewtonsche Fluide, ungleich Newtonsche Fluide, mit zunehmender Darcy Geschwindigkeit ändert. Die untersuchten Druckverluste in der horizontalen Bohrung und in der Formation sind im Vergleich zum Injektionsdruck vernachlässigbar klein. Die berechneten Darcy Geschwindigkeiten sind weit unter der Geschwindigkeit, bei der die Polymere zersetzen würden weshalb es zu keiner signifikanten Polymerbeschädigung in der unmittelbaren Umgebung des Bohrlochs kommt.

Im zweiten Teil werden die Bohrlängen und Abstände zwischen den Bohrungen variiert und die daraus resultierende inkrementelle Ölproduktion zwischen Polymerflutung und Wasserflutung bewertet. Es wurden sowohl für homogene als auch für heterogene Lagerstättenmodelle Simulationen durchgeführt. Diese Untersuchungen sind notwendig um die Größe der Injektionsgeometrie, Chemically Affected Reservoir Volume (CARV), zu optimieren. Die Größe der Injektionsgeometrie ist wesentlich, da sie nicht nur das Ölproduktionsvolumen beeinflusst sondern auch die wirtschaftlichen Aspekte. Die wirtschaftliche Bewertung anhand der Ergebnisse der homogenen Simulationen, befasst sich mit Faktoren für den Investitionsaufwand der Bohrung und der Komplettierung sowie für den Betriebsaufwand aus den Polymerkosten. Werden die technischen Kosten auf den diskontierten inkrementellen Barrel Ölproduktion bezogen, ergibt sich eine optimale Bohrlochlänge.

Die Ergebnisse der homogenen und heterogenen Simulationen ergeben, dass die Polymer–Wasserlösung eine stabile Verdrängungsfront erzeugt, die für einen besseren Wirkungsgrad sorgt. Ergebnisse der Simulationen zeigen auch, dass größere CARV über kleinere bevorzugt werden sollten, da bei diesen Geometrien die inkrementelle Ölproduktion höher ist. Bei den heterogenen Lagerstätten wird eine höhere inkrementelle Ölproduktion bei Modellen mit Variograms perpendikular zu den Bohrungen erzielt.

Abstract

Polymer injection as a tertiary EOR method has been carried out in both, vertical and horizontal wells, to improve oil recovery because of its lower mobility ratio. The advantages of horizontal polymer flooding seem to outweigh those of vertical wells. It has been shown, that polymer flooding in horizontal wells allows higher injection rates and injection under matrix conditions, which is more difficult to achieve in vertical wells. These advantages have shown that polymer injection into horizontal wells can significantly improve incremental oil production – by enhancing the sweep efficiency – as compared to vertical wells.

Polymers being non-Newtonian fluids, thus having a non-linear shear stress and shear rate relationship, undergo shear thinning or shear thickening at high Darcy velocities, which affects their effectiveness. In this respect, the first part of this thesis is devoted to the investigation of the polymer rheology as it flows through the liner slots into the formation – hence injectivity investigations. The thereby considered parameters include the pressure losses that occur in the horizontally lying liner and the Darcy velocities encountered in the liner slots as well as during radial flow of the polymer solution into the near wellbore region. The results reveal an insignificant frictional pressure drop along the horizontal wells and the velocities at which polymer degradation would occur were not reached.

The second part of this thesis concentrates on the evaluation of cumulative incremental oil recovery at different well spacings and well lengths of horizontal wells from homogeneous and heterogeneous reservoir models. It is necessary to investigate this matter in order to optimise the size of the injection and production pattern i.e. the chemically affected reservoir volume (CARV). The size of the pattern has a major importance on the economics because this determines for example, the operational expenditure (opex) arising from the costs of polymers and the capital expenditure (capex) arising from the drilling and completion costs. Hence, the technical costs, which when set in relation to the discounted cumulative incremental barrels of oil produced, yield the unit technical cost and an optimum well length. The utility factor of each model is calculated and compared to the injection duration.

The results of the homogeneous and heterogeneous simulations indicate that polymer solutions create a stable flooding front accounting for the better sweep efficiency as compared to water flooding. From the homogeneous simulations, the results showed that lager CARV should be preferred over smaller ones. In the heterogeneous models, the variograms with their azimuths perpendicular to the wells had higher incremental oil production.

Table of Content

Page

List of Figures

List of Tables

Abbreviations

1D	1 – Dimensional
3D	3 – Dimensional
CAPEX	Capital Expenditure
CARV	Chemically Affected Reservoir
EOR	Enhanced Oil Production
FV	Future Value
HPAM	Hydrolysed Polyacrylamide
IFT	Interfacial Tension
OPEX	Operational Expenditure
PV	Pore Volume
UF	Utility Factor
UTC	Unit Technical Costs

Chapter 1:   Introduction

Reservoir management aims at improving the profitability of a reservoir. The rate of return on investment is used to appraise the project and as the petroleum production industry has little control on the price of oil and gas, operators are left with the option of enhancing profit by minimizing costs of producing a barrel of oil. This therefore calls for the need to optimize production from discovered fields to stay competitive. Using horizontal wells in enhanced oil recovery (EOR) can help to achieve this goal. Many horizontal well projects worldwide have confirmed their effectiveness in injection rates as well as in increasing production, leading to better performances in enhancing reserves (Joshi and Ding, 1996).

Horizontal wells are now not only used as production wells but also used in EOR applications due to their advantages over vertical wells. They have been applied in EOR applications like thermal oil recovery (Joshi, 1991), and also in miscible CO_2 floods where excellent results have been achieved. Water flooding has also shown great potential when applied in horizontal wells (Lacy et al., 1992). The key advantages of horizontal wells over vertical wells include improved sweep efficiency, enhanced producible reserves, and a decrease in the number of vertical wells. According to Joshi, (1991) a horizontal well of 600 to 1200 m can replace several vertical wells and its main disadvantage is the initial cost.

In injectivity investigations of horizontal wells, Taber and Seright (1992) suggest, that horizontal wells can increase injectivity by a factor of ten depending on the well spacing and the thickness of the formation compared to a five spot pattern of a vertical well configuration. They declare that, due to the improved areal sweep efficiencies, higher flooding rates and lower injection pressures are possible. Therefore, horizontal wells should be beneficial for all EOR methods. Furthermore, they state that for a given injection pressure, the pressure gradient in the bulk of the reservoir can average up to numerous times higher than vertical wells, when using horizontal wells which in the case of micellar or polymer flooding could significantly improve microscopic displacement efficiencies (Taber and Seright, 1992). Another advantage of horizontal wells over vertical wells is the enhancement of the injection rates in injection wells because of the large contact area of the horizontal well (Joshi, 1991).

Because of these above-mentioned benefits of horizontal wells, OMV AG is planning a polymer flooding pilot project using horizontal wells. In this research, I aim at combining the advantages of horizontal wells with those of polymers through a series of simulations to increase recovery efficiency. According to Clemens et al. (2010), the main objective of polymer flooding is to increase the viscosity of the injected water by adding water soluble polymer. The increase in viscosity leads to a reduced frontal

mobility ratio between the polymer displacing fluid and the oil and consequently improving the in-situ sweep efficiency (Clemens et al., 2010).

Owing to the fact that polymer solutions are non-Newtonian time-dependent viscous fluids, the injectivity of the fluid has to be investigated. I have therefore divided this thesis into two parts. In the first part, I am going to examine the injectivity of the polymer solution, whereby issues such as pressure drop in the liner along the horizontal wellbore and shear rate of the polymer flowing through the liner slots into the formation are going to be investigated. Furthermore, the radial inverse drawdown pressure around the wellbore is also tackled and examined. In the second part, my aim is to tackle the efficiency of oil recovery in respect to spacing and length of horizontal wells to find out an optimal well geometry. Finally, from the results of the simulation I am going to consider the economic aspects of the project such as present value (PV), operating expenditure (opex), capital expenditures (capex) and unit technical costs (UTC).

Chapter 2:   Polymer Solution Injectivity Analysis

This thesis discusses the flow of polymer fluid, i.e. non-Newtonian fluid, through the horizontal section of the wellbore into the formation. This part focusses on the pressure losses in the pipe, i.e. in the liner, and the inverse drawdown pressure as the fluid moves into the formation. The thereby changes in the apparent viscosity due to flow velocity of the polymer solution in the liner and the associated shear rate at which polymer degradation may occur as the fluid moves through the liner slots into the formation are also taken into account. Whilst in the liner, the flow of the fluid can be treated as flow through pipes, hence internal flow, the flow of the fluid from the liner slots into the formation may be classified as radial flow. The pressure losses in the pipe is best described as the sum of the losses resulting from gravity, friction and acceleration. Radial flow on the other hand is best described using the Darcy equation for the radial flow.

According to Joshi (1991), if the pressure drop along the wellbore compared to the inverse drawdown pressure of the reservoir is very small it can be ignored. The horizontal well in this case can be considered as an infinite – conductivity wellbore. He further expresses that high flow rates or high viscous fluids can lead to higher pressure drops along the wellbore. This would lead to changes in inverse drawdown pressure and would consequently lead to a decrease in injectivity. He therefore suggests that an optimum well length can be calculated to overcome high pressure drops or by making sure that flow is in laminar regime by regulating the flow rate through a larger hole size (Joshi, 1991 p. 380).

The above-described sequences can be schematically seen in Figure 1.
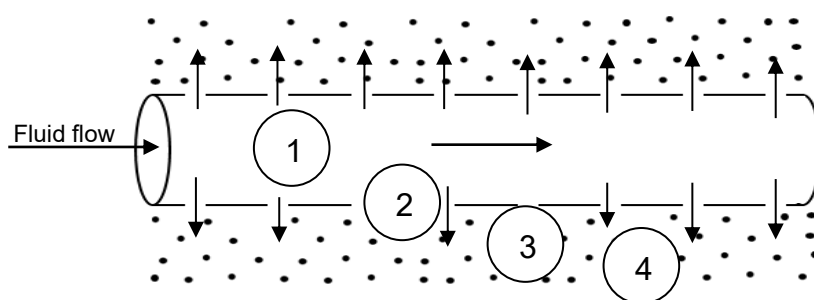
1 → Pressure drop in horizontal well.
2 → Polymer degradation in liner slots.
3 → Polymer degradation in near wellbore region.
4 → Influx into the formation.

Figure 1: Scope of investigations

2.1 Pressure Drop in the Liner

In the horizontal section of the wellbore, the losses in pressure are predominantly caused by the friction between the fluid and the walls of the liner. It is therefore necessary to know the pressure drop along the pipe in order to be able to design the pumps necessary for the injection of the fluid into the wellbore. The pressure drop is calculated for a liner length of 500 m with different flow rates ranging from 200 to 500 m³/day. It is assumed that the flow rate decreases linearly with distance and is zero at the toe of the horizontal well, thus zero flow rate at the toe as shown in schematically in Figure 2. In calculating the pressure losses, fluid properties like density and dynamic viscosity are necessary to compute the Reynolds number.
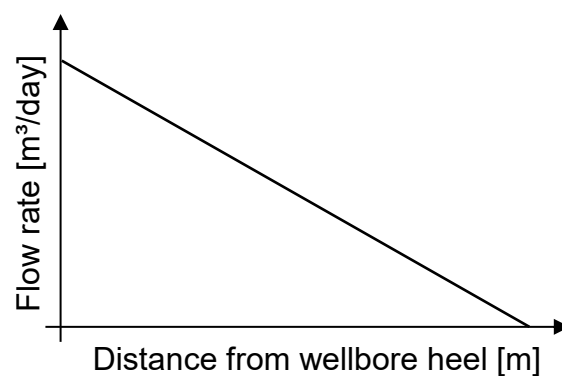
Figure 2: Flow rate decline with well distance from heel to toe

The Reynolds number expresses a relationship between inertia and viscous forces and is used to characterize flow regimes. In the following calculations, a Reynold Number below 2100 (Vlachopoulos, 2016 p. 1) is said to be laminar, whilst above 4000 is said to be turbulent. In between laminar and turbulent, the flow is in a transition zone. Figure 3 shows the velocity profile of the flow through a pipe for laminar (a) and that of turbulent regime (b). In the laminar flow regime, the fluid moves in an orderly manner whilst the flow of turbulent fluid is highly chaotic and disturbed making it difficult to predict the flow path of the particles (Khan, 2015 p. 281).
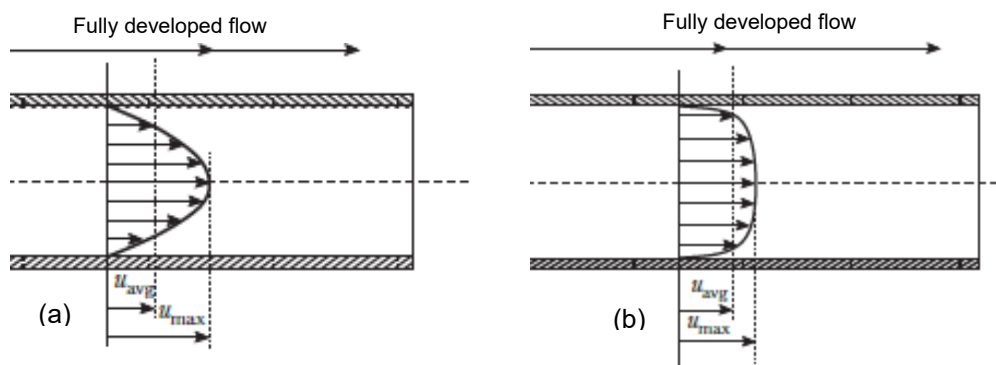
Figure 3: Flow inside a pipe: laminar (a), turbulent (b). (Vlachopoulos, 2016)

The pressure drop along the horizontal well, represented as a horizontally lying pipe can be calculated using the laws of conservation, mass momentum und energy, as shown in equation 1 (Joshi, 1991 p. 389),

$$\frac{dp}{dl} = \left(\frac{dp}{dl}\right)_{gravity} + \left(\frac{dp}{dl}\right)_{friction} + \left(\frac{dp}{dl}\right)_{acceleration} \qquad 1$$

where dp is the pressure drop [Pa] and dl the incremental length [m]. Due to the negligible magnitude of the losses from gravity and acceleration, the pressure drop of the fully developed flow of the horizontal section is mainly caused by friction. The resulting equation can be seen in equation 4 (Joshi, 1991 p. 389).

In the injectivity calculations for the pilot project, a 4 ½ inch liner has been planned for the horizontal section. For the earlier mentioned range of flow rates, i.e. 200 – 500 m³/day, the flow velocity (v) in m/s was calculated using equation 2 (Mott and Untener, 2015 p. 119),

$$v = \frac{q}{A} \qquad 2$$

where q is the flow rate [m³/s] and A is the area of the liner [m²]. This velocity corresponds to the Darcy velocity or superficial velocity. Having calculated the flow velocity, the Reynold Number is computed using equation 3 (Vlachopoulos, 2016, p. 1),

$$Re = \frac{\rho . v . d}{\mu} \qquad 3$$

where ρ is the density of the fluid [kg/m³], v the flow velocity [m/s], d the inner-diameter of the liner [m] and μ the viscosity [Pa·s]. The density of the polymer solution is assumed to be 1000 kg/m³ with a viscosity of 6 cp (6 mPa·s). Equation 4, Darcy – Weisbach equation, requires the friction factor (f_D) which is derived either from correlations or from the Moody Diagram using the calculated Reynolds Number and the relative roughness of the liner wall. The pressure drop along the pipe is calculated as follows (Khan, 2015, p. 270):

$$dp = f_D \frac{\rho}{2} \frac{v^2}{d} dl \qquad 4$$

where (f_D) is the dimensionless friction factor. The dimensionless friction factor f_D for laminar flow is calculated using equation 5 which was postulated by Poiseuille and that for turbulent flow using the Colebrook equation as shown in equation 6. While the

Poisueille equation for laminar flow depends solely on the Reynolds Number, the Colebrook equation depends as well on the Reynolds Number and additionally on the relative roughness of the pipe (ε/D) (Saavedra and Reyes, 2001). ε represent the roughness of the inner surface of the specific material and D the inner diameter of the pipe. In these calculations the surface roughness of a smooth steel pipe with ε = 0.1 mm is used.

Laminar flow:
$$f_D = \frac{64}{R_e}$$
5

Turbulent flow: 4000 < Re < $1 \cdot 10^8$ and $1 \cdot 10^8 < \varepsilon/D < 0.1$

Turbulent flow:
$$f_D = \left[1.14 - 2 \log \left[\left(\frac{\varepsilon}{D} \right) + 21.25 \, R_e^{-0.9} \right] \right]^{-2}$$
6

According to Joshi (1991), in the transition region, Moody's friction diagram can be used to calculate the friction factor if there are no given correlations. (Joshi, 1991) However, this diagram can also be used to figure out the friction factor for both the laminar and the turbulent flow as well. This diagram can be seen in the appendix A.

From the results of the above calculations, the highest Reynolds Number is achieved by a flow rate of 500 m³/day and hence the highest pressure drop, whilst the lowest as expected by a flow rate of 200 m³/day. The results can be seen in Figure 4 which illustrates the flow velocity distribution of the fluid linearly in the liner for a constant length of 500 m. A linear flow velocity distribution is experienced. This is because of the assumption of an equal influx along the horizontal well. Hence, the flow rate is zero at the toe of the well.
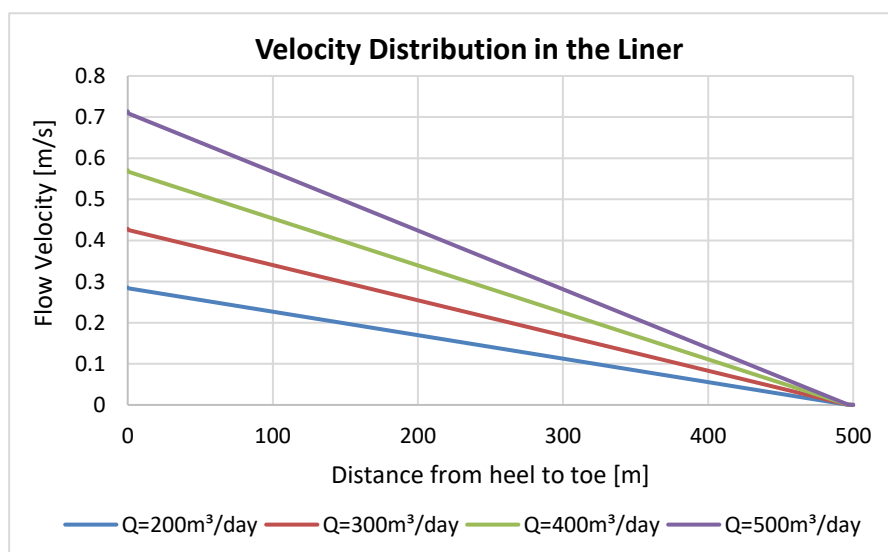
Figure 4: Flow velocity along the liner for equal influx along horizontal well.

Similarly, since Re $\propto$ v, the distribution of the Reynolds Number along the length of the liner also decreases linearly as expected (Figure 5).

Distribution of Reynolds Number in the Liner
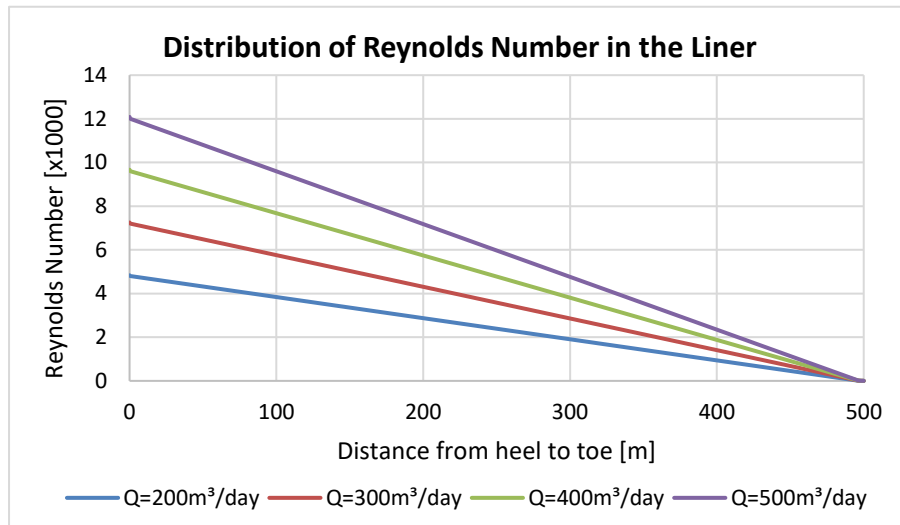
Figure 5: Reynolds Number along the liner for equal influx along horizontal well for different flow rates and 500 m liner.

In Figure 6, the frictional pressure losses along the liner is illustrated. As the Reynolds Numbers calculated ranges from 0.6 for a flow rate of 200 m³/day to 12000 for a flow rate of 500 m³/day, the flow regime stretches across laminar and turbulent. The change of the flow from turbulent to laminar is responsible for the sharp decline or jump in pressure as seen in the Figure 6.

Pressure Drop per Distance
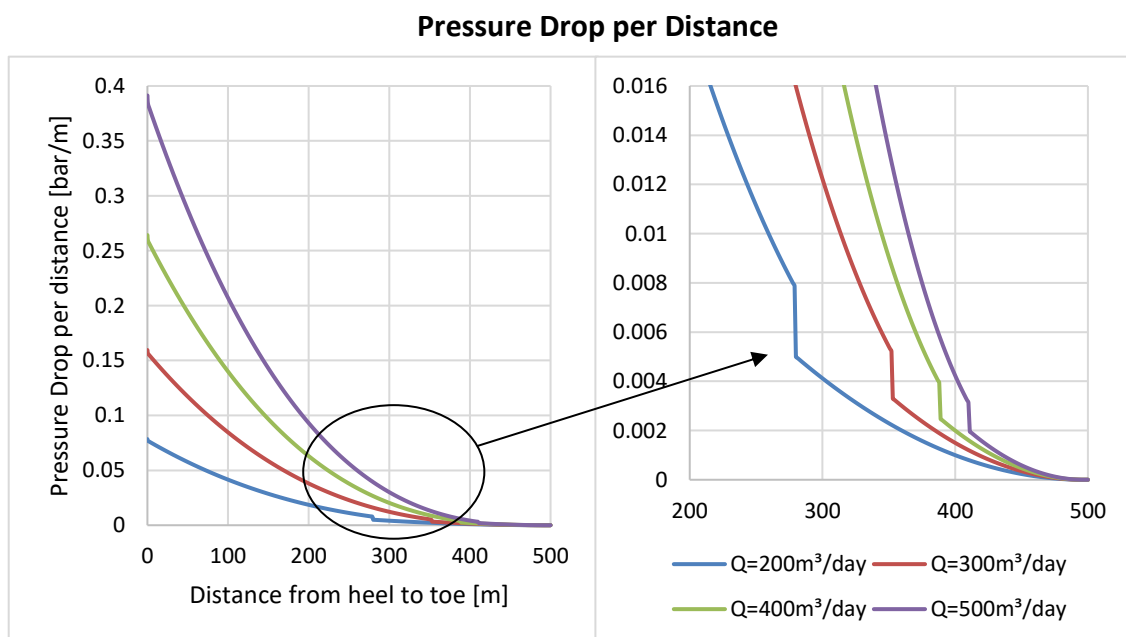
Figure 6: Pressure drop per distance in the liner for different flow rates and 500 m liner.

From equation 4 it can be seen that the pressure drop is proportional to the dimensionless friction factor (f_D) and therefore with the velocity decreasing linearly, the density, liner length and diameter being constant, this sharp jump is caused by the dimensionless friction factor. This is best seen by plotting the dimensionless friction factor against liner length, as illustrated in Figure 7 for a flow rate of 200 m³/day. In reality this jump represent a transition from turbulent into laminar regime. The turbulent flow regime as shown in the plot is on the left and the laminar on the right.
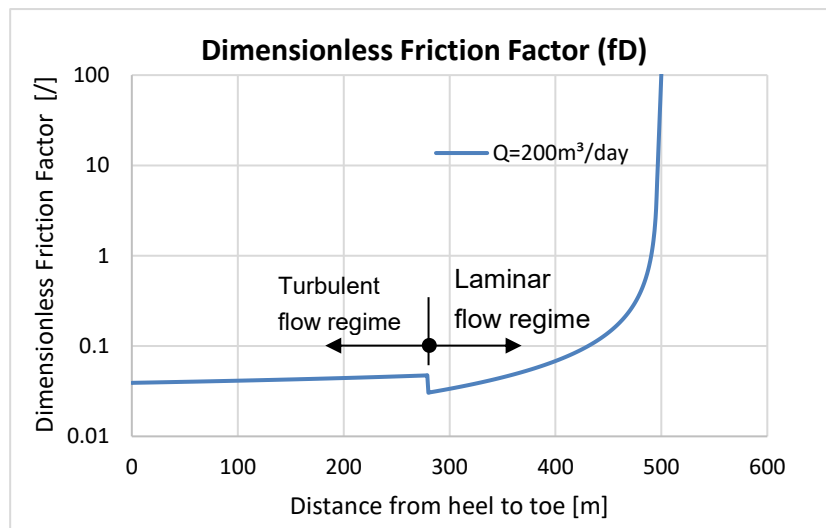
Figure 7: Dimensionless friction factor against liner length for 200 m³/day and 500 m distance from heel

Varying the liner lengths between 500 m and 4 m show a decrease in the friction pressure losses as the length decreases. This is attributed to the fact that dp ∝ dl as seen in equation 4 and the corresponding plot can be seen in Figure 8 for liner lengths of 500, 250, 100, 50 and 4 m for a 200 m³/day injection flow rate.
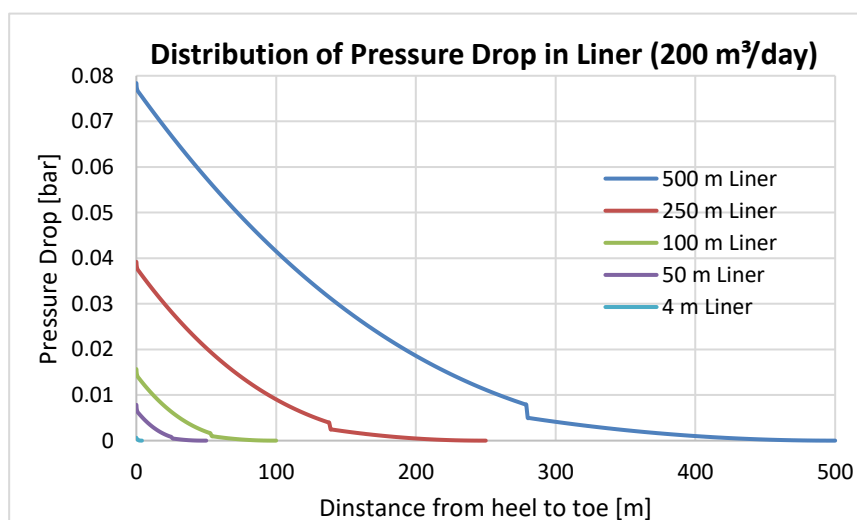
Figure 8: Pressure drop distribution in the liner for different horizontal well

According to Zechner et al., (2013) the current reservoir pressure of the 8th Tortonian reservoir horizon of the Matzen Field is about 102 bar. The polymer injection into this reservoir is planned to be under matrix conditions for horizontal wells. Therefore, comparing the injection pressure of 160 bar, which is below the formation parting pressure of 180 bar, the friction pressure losses in the 500 m liner, which from the calculations is at a maximum of 0.4 bar at an injection rate of 500 m³/day as seen in Figure 6 can be neglected. However, this has to be compared with the inverse drawdown pressure around the wellbore to justify the availability of enough differential pressure.

2.2 Shear Rate in the Liner Slots

This section investigates the mechanical degradation of the polymer in the aqueous solution as it flows through the liner slots into the reservoir. The mechanical deformation can be shear, elongation or a mixture of both caused by shear and strain stresses. Generally, most polymers display a shear thinning – pseudo plastic behaviour – temperature and pressure dependent viscosities leading to loss in viscosity at high rates of deformation. This is because at high deformation rates the molecular chains disentangle, stretch out and slide past each other leading to lower bulk viscosity. Considering the effect of process time on the deformational behaviour of materials a dimensionless number called Deborah number has been introduced. This number is the ratio of the stress relaxation time (λ) of the material to the observation time (t_p) or process time (Osswald and Rudolph, 2015 p. 17). A Deborah number of about zero depict a viscoelastic fluid (non-Newtonian), greater than one to infinity shows an elastic solid and a number below one is liquid-like (Newtonian behaviour) (Goodwin and Hughes, 2008 p. 195).

Polymers, being non-Newtonian fluids follow the power law fluid model, whereby the fluid exhibit either a shear thickening – dilatant – or a shear thinning – pseudoplastic behaviour. Equation 7 describes the power law model showing the relationship between shear stress (τ), shear rate (γ), the consistency index (k) and the power index (n) (Tadros, 2010 p. 42).

$$\tau = k\gamma^n \qquad\qquad\qquad 7$$

 A shear thinning fluid has a power index lower than 1 (n<1) and shear thickening greater than 1 (n>1). The relationship between the apparent viscosity (μ), consistency index, shear rate and the power index is given in equation 8 (Tadros, 2010 p. 42).

$$\mu = \frac{\tau}{\dot{\gamma}} = \frac{k\dot{\gamma}^n}{\dot{\gamma}} = k\dot{\gamma}^{n-1} \qquad\qquad 8$$

Figure 9 illustrates the various curves of fluid models – shear stress against shear rate for shear thinning, shear thickening and Newtonian fluids for (a) purely viscous fluid and (b) viscoplastic fluid. An example of viscoplastic fluid is the Herschel – Bulkley fluid model which describes a power law fluid model possessing a yield point (τ_y).

A Newtonian fluid is described by the shear stress function as can be seen in equation 9, expressing a linear relationship between shear stress and shear rate. Bingham plastic flow model is the simplest viscoplastic model, which behaves as a Newtonian fluid after the yield point has been reached. Equation 10 shows the corresponding function (Irgens, 2014 p. 9).

$$\tau = \mu\dot{\gamma} \qquad\qquad 9$$

$$\tau = \tau_y + \mu\dot{\gamma} \qquad\qquad 10$$
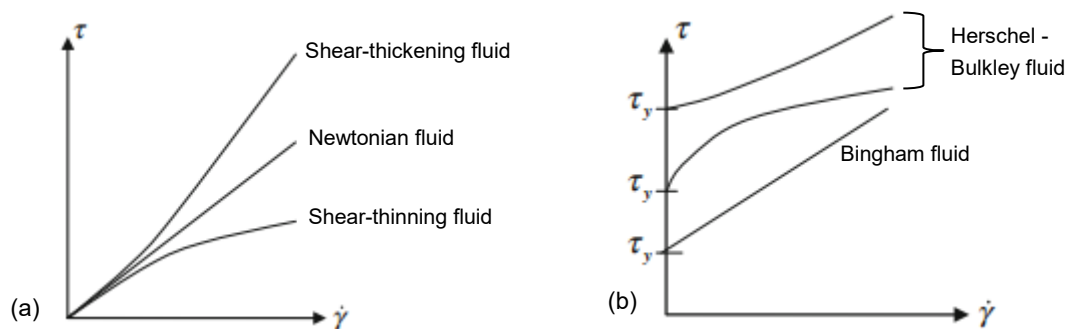
Figure 9 – Viscoelastic (a) and viscoplastic (b) fluid models. (Irgens, 2014)

The shear rate of the polymer across the slots of the liner is calculated by summing up the slots around the liner, making the slots look like a one long rectangular opening, i.e. like a fracture opening, through which the fluid is flowing into the formation. The dimensions of the liner slots can be seen in Figure 10. A slot has a length of 50.8 mm and there are five slots per circumference. This make up a total fracture height or total slot length of 3.34 m per 1 m length of liner. The aperture is 1 mm. From experiments carried out by Wang and Seright (2006), a correlation for the calculation of the shear rate for the power law non-Newtonian fluid as seen in equation 11 was derived. This equation is used to convert the fracture geometry and the fluid velocity into shear rates.

$$\dot{\gamma} = \frac{2n+3}{n+1} \cdot \frac{2q}{h} w^{-\frac{2n+3}{n+1}} (2x)^{\frac{1}{n+1}}$$ 11

$\dot{\gamma}$ is the shear rate [1/s], n is the power index, q is the flow rate [m³/day], h is the height of the fracture [m], w is the aperture of the fracture and *x* is the half-distance between the walls (Wang and Seright). The power index (n = 0.88) of the polymer fluid was provided by Zechner et al. (2013) from their experiments and calculation of pressure drop of non-Newtonian fluid in a fracture.
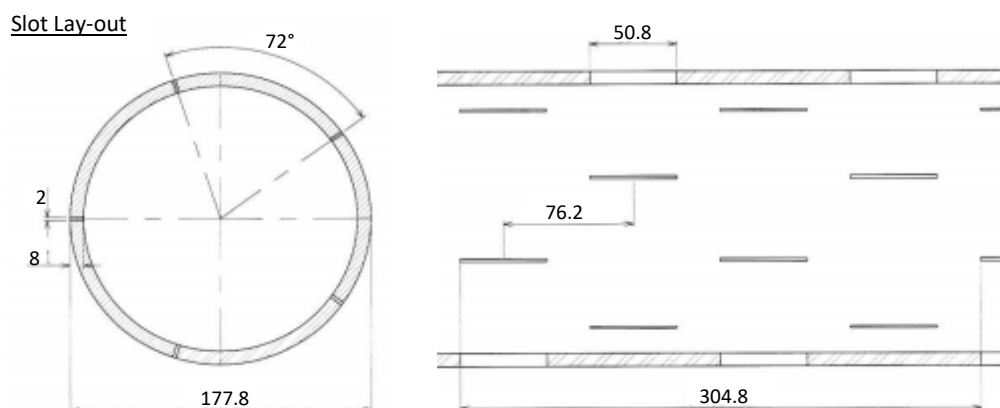
Figure 10: Dimensions of the liner [mm].

From these experiments done by Zechner et al. (2013) they found that polymer degradation for plain fractures, as this is the case of the liner slots, would occur at shear rates above 1000 1/s and at an apparent viscosity of about 4 cp. Calculations for the shear rate is performed for different lengths – effectively contributing part of the horizontal well - to investigate at which effective fracture length and flow rate the polymer is going to degrade. Figure 11 shows the results of the calculations in a form of a plot of the flow rate against the shear rate for flow velocities of 100, 200, 300, 400 and 500 m³/day. The length of the liner is varied from 25 to 500 m. As can be seen in the plot, the lowest shear rates are experienced at lower flow rates of 100 m³/day at a liner length of 500 m. Even at a length of 25 m, the shear rate stays around 175 1/s, which is far below the 1000 1/s degradation rate estimated by Zechner et al. (Zechner et al., 2013).
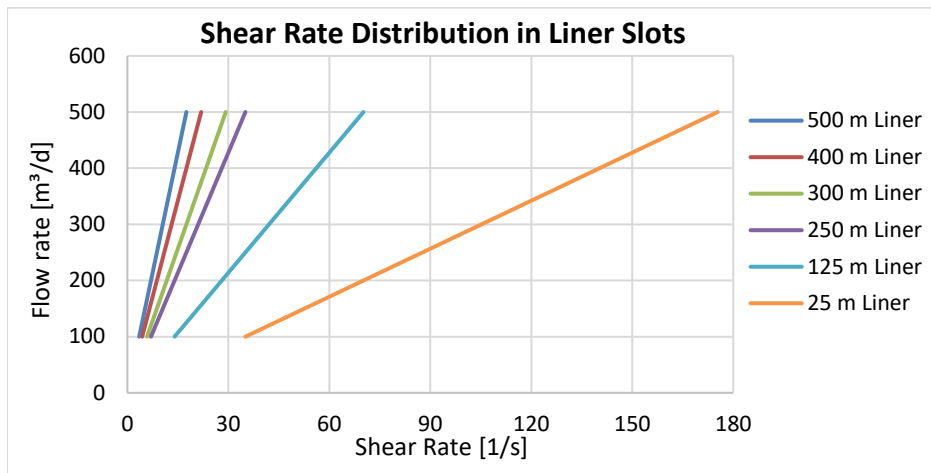
Figure 11: Trend of the shear rate in the liner slots at 500 m³/day flow rate for different liner lengths.

2.3 Radial Inverse Drawdown Pressure in Near Wellbore Region

Ahmed and Mehan (2012) state that the shape of the reservoir has an important effect on the flow behaviour. Mathematical descriptions of irregular boundaries are possible using numerical simulators. They further state that for many reservoir engineering purposes, reservoir geometries are represented either as radial, linear or spherical flow (Ahmed and Meehan, 2012 p. 4). An earlier work of Ahmed expresses flow of fluid into the wellbore as not being linear but more often as radial (Ahmed, 2006 p. 239). As illustrated in Figure 12 and in Figure 13, an idealised radial flow can be seen whereby in the case of inflow, the reservoir pressure p_e is higher than the well flowing pressure p_{wf} allowing the flow of fluid into the wellbore, hence drawdown pressure.
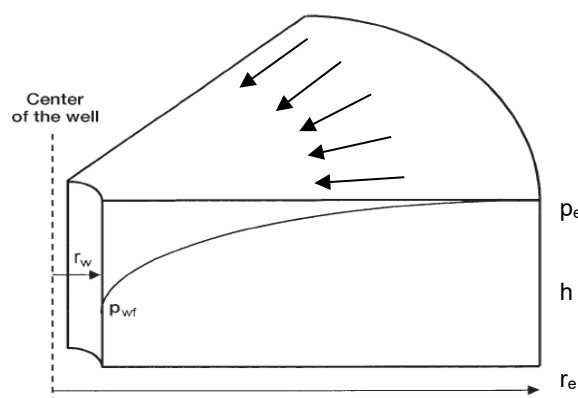
Figure 12: Radial flow model (Ahmed and Meehan, 2012).
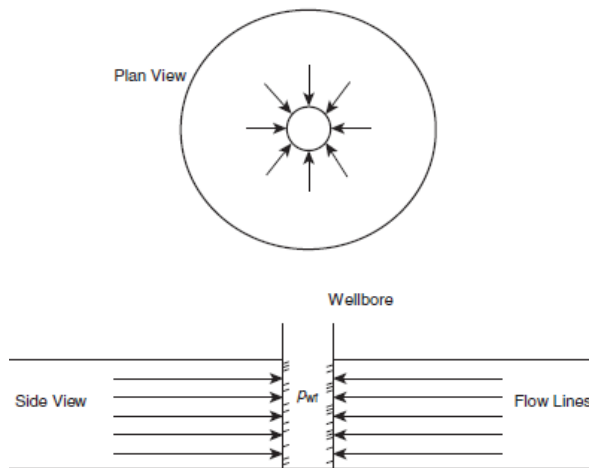
Figure 13: Ideal radial flow into a wellbore (Joshi, 1991 p. 6).

For radial flow the Darcy equation can be used to calculate the drawdown pressure Δp. Equation 12 shows the Darcy equation, which is only valid for steady state flow, i.e. pressure does not change with time, incompressible fluid, i.e. the density of the fluid does not change with pressure and laminar flow. This relationship shows that the drawdown pressure increases with increasing drawdown radius (Ahmed, 2006 p. 240).

$$q = \frac{k\,A}{\mu}\,\frac{dp}{dr}$$

12

q is the flow rate [m³/s], k the permeability, A the area of the curved surface [m²], hence surface area of a cylinder which is $2\pi rh$, μ is the viscosity [Pa·s] and dp/dr mark the radial pressure drawdown. The integrated Darcy equation in computing the pressure is shown in equation 13 (Ahmed, 2006, p. 240)

$$q \int_{r_w}^{r_e} dr = \frac{k\,A}{\mu} \int_{p_{wf}}^{p_e} dp$$

13

Rearranging and solving equation 13 for the drawdown pressure Δp delivers equation 14.

$$\Delta p = q \frac{\mu}{2\pi h\,k} \ln\left(\frac{r_e}{r_w}\right)$$

14

Inversely, during injection, the flow of fluids away from the wellbore into the formation also follow radial flow lines as the fluid moves into all direction. This is also characterized as a radial flow geometry (Ahmed, 2006, p. 337) and as a result the equation of Darcy is valid.

As can be seen from the Darcy equation, the viscosity of the fluid is necessary in calculating the drawdown pressure. Due to the behaviour of polymers undergoing shear thinning at increasing shear stress, the apparent viscosity as a function of the flow rate has to be considered. Gumpenberger et al. (2012) however, have shown in

their core flooding experiments that the apparent viscosity of the polymer solution of partially hydrolysed polyacrylamides (HPAM) – polyacrylic acid copolymer Flopaam – at some point increased with increasing flow rate because of the viscoelastic properties of the polymer before degradation arose. Using two different polymer solution concentrations of 500 and 1000 ppm and varying flow rates, they found that the apparent viscosity increased until a maximum was reached at a specific flow rate and after this, the apparent viscosity started decreasing owing to polymer degradation as shown in Figure 14. Polymer degradation occurred at a Darcy velocity of 18 m/day and 35 m/day for the 1000 and 500 ppm respectively (Gumpenberger et al., 2012).

Thus, the polymer they investigated showed both shear thickening at lower flow rates and degradation at higher flow rates. The decrease in the apparent viscosity with increasing flow rates can be accredited to mechanical polymer degradation. The shear rates at which the polymer starts degrading are typically met in the near-wellbore region during injection. Gumpenberger et al point out in their work that the changes in apparent viscosity is not only a function of flow rate but also depends on the concentration of the solution. This can be seen in the Figure 14 as the maximum apparent viscosity of the polymer solution with a concentration of 1000 ppm is about twice that of the polymer solution with a concentration of 500 ppm, hence the maximum apparent viscosity correlates roughly with polymer concentration. They point out that the reason for this is the longer interaction of the polymer particles at high concentrations as opposed to lower concentrations where there is a reduced polymer particle interaction (Gumpenberger et al., 2012).
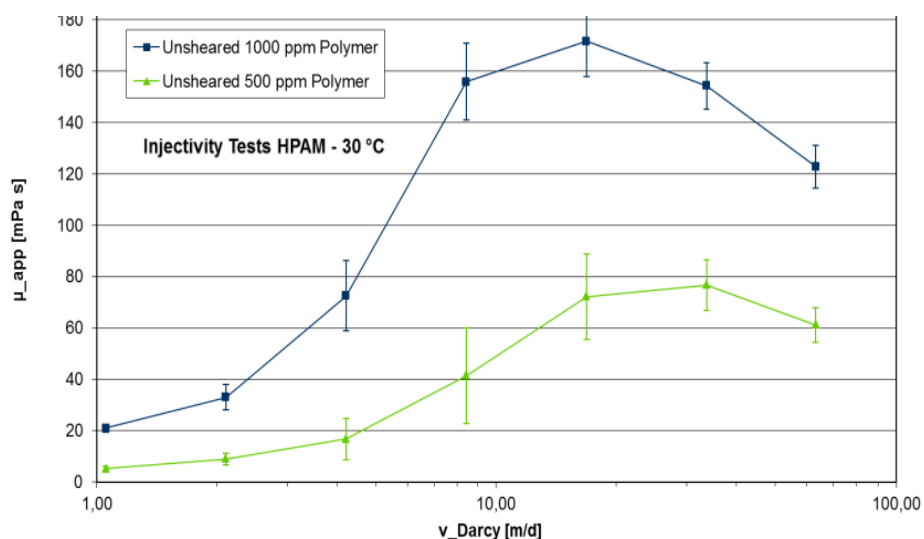
Figure 14: Apparent Viscosity of polymer solution as a function of Darcy velocity (Gumpenberger et al., 2012).

To find out how the apparent viscosity would change as the polymer solution propagates from the near wellbore region into deeper parts of the reservoir, they used

the effluent of the core flooding i.e. presheared polymer solution from different flow rates to investigate this. The effluent polymer solution was then reinjected into a brine-saturated core at flow rates up the flow rate at the time of sampling. In radial geometry the shear rate decreases with r $^{-1}$ as the Darcy velocity also does. Their result, which is shown in Figure 15 illustrates, that presheared polymer solutions at low flow rates, for example at a Darcy velocity of 4 m/d, a significant loss in apparent viscosity can be detected. For higher flow rates, a more pronounced effect can be observed. They propose that the irreversible loss of viscosity can be attributed to physical degradation of the polymer as it moves through constrictions in the pore space (Gumpenberger et al., 2012).
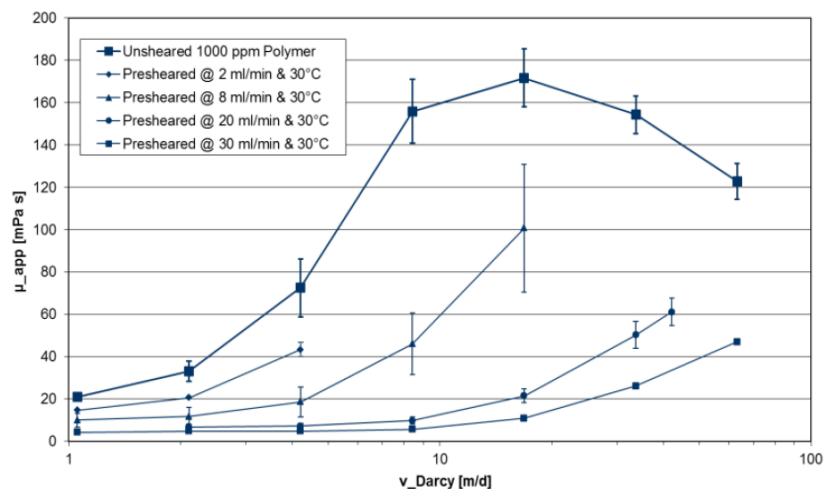
Figure 15: Apparent viscosity of presheared polymer (Gumpenberger et al., 2012).

In the calculation of the radial pressure drawdown, the curve in Figure 14 is fitted for a polymer solution concentration of 800 ppm to achieve the necessary apparent viscosities. In doing so the apparent viscosity curve was broken into six areas in order to describe the curve mathematically. The adapted apparent viscosity curve for 800 ppm polymer solution is illustrated in Figure 16.
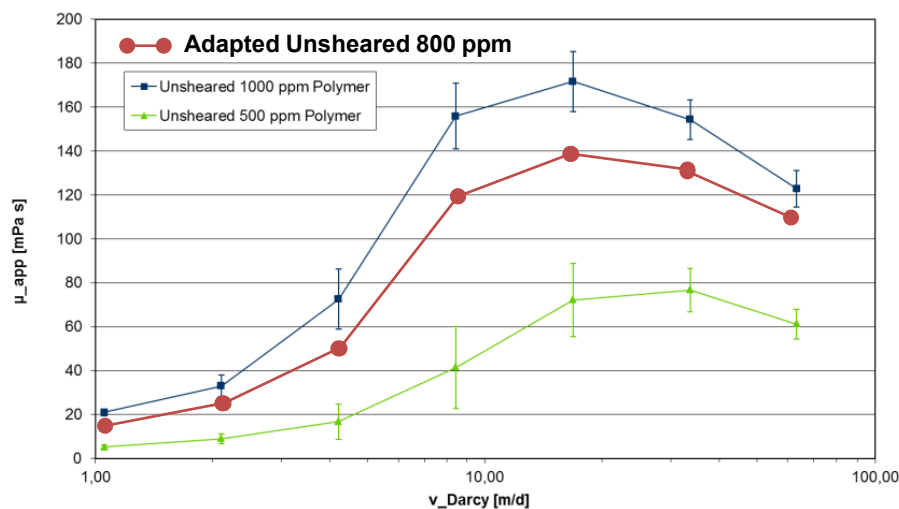
Figure 16: Adapted apparent viscosity curve for 800 ppm polymer concentration (Gumpenberger et al., 2012).

Expressing the curve mathematically, the equations below show the relationship of the apparent viscosity (μ apparent) to the Darcy velocity (v_D) and their corresponding ranges which is only valid for the 800 ppm polymer solution. In the equations y represent the apparent viscosity and x the Darcy velocity. For velocities below 1 m/d, it is assumed that the apparent viscosity stays constant.

v_D < 1: $$y = 18$$ 15

1 < v_D < 4: $$y = 0{,}9278595\, x^2 + 9{,}196284\, x + 7{,}303013$$ 16

4 < v_D < 6: $$y = 6\, x^2 - 49\, x + 159$$ 17

6 < v_D < 10: $$y = 0{,}3781069\, x^2 + 5{,}307962\, x + 35{,}75344$$ 18

10 < v_D < 20.5: $$y = -0{,}1399143\, x^2 + 5{,}723684\, x + 284{,}46344$$ 19

20.5 < v_D < 63: $$y = -0{,}006820119\, x^2 - 0{,}2540494\, x + 151{,}0742$$ 20

Now having fitted the apparent viscosity curve the pressure drop can be calculated. In these calculations, different flow rates are used in the calculation of the pressure drop along the liner in order to have a solid comparison in relating the pressure drop along the horizontal wellbore to the inverse drawdown pressure of the formation, hence 200, 300, 400 and 500 m³/day are the considered flow rates. The investigation of the inverse drawdown pressure is carried out for an outer reservoir radius of 10 m and an inner radius, hence wellbore radius of 0.0762 m (6 inches openhole) as illustrated in Figure 17. The reservoir is estimated to have an average permeability of 1 Darcy. Lengths of the horizontal section considered are 50, 100, 250 and 500 m, whereby the small lengths were used to cover partial contribution to injection.
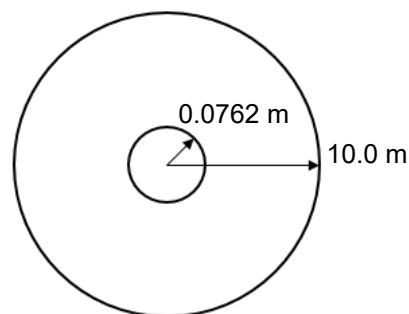
Figure 17: Drawdown boundaries.

From the calculations, it can be seen, that high pressures are encountered within the first 1 m away from the borehole. The highest pressure drop is met with a liner length of 50 m, as expected. This is because the Darcy velocity v_D used in calculating apparent

viscosity is a function of flow rate and the area as seen in equation 2. In addition, since the area is a function of the radius and length of the liner, at a specific flow rate, higher Darcy velocity is derived for smaller lengths. As stated earlier and seen in Figure 14 , the apparent viscosity increases up to a maximum as the velocity increases and then falls by further increase in velocity leading to higher pressures drops in the near wellbore region where high flow velocities are expected. Figure 18 shows for example the results achieved at an injection rate of 200 m³/day for different liner lengths.
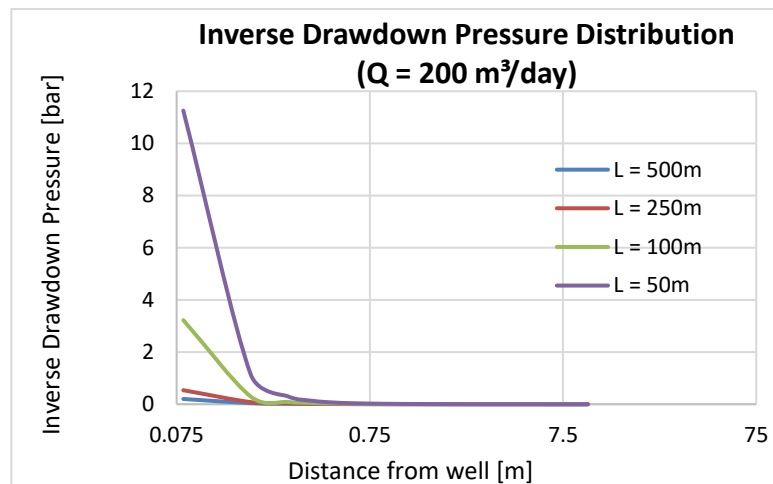
Figure 18: Drawdown pressure for 200 m³/day flowrate.

A 500 m length delivered the lowest drawdown pressure. Increasing the flowrate increases the inverse pressure drawdown and the trends received in the other flow rates are similar to that of 200 m³/day, however of different magnitudes. Figure 19 compares the inverse pressure drawdown at a liner length of 500 m for the different injection flow rates under investigation. This shows how the pressure losses decrease as the fluid moves deeper into the reservoir. Similar trends are observed for the other liner lengths under consideration.
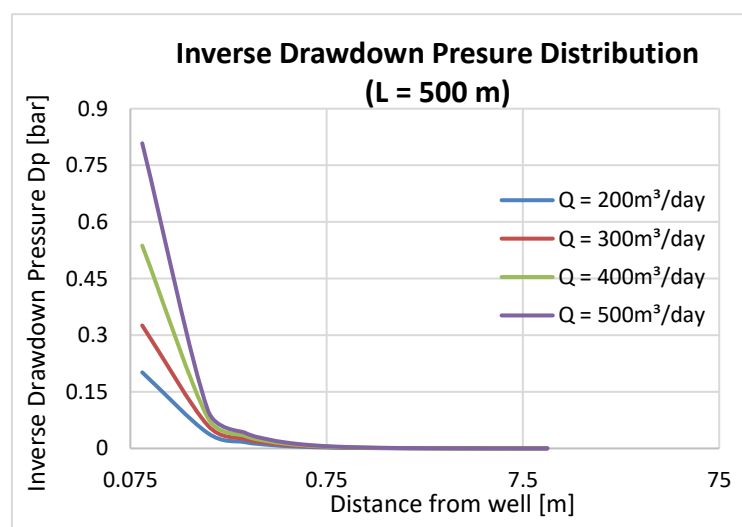
Figure 19: Drawdown pressure of a 500 m Liner at different flow rates.

In a Newtonian system, due to the linear behaviour of shear stress to shear rate, reducing the length of the liner by a half leads to an increase in the inverse pressure drawdown by a factor of two. This however, cannot be confirmed for a non-Newtonian system due to the non-linear dependency of the apparent viscosity to the Darcy velocity.

2.4 Radial Drawdown Pressure in the near Wellbore Region of a Heterogeneous Reservoir

To investigate the effect of heterogeneity of the reservoir on the injectivity of the polymer solution, it is assumed to have a layered reservoir with each having a different permeability, a constant pressure difference at the boundaries, and an equal drainage radius. Crossflow between the layers is not taken into account for the sake of simplicity in the calculations. According to Garland (1966) injected fluid into a layered reservoir pursues the path of the least resistance to flow, and thus flow through the layer with higher permeability (Garland, 1966). Therefore most fraction of the fluid injected will flow through the high permeable layer. Emami et al. (2008) describe that this would lead to most fraction of the oil remaining in the lower permeable zone, affecting the sweep efficiency (Emami Meybodi et al., 2008).

Consequently, the aim of these calculations is to figure out the velocity propagation of the polymer fluid in the different layers as the apparent viscosities change with velocity and to find out the impact of permeability and layer thickness (kh) on the flow velocity. To have a better comparison to the polymer solution, a Newtonian fluid, i.e. water was also considered. Figure 20 represent a schematic drawing of the layered reservoir along the horizontal borehole, where Q_T represent the total flowrate, h the total length, k_1 and k_2 the respective permeability of layer 1 and 2, h_1 and h_2 the lengths, μ_1 and μ_2 the viscosities and Q_1 and Q_2 the respective flowrates.
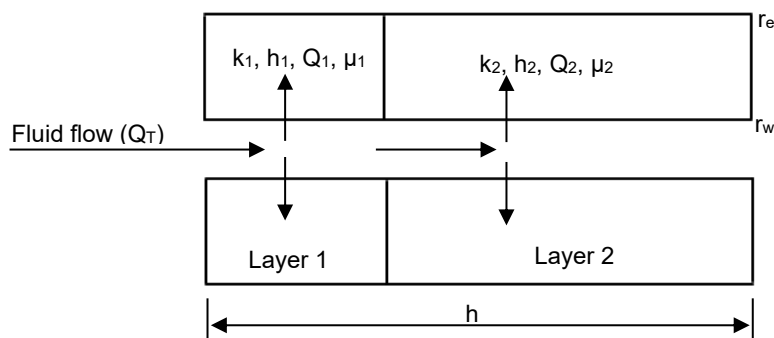
Figure 20: Schematic diagram of radial flow in layered reservoir.

In a layered parallel bedded reservoir with different permeabilities, the average permeability is determined using the weighted average permeability as described by Ahmed (2006). It is assumed, that there is no crossflow between the layers and therefore the total flowrate can be described using equation 21 (Ahmed, 2006, p. 243):

$$Q_T = Q_1 + Q_2 \qquad\qquad 21$$

Using the Darcy equation for radial flow, the flow rate for Q_1 und Q_2 are expressed in equation 22 and 23. In the Newtonian fluid calculations, the viscosity stays constant, thus µ1 = µ2, whilst in the non-Newtonian the viscosity varies with the Darcy velocity.

Layer 1: $$Q_1 = \frac{k_1 \, 2 \, \pi \, h_1}{\mu} \frac{dp}{dr} \qquad\qquad 22$$

Layer 2: $$Q_2 = \frac{k_2 \, 2 \, \pi \, h_2}{\mu} \frac{dp}{dr} \qquad\qquad 23$$

The sum of equation 22 and 23 can be seen in equation 24 , from which it is possible to calculate the weighted average permeability of the layers.

$$Q_T = Q_1 + Q_2 = \frac{k_{av} \, 2 \, \pi \, h}{\mu} \frac{dp}{dr} \qquad\qquad 24$$
$$= \frac{k_1 \, 2 \, \pi \, h_1}{\mu} \frac{dp}{dr} + \frac{k_2 \, 2 \, \pi \, h_2}{\mu} \frac{dp}{dr}$$

The weighted average permeability k_{av}, is given in equation 25 :

$$k_{av} = \frac{k_1 \, h_1 + k_2 \, h_2}{h} \qquad\qquad 25$$

Knowing the total flowrate, the fraction of flow into a specific layer can be calculated by building a ratio between the specific flowrates as a function of their respective permeability and their length of the layer multiplied by the total flowrate. The flowrate of layer 1 is given in equation 26

Layer 1: $$Q_1 = \frac{k_1 \, h_1}{k_1 \, h_1 + k_2 \, h_2} \, Q_T \qquad\qquad 26$$

and that for layer 2 in equation 27

Layer 2: $$Q_2 = \frac{k_2 \, h_2}{k_1 \, h_1 + k_2 \, h_2} \, Q_T \qquad\qquad 27$$

After computing the volumetric flowrate into the layers, the Darcy velocity for each layer can be calculated using equation 2 and subsequently the drawdown pressure with equation 14. The difference in drawdown pressure between layer 1 and 2 should be equal to zero since a constant boundary pressure is assumed and the radius for both layers are equal. Since this is the case for the Newtonian fluid however not for the non-

Newtonian polymer solution with velocity dependent viscosity, through reverse calculation using a what-if-analysis or a goal seeker function, the pressure difference at the boundary is set to zero. This enables the recalculating of the flow rates and hence the corresponding Darcy velocities resulting in a differential pressure of zero at the boundary.

In these calculations, the drainage radius under investigation is set to 5 m with an openhole radius of 0.0762 inches (6" openhole) and the viscosity of the Newtonian fluid, i.e. water, is 1 cp (1mPa·s). For the viscosity of the polymer solution, the adapted unsheared 800 ppm polymer curve as illustrated in Figure 16 was used. Calculations are done for a 500 m horizontal well with variable layer lengths. The varied lengths for layer 1 are 1, 10, 125, 250 and 490 m. The lengths of layer 2 add up to give a total horizontal well length of 500 m. The flowrates considered are 100, 200, 300 and 500 m³/day. The permeability ratio, k_1/k_2, are as follows 10/5, 10/1 and 10/0.5.

The results show that in Newtonian systems the radial drawdown pressure is much lower than that of the non-Newtonian fluid and henceforth higher flow velocities in the Newtonian fluid than in the non-Newtonian. Figure 22 shows the decline in velocity of the injected Newtonian fluid as the fluid propagates into the reservoir. Having two different layers leads to two different Darcy velocities, i.e. v_1 and v_2. It is observed, that the highest velocity among the investigated flow rates was achieved with the configuration of 500 m³/day flow rate, permeability ratio of 20, thus k_1 = 10 mD and k_2 = 0.5 mD and a layer length of h_1 = 1 m and h_2 = 499 m for both Newtonian and non-Newtonian fluids, as illustrated in Figure 21. Due to the higher permeability and lower area of layer 1 as compared to layer 2, layer 1 has an initial velocity of 37.7 m/day and declines to about 0.6 m/day at distance of 5 m. Layer 2 has initially a velocity of 1.9 m/day and declines with distance to about 0.03 m/day.
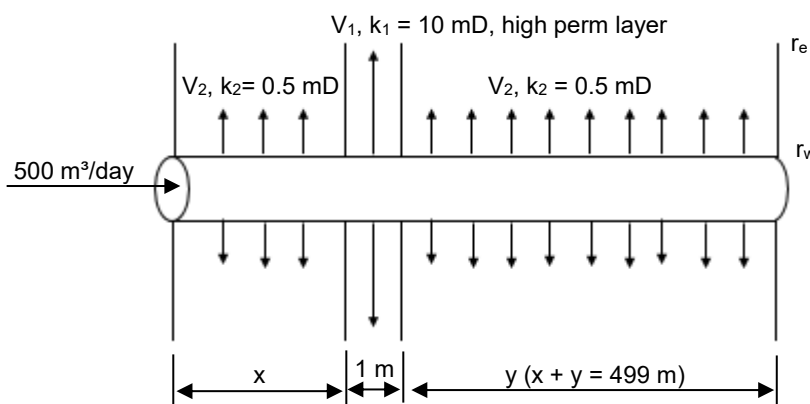
Figure 21: Illustration of velocity profile of layer 1 and 2.

Figure 22: Velocity distribution of Newtonian fluid in a layered reservoir at a flow rate of 500 m³/day, a high perm layer of 1 m and $k_1/k_2 = 20$.

The velocity distribution of the same configuration as seen Figure 21 for non-Newtonian flow can be seen in Figure 23. It is observed that the initial velocity in layer 1 is 9.7 m/day and that of layer 2 is 1.9 m/day. Comparing these results to those of the Newtonian fluid, reveal that due to the higher viscosity of the non-Newtonian fluid, the velocity achieved with non-Newtonian fluid is much lower than that of the Newtonian. The difference in velocity in layer 1 between both fluids is about a factor of 4. In the lower permeable layers however, the difference in the initial velocities are insignificantly low.

Figure 23: Velocity distribution of non-Newtonian fluid in a layered reservoir at a flow rate of 500 m³/day, a high perm layer of 1 m and $k_1/k_2 = 20$.

The viscosity change per distance of Newtonian and non-Newtonian is shown in Figure 24. The viscosity of the non-Newtonian decreases with increasing distance owing to the decrease in velocity. This is because of the behaviour of the polymer as shown in

Figure 16. The Newtonian fluid viscosity is constant over the distance due to its linear shear rate – shear stress relationship.
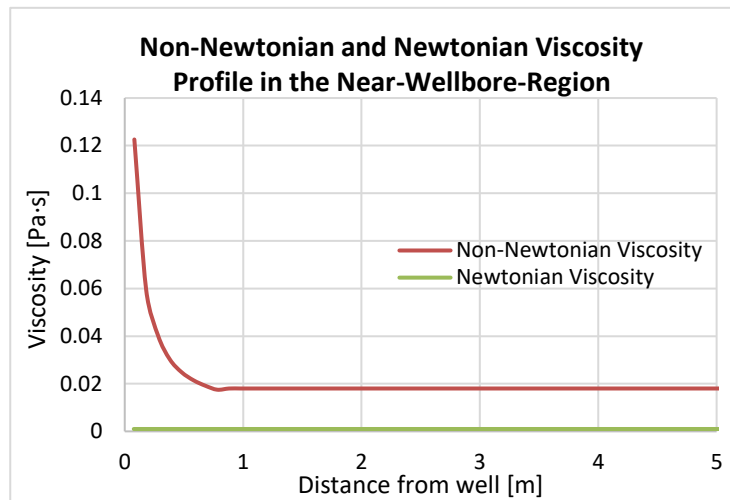
Figure 24: Viscosity relationship to distance from wellbore at a flow rate of 500 m³/day and a high perm layer of 1 m.

It is observed that for the above-mentioned configuration of 500 m³/day, the velocity in the higher permeability layer decreases with decreasing permeability ratio (k_1/k_2) whilst that of the lower permeability increases. This makes sense in the fact that as the permeability of the second layer approaches that of the first, there should be an increase in velocity in the second layer and hence the velocities should be equal at equal permeability and layer thickness as it would be in a one layered reservoir. Figure 25 and Figure 26 show the velocity reduction with distance for different permeability ratios at a flow rate of 500 m³/day for Newtonian and non-Newtonian fluids respectively.
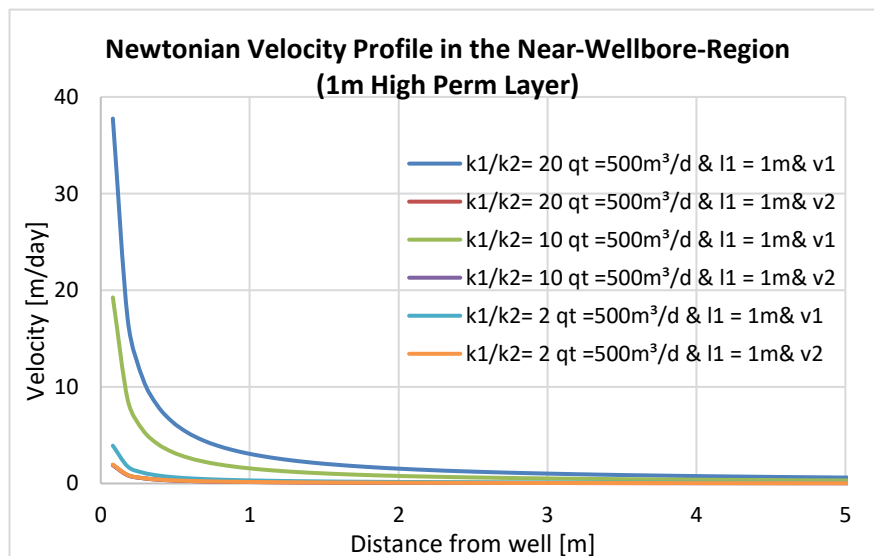
Figure 25: Velocity distribution of Newtonian fluid in a layered reservoir at a flow rate of 500 m³/day and a high perm layer of 1 m for different k_1/k_2.
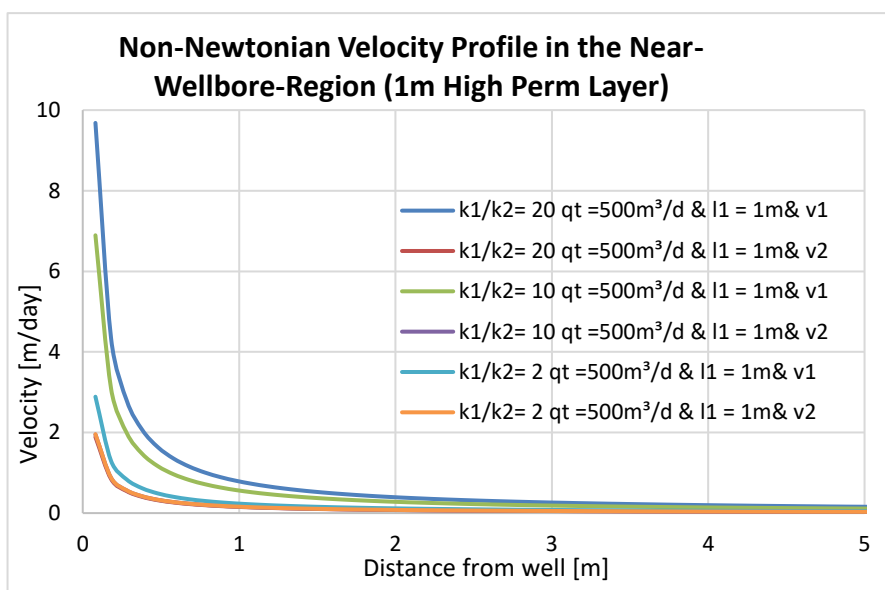
Figure 26: Velocity distribution of non-Newtonian fluid in a layered reservoir at a flow rate of 500 m³/day and a high perm layer of 1 m for different k_1/k_2.

It is also observed that as the thickness of layer 1 increases, for example from 1 m to 125 m as depicted in Figure 27, a trend of decreasing velocities could be seen. This implies that despite the high permeability of layer 1, there is a reduction in velocity in the high permeability layer as the area increases. This is to be expected because the flow velocity is the ratio of flow rate to area. Therefore, increasing the area decreases the velocity.
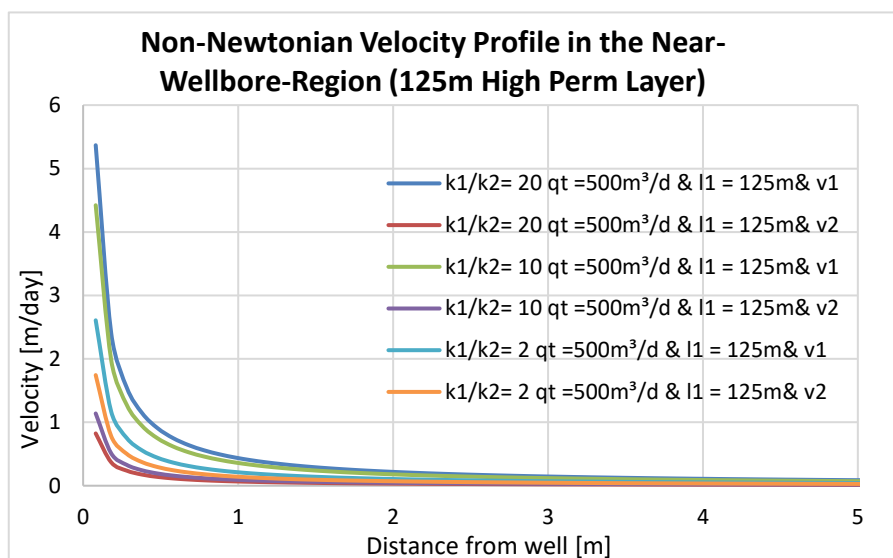
Figure 27: Velocity distribution of non-Newtonian fluid in a layered reservoir at a flow rate of 500 m³/day and a high perm layer of 125 m for different k_1/k_2.

These effects and trends observed in the 500 m³/day flowrates are also observed in the other investigated flowrates. Figure 28 and in Figure 29 illustrate the velocity reduction of 100 m³/day flow rate for Newtonian and non-Newtonian flow respectively.

For the same constellation as seen in Figure 21 however, with a flow rate of 100 m³/day show that the velocity in the high perm layer 1 decreases to 7.5 m/day initially as compared to 500 m³/day with an initial velocity of 37.7 m/day in the Newtonian flow. In the low permeable layer 2 the velocity is initially at 0.17 m/day at a flow rate of 100 m³/day and 0.84 m/day at 500 m³/day. Comparing these velocities at 500 m³/day and 100 m³/ day give a factor of exactly 5 as it is between the flow rates. This owes to the constant relationship of the Newtonian viscosity to velocity. In the non-Newtonian flow, the velocity in the high permeability layer 1 falls to 3.4 m/day at 100 m³/day compared to a 9.7 m/day velocity at 500 m³/day. In the low permeability layer 2 the velocity reduces to 0.4 m/day at 100 m³/day compared to 1.88 m/day at 500 m³/day flow rate.
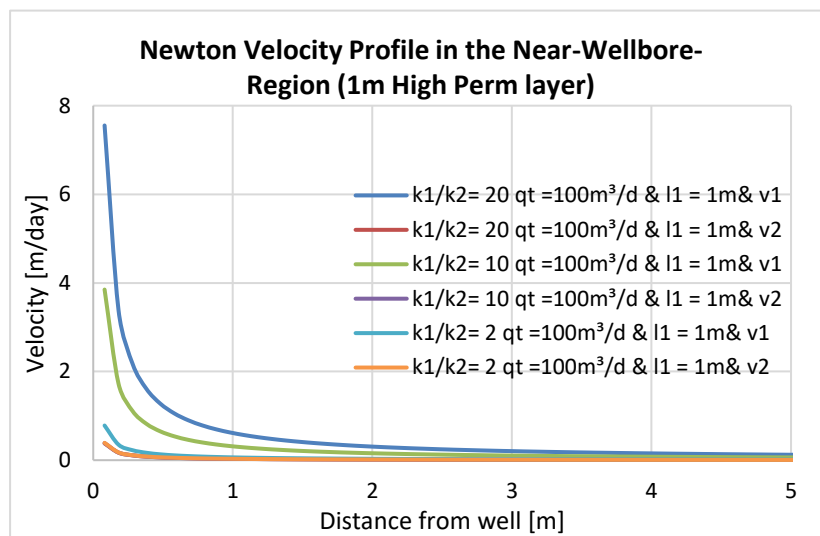
Figure 28: Velocity distribution of Newtonian fluid in a layered reservoir at a flow rate of 100 m³/day and a high perm layer of 1 m for different k_1/k_2.
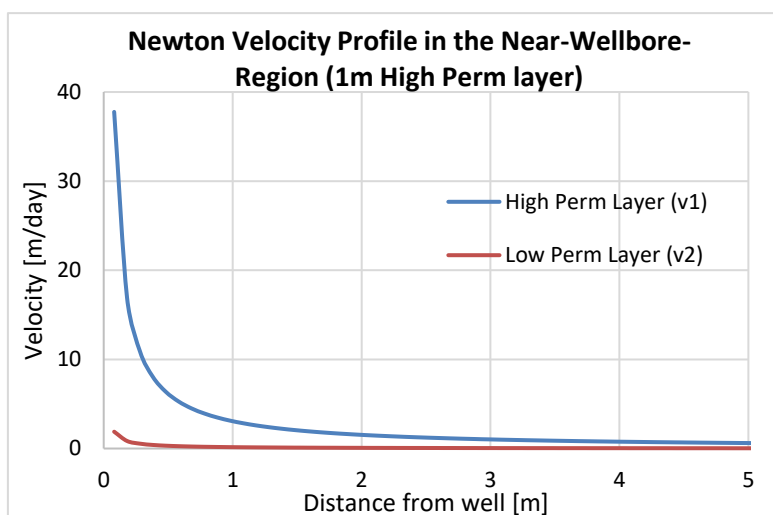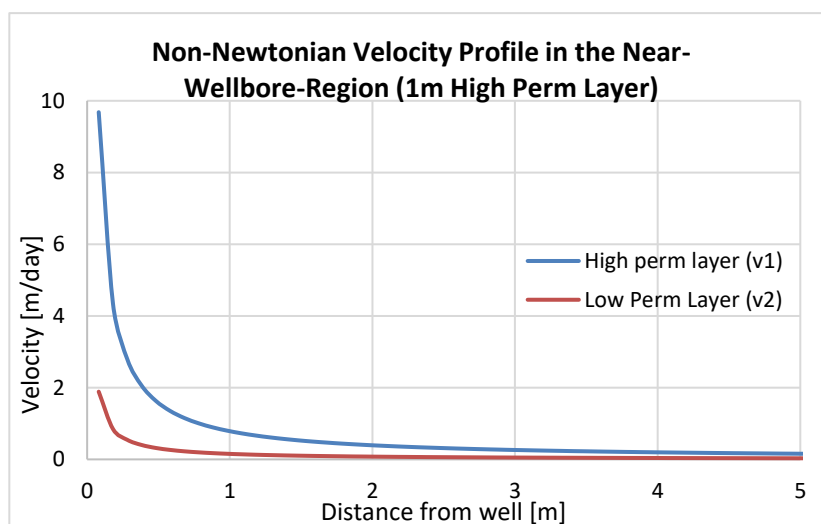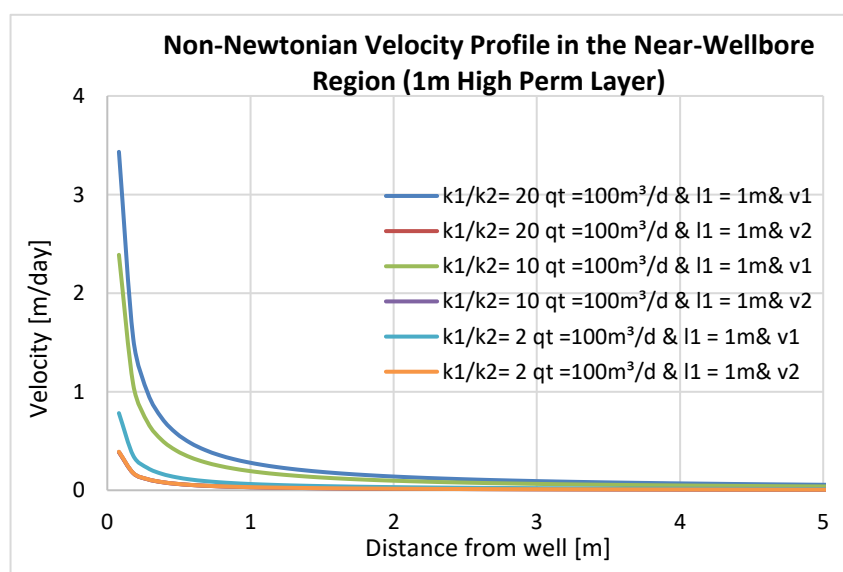

Figure 29: Velocity distribution of non-Newtonian fluid in a layered reservoir at a flow rate of 100 m³/day and a high perm layer of 1 m for different k_1/k_2.

2.5 Velocity Profile at Fracture Interface

Van Golf-Racht (1982) defines a fracture in a specific way as a surface in which a loss of cohesion has occurred and in a general way as a discontinuity breaking rock beds into blocks along cracks, fissures, joints (van Golf-Racht, 1982, p. 6). Reiss (1980) states that these discontinuities introduce considerable difficulties in describing both the internal structure and the flow of fluid through the fracture (Reiss, 1980, p. 3). It is generally differentiated between naturally fractured reservoirs and hydraulically fractured reservoir. As explained by Ramirez et al. (2007), naturally fractured reservoirs contain fractures with significant permeability anisotropy which occurred naturally (Ramirez et al., 2007).

These reservoirs as seen in Figure 30 from Warren and Root, 1963, have connected porous space categorized as the matrix i.e. primary porosity and the fractures i.e. secondary porosity, hence dual porosity. They point out that fractures have relatively higher permeability compared to that of a matrix and therefore can enhance ultimate recovery of a given reservoir. Furthermore, they express, that due to the higher permeability of the fractures over that of the matrix, the possibility of early breakthrough of an injected flooding fluid like water is high (Ramirez et al., 2007).
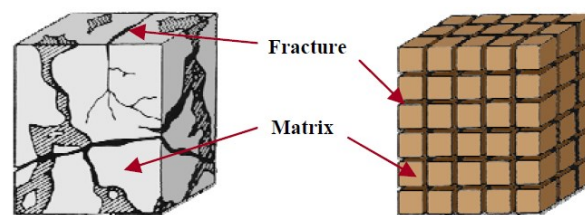
Figure 30: Idealized Dual Porosity of a Heterogeneous Porous Medium (Warren and Root, 1963).

The velocity profile investigation in this section, examines the flow velocity of the fluid as it flows through the horizontal well into the fracture and from there into the formation as illustrated in Figure 31. It is assumed that if injection occurs above the formation parting pressure, fractures form along the horizontal well and due to the high fracture permeability the whole fluid flows through the fracture interface into the formation. Therefore the velocity investigated here is the one at the interface as the fluid moves into the formation. Considering the fracture height and fracture half lengths deliver four areas through which the flow is divided as shown in equation 28. In this investigation, the following flowrates are examined: 200, 300, 400 and 500 m³/day. A fracture height (h) of 10 m and a fracture half-length (l) of 4 m are considered in the calculations. The Darcy velocity is then calculated from equation 2, whereby the total area of the four fracture surfaces are given by equation 28.

$$A = 4lh \hspace{4cm} 28$$
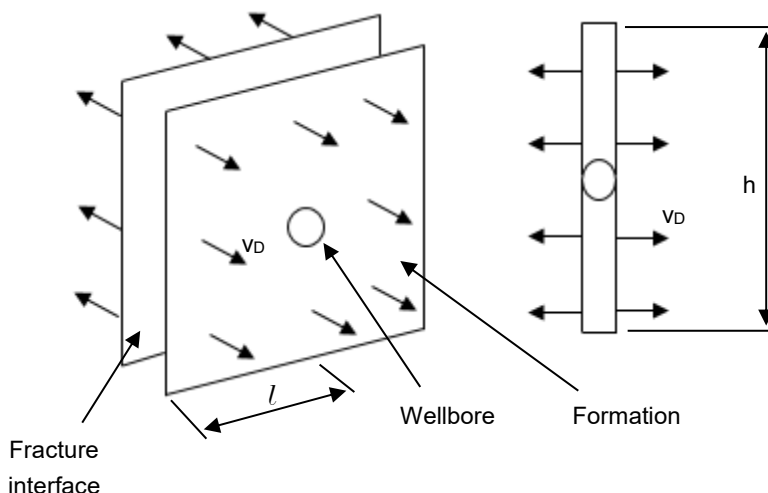
Figure 31: Simple Fracture Model.

From the results as seen in Figure 32 depicts that at a fracture height of 0.5 m, the Darcy velocity at the interface for a 500 m³/day is 62.5 m/day.   At a fracture height of 2 m the velocity is reduced to 15.6 m/day and at 4 m the velocity at the interface falls below 10 m/day. This implies that if injection occurs above the formation parting pressure, for example at a fracture height of 6 m, the velocity would be 3.1 m/day at a 500 m³/day flow rate. Therefore, the polymer fluid does not undergo shear thickening but remains in the shear thinning regime as can be seen in Figure 16. However, if the fracture height is short, the velocity at the interface is high and the polymer solution undergoes shear thickening and degrade. The other flow rates examined show that, the velocity at the interface decreases with decreasing flow rate as seen in Figure 32
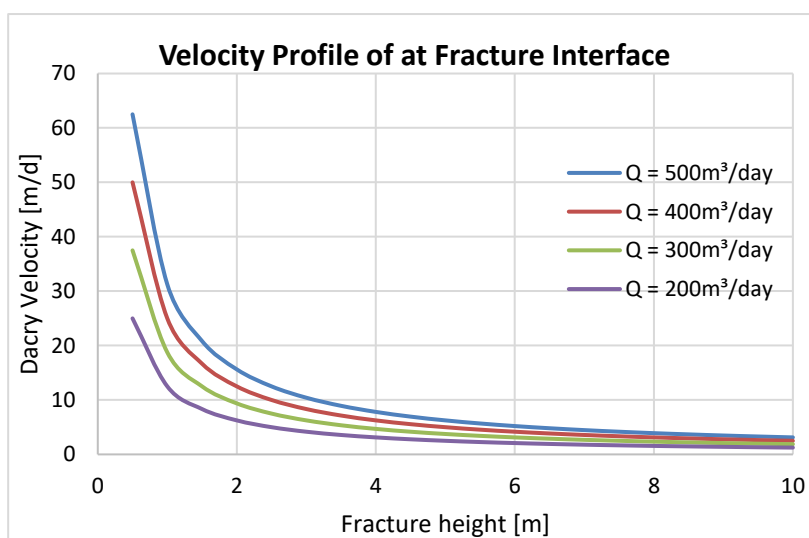
Figure 32: Distribution of Darcy velocity at the fracture interface into the formation

Chapter 3:   Conclusion – Polymer Solution Injectivity

The investigation of the injectivity is essential as this judges first of all the success of the polymer flooding project. It is of high importance that the polymer does not lose its viscous properties during injection into the wellbore because of high flow velocity, which leads to shear thinning, hence lowering the viscosity. Lower viscosity of the solution would lead to a reduction in the effectiveness of the polymer in flooding and consequently reducing the sweep efficiency.

Pressure drop in the horizontal section of the liner, which is predominantly caused by friction, is very low as compared to the injection pressure. Calculations reveal that even at a flow rate of 500 m³/day a maximum of 0.4 bar of pressure drop is encountered at a liner length of 500 m. This shows that during injection, the pressure drop in the horizontal section should not cause a significant reduction in the injection pressure.

In the liner slots, the 175 1/s shear rate calculated for a horizontal contribution length of 25 m is very low as compared to 1000 1/s where polymer degradation would occur. For a 500 m contribution length of 500 m the shear rate through the liner slots is 15 1/s. Owing to these low shear rates, no polymer degradation is expected in the liner slots.

In the near wellbore region of the horizontal well, the inverse drawdown pressure according to the calculations causes no significant reduction in injection pressure. The magnitude of the inverse drawdown pressure is 0.8 bar in the first 1 m of the drawdown radius and reduces further on towards zero for a liner length of 500 m, hence being insignificant. Moreover, there is an irrelevant degree of mechanical polymer degradation in the near wellbore region because of low Darcy velocities, which are below 2 m/day for a high flow rate of 500 m³/day and a 500 m contribution horizontal length. Reducing the contribution horizontal length to 250 m at 500 m³/day increases the velocity to 3.9 m/day, which is also below the polymer degradation velocity of 18 m/day.

Finally, the velocity propagation investigation in the layered and in fractured reservoir in the near wellbore region depict, that higher velocities are encountered in the first 1 m of the drawdown radius. In the layered reservoir, high velocities are observed in thin high permeable layers as compared to larger lower permeable layers for both Newtonian and non-Newtonian fluids. In the high permeable layer injection, through the non-Newtonian shear thinning effects, the velocity in the high permeability layer is minimised. The Darcy velocities at the fracture interface decrease with increasing fracture height and falls below significant values from 4 m onwards for all the flow rates investigated. This depicts that, from such fracture heights, there is no polymer degradation.

Chapter 4:   Polymer Flooding

Polymer flooding is a chemical flooding method under tertiary recovery method. This process involves the dissolution of a water-soluble polymer in water to reduce its mobility. Polymer increases the apparent viscosity of the solution and thereby decreasing the mobility ratio in comparison to water flooding. Polymer flooding projects tend to be economical if the mobility ratio difference between water and polymer flooding is high enough. Reducing the mobility ratio leads to an increase in the sweep efficiency of polymer flooding (Lake et al., 2014 p. 279). The sweep efficiency increases because at reduced mobility ratios viscous fingering is reduced, making the flood front stable (Sheng, 2011 p. 176).

4.1 Mobility Control

The mobility ratio (M), shown in equation 29, is defined as the ratio of the mobility of the displacing fluid (λ_w) to that of the fluid being displaced (λ_o). Mobility ratio less than 1 is considered to have a stable flood and greater than 1 an unstable flood front (Clemens et al., 2010). This means, that at a mobility ratio less than 1 the injected fluid travels slower than the displaced fluid (Ahmed and Meehan, 2012 p. 568).

$$M = \frac{\lambda_w}{\lambda_o} = \frac{mobility\ of\ displacing\ fluid}{mobility\ of\ displaced\ fluid} \qquad\qquad 29$$

Mobility is the relationship between the relative permeability of a fluid and its viscosity as shown in equation 30 (Lake et al., 2014 p. 30).

$$\lambda_{rj} = \frac{k_{rj}}{\mu_j} \qquad\qquad 30$$

Where k_{rj} represent the relative permeability of the fluid and μ_j the viscosity of the fluid and therefore the mobility ratio can be expressed as seen in equation 31 (Littmann, 1988 p. 3).

$$M = \frac{\lambda_w}{\lambda_o} = \frac{(k_{rw}/\mu_w)}{(k_{ro}/\mu_o)} \qquad\qquad 31$$

K_{rw} and μ_w represent relative permeability of water and water viscosity respectively, whilst k_{ro} and μ_o represent relative permeability of oil and oil viscosity respectively. The relative permeability of the fluid is the permeability of a fluid in presence of another and a function of saturation, as shown in Figure 45. It is the ratio of the effective permeability (k_o) of the fluid, measured directly on core plugs in the laboratory, to the absolute permeability (k) of the porous medium as can be seen in equation 32 (Ahmed, 2010 p. 288).

$$k_{ro} = \frac{k_o}{k} \hspace{3cm} 32$$

From equation 31, there are four parameters influencing the mobility ratio which when adjusted have an impact on the displacement efficiency and consequently on the recovery efficiency. Therefore, to achieve a favourable and stable flood, either the oil viscosity is decreased, or the effective permeability to oil is increased, or the effective permeability of water is decreased or the viscosity of water is increased. With the exception of thermal recovery methods, little can be done to alter the oil viscosity and the relative permeability of oil. However, the viscosity of water can be increased by the addition of polymers and thereby decreasing the effective water permeability. This as a result leads to a reduction in the mobility ratio (Ahmed and Meehan, 2012).

Figure 33 illustrates the effect of the mobility ratio on the local saturation profile in a linear 1D water flood. It can be seen that at a mobility ratio lower than 1, the Buckley – Leverett front height is high hindering an early water breakthrough compared to mobility ratios greater than 1 (Sorbie, 1991 p. 248).
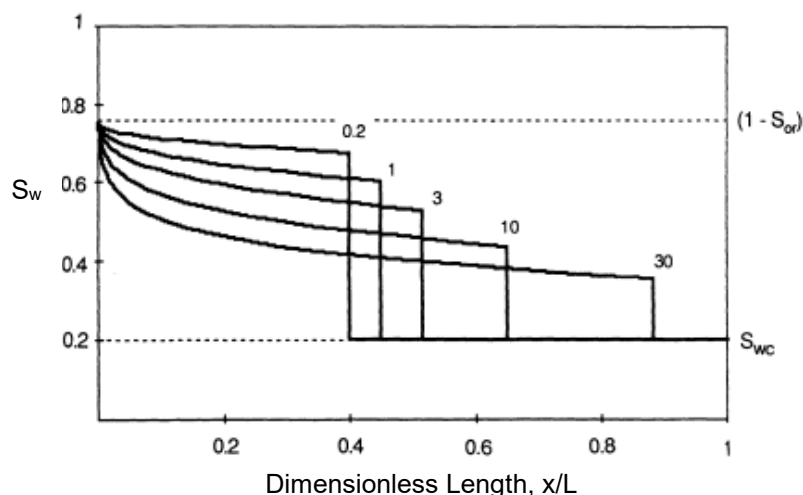
Figure 33: Effect of mobility ratio on in-situ saturation profile (Sorbie, 1991).

At very high mobility ratios, the less viscous displacing fluid flows easily and faster than the more viscous displaced fluid. This causes an occurrence of perturbation leading to viscous fingering – thus unstable displacing front. This can have a severe effect on the sweep efficiency of the displacement process. Figure 34 compares the flooding front of a stable flood, for example polymer solution (M ≤ 1) and that of an unstable water flood (M >> 1).

(a) Water flooding   (b) Polymer flooding
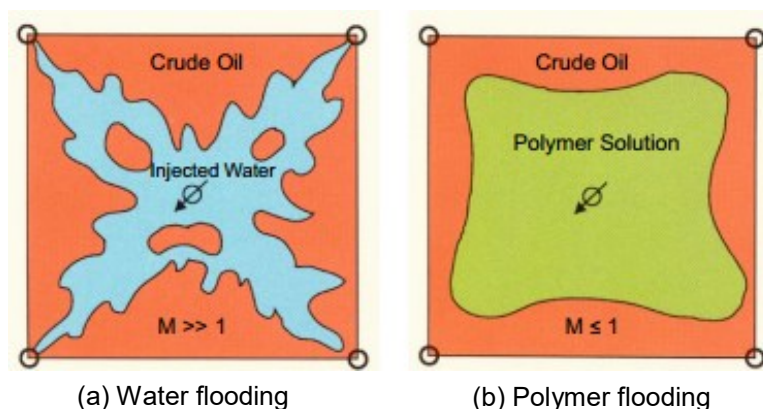
Figure 34: Flood front of an unstable water flooding – viscous fingering (a) and a stable front of polymer solution (b) (Ahmed and Meehan, 2012).

4.2 Recovery Efficiency

Recovery efficiency describes the effectiveness of producing oil and is expressed as the ratio of the amount of oil produced to the amount of oil initially present in the reservoir. The recovery efficiency lies between 0 and 1. To be able to express the recovery efficiency E_R as a function of time, it has to be decomposed into displacement efficiency (microscopic efficiency) E_D and volumetric sweep efficiency (macroscopic efficiency) E_V. Hence, the recovery efficiency is the product of the displacement and volumetric sweep efficiency as shown in equation 33 (Lake et al., 2014 p. 47).

$$E_R = E_D E_V \qquad\qquad\qquad 33$$

4.3 Microscopic Displacement Efficiency

The microscopic displacement efficiency is affected by interfacial tension (IFT), wettability – the ability of a fluid to adhere to the surface of a solid in the presence of another immiscible fluid, capillary pressure and relative permeability. Interfacial tension is the force per unit length acting at the fluid-fluid and rock-fluid interface. Capillary pressure is a result of wettability and is the difference in pressure between the non-wetting and wetting phase (Craft et al., 1991 p. 336). With the density of oil being constant, the microscopic displacement efficiency is defined as the ratio of the amount of oil displaced to the amount of oil contacted by the displacing agent as illustrated in equation 34 (Lake et al., 2014 p. 131).

$$E_D = \frac{Amount\ of\ oil\ displaced}{Amount\ ot\ oil\ contacted\ by\ the\ displacing\ agent} \qquad 34$$

Displacement efficiency is bound between 0 and 1 and the rate at which it approaches 1 is affected by the initial conditions, the displacing agent and the amount of the displacing agent. Concerning immiscible displacement, for example between water and oil, Buckley and Leverett were the first to solve this and later extended by Welge (Lake et al., 2014). Buckley and Leverett developed the frontal displacement theory, which is made up of the fractional flow equation and the frontal advance equation (Ahmed, 2010). In their theory, assumptions are based on linear displacement (1D), immiscible incompressible fluids, validity of Darcy's two-phase equation and the negligence of capillary forces (Heinemann and Mittermeir, 2013 p. 152).

The fractional flow (f_w) developed by Leverett for two immiscible fluids, thus oil and water, is the ratio of the Darcy flow rate of one fluid to the sum of the two flow rates – total flow rate (q) – as shown in equation 35,

$$f_w = \frac{q_w}{q_w + q_o} = \frac{q_w}{q} = \frac{u_w}{u_w + u_o} = \frac{u_w}{u} \qquad 35$$

where q_w, q_o, are the Darcy flow rates of water and oil respectively and u_w, u_o and u are the Darcy velocity of water, oil and the total Darcy velocity respectively (Ahmed, 2010 p. 936), (Lake et al., 2014 p. 132). Equation 35 can be reduced to equation 36, if capillary and gravitational forces are neglected. The new equation now illustrate fractional flow as a function of mobility and mobility ratio (M) (Ahmed, 2010 p. 946).

$$f_w = \frac{\lambda_w}{\lambda_w + \lambda_o} = \frac{1}{1 + \left(\frac{k_{ro}\ \mu_w}{\mu_o\ k_{rw}}\right)} = \frac{1}{1 + (1/M)} \qquad 36$$

The mass conservation equation for oil and water under isothermal immiscible and incompressible fluid flow in porous medium is given by the equation 37. This equation illustrates the change in saturation as a function of time (t) and change in fractional flow as a function of length (x) (Lake et al., 2014).

$$\phi \frac{\partial S_w}{\partial t} + u \frac{\partial f_w}{\partial x} = 0 \qquad 37$$

Φ, S_w and u represent porosity, water saturation and Darcy velocity. The velocity is a function of time only and the fractional flow a function of saturation only. Buckley and Leveret solved the displacement efficiency by solving the saturation (S) as a function of time (t) and position (x) by introducing dimensionless time (t_D) as seen in equation 38 and dimensionless position (x_D), equation 39.

$$t_D = \frac{u}{L\phi} t = \frac{total\ volume\ of\ fluid\ injected}{pore\ volume} \qquad 38$$

$$x_D = \frac{x}{L} \qquad 39$$

L represents the macroscopic permeable medium dimension in the x-direction. Combining equation 37, 38 and 39 result in equation 40, the Buckley – Leverett solution.

$$\frac{\partial S_w}{\partial t_D} + \frac{\partial f_w}{\partial S_w} \frac{\partial S_w}{\partial x_D} = 0 \qquad 40$$

The derivative of the fractional flow curve at a given saturation is the specific velocity (v_{sw}) at that constant saturation. The specific velocity is illustrated in equation 41 (Lake et al., 2014 p. 132 - 135).

$$v_{sw} = \frac{\partial f_w}{\partial S_w} \qquad 41$$

Figure 35 depicts a fractional flow curve for both water and polymer solutions. In this figure, there are no gravitational and capillary effects. A zero capillary pressure generates a shock front. Moreover, there is zero dispersion and adsorption is in equilibrium and the amount of polymer adsorbed (C_a) is a function of the polymer concentration (C). Figure 36 shows the corresponding saturation profile showing the Buckley – Leverett front heights (Sorbie, 1991 p. 252).
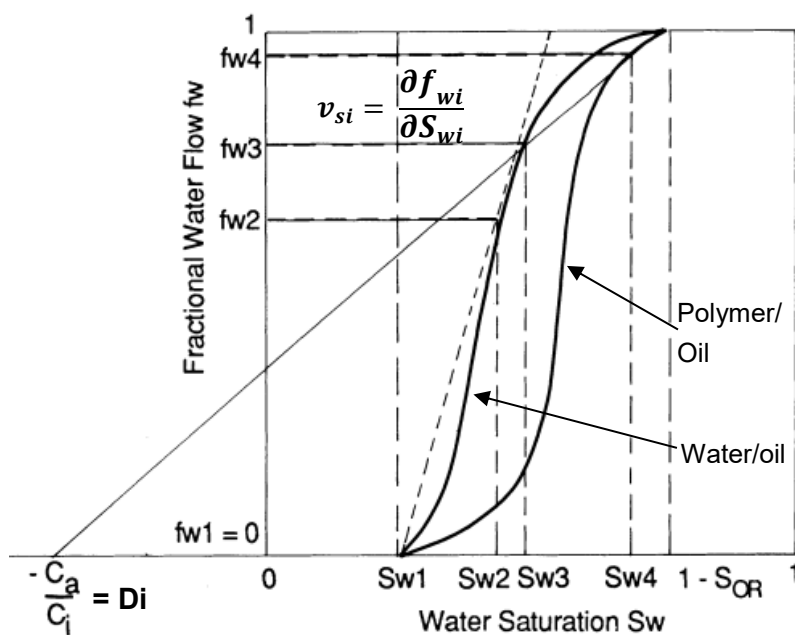
Figure 35: Fractional flow curves for water and polymer floods (Sorbie, 1991).

The intersection of the tangents in the fractional flow curve represent the particular saturation and fraction of water at the flooding front. The quotient –Ca/Ci in the fractional flow curve represent the polymer retention factor Di and expresses the amount of polymer adsorption expressed in pore volume. From Figure 35 the specific velocity of the polymer solution would be

$$v_{sw\ polymer\ solution} = \frac{\partial f_w}{\partial S_w} = \frac{f_{w4}}{S_{w4} - D_i} \qquad\qquad 42$$

and that of water flood would be (Sorbie, 1991 p. 255)

$$v_{sw2\ (water)} = \frac{\partial f_w}{\partial S_w} = \frac{f_{w2}}{S_{w2} - S_{w1}} \qquad\qquad 43$$

From these equations 42 and 43, it can be seen that the specific velocity of the polymer front is lower than that of water as a result of polymer retardation. This leads to stable front and higher displacement efficiency.

In polymer flooding, two saturation shock fronts are formed as can be seen in Figure 36. The first shock is formed as the water saturation increases from its initial saturation as in water flooding. The second saturation shock is formed at the polymer concentration front where the polymer solution contacts the initial water (Pope, 1980). Through the advancement of the second front, the polymer deposited on the rock at its leading edge forms the striped injected water. This striped water and the connate water build a bank, which is pushed forward by the polymer front (Sorbie, 1991 p. 252).
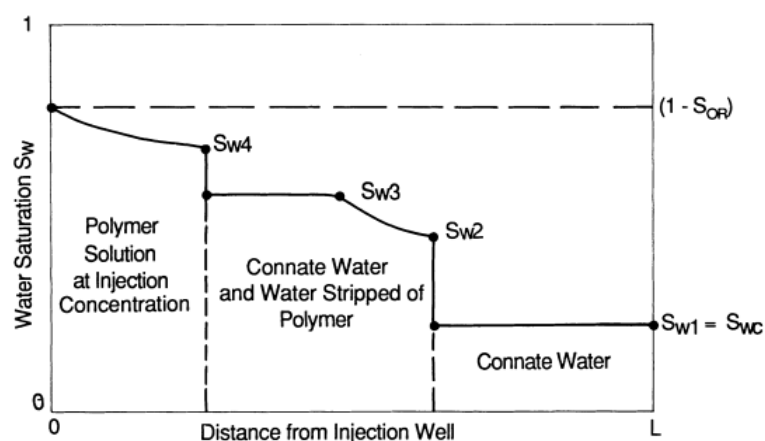
Figure 36: Water saturation fronts in a linear polymer flood (Sorbie, 1991).

The saturation front S_{w2} seen in Figure 36 is the maximum possible saturation, which can form behind the connate water saturation (S_{wc}) and this is equal to the Buckley – Leverett waterfront. Since the intersection of the polymer solution tangent lies higher

than that of the water saturation curve ($S_{w3} > S_{w2}$) as can be seen in Figure 35, this causes the water saturation to decrease from a smaller plateau at saturation value S_{w3}, which is just infront of the polymer bank to S_{w2} which is behind the water front. However if S_{w3} is lower than S_{w2}, then there will be a constant saturation plateau, hence $S_{w2} = S_{w3}$ (Sorbie, 1991 p. 254).

4.4   Macroscopic – Volumetric Sweep Efficiency

The recovery of oil in displacement methods depend on the volume of reservoir, which is contacted by the fluid injected. Volumetric sweep, also termed macroscopic efficiency can be expressed as a fraction of reservoir pore volume invaded by the injected fluid and is a function of time. (Green and Willhite, 1998 p. 73) Thus volumetric efficiency (E_v) is defined as (Lake et al., 2014 p. 179)

$$E_v = \frac{Volume\ of\ oil\ contacted\ by\ displacing\ agent}{Volume\ of\ oil\ initially\ in\ place} \qquad 44$$

Generally, there are four factors influencing how much of a reservoir is going to be contacted by the displacing agent. These include properties of the injected fluid, properties of the fluid to be displaced, geological characteristics and properties of the reservoir rock and lastly the geometry of the injection and production pattern. Volumetric sweep efficiency can be decomposed as the product of areal (E_A) and vertical (E_I) sweep efficiencies as shown in equation 45 (Green and Willhite, 1998 p. 74).

$$E_v = E_A E_I \qquad 45$$

The areal sweep efficiency (E_A) can be defined as (Lake et al., 2014)

$$E_A = \frac{Areal\ contacted\ by\ the\ displacing\ agent}{Total\ area} \qquad 46$$

and the vertical sweep efficiency (E_I) as

$$E_I = \frac{Cross-sectional\ area\ contacted\ by\ the\ displacing\ agent}{Total\ cross-sectional\ area} \qquad 47$$

The schematic of the volumetric sweep efficiency is illustrated in Figure 37 where (a) shows the vertical sweep efficiency and (b) the areal sweep efficiency (Lake et al., 2014 p.180).
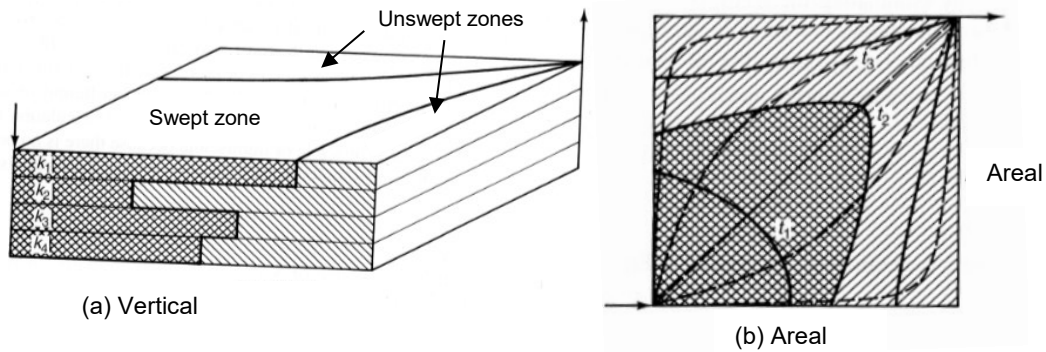
Figure 37: Sweep efficiency schematic (Lake et al., 2014).

Areal sweep efficiency is controlled by four key elements, which are injection and production pattern, the heterogeneity of the reservoir, mobility ratio and gravity and viscous forces (Green and Willhite, 1998 p. 75). Through simulations and analytical methods, the areal sweep efficiency can be determined. Figure 38 shows a typical areal sweep correlation for a five – spot flood pattern (Lake et al., 2014 p. 180).
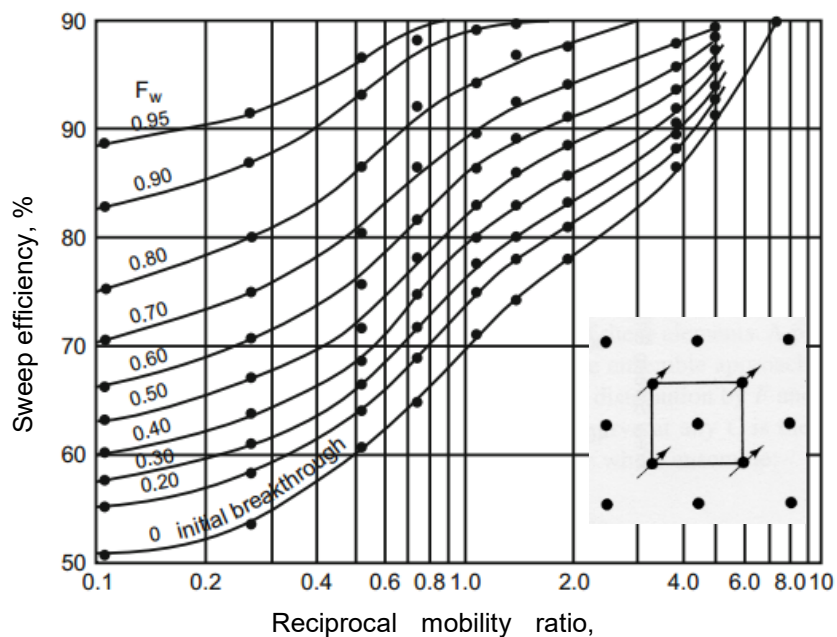
Figure 38: Areal sweep efficiency as a function of 1/M and f_w for a five - spot pattern (Ahmed and Meehan, 2012), (Lake et al., 2014).

Vertical sweep on the other hand is controlled principally by gravity segregation caused by density differences, mobility ratio, variations in the vertical to horizontal permeability (k_v/k_h) and capillary forces (Green and Willhite, 1998 p. 84).

4.5 Types of Polymers

The type of polymers used in EOR activities are synthetic for example partially hydrolysed polyacrylamide (HPAM) and biopolymers such as xanthan. Natural polymers like guar gum and hydroxyl-ethyl-cellulose (HEC) are not commonly applied. Criteria for a suitable EOR polymer include thermal stability, i.e. no $-O-$ in the backbone of the carbon chain, negative ionic hydrophilic group that reduces adsorption of the polymer onto the rock surface, good viscosifying powder and chemical stability through a non-ionic hydrophilic group. According to Sheng, 2011, HPAM best fulfils these criteria (Sheng, 2011 p. 101). Another essential criterion is the stability of the polymer to salts present in the reservoir brine. At high salinity, the reservoir can be conditioned by preflushing the reservoir with water. However, whether a preflush with water is possible depends on the mineralogy of the reservoir (Littmann, 1988 p. 13). A detailed screening criterion can be seen in Table 1.

4.5.1 Polyacrylamide

Polyacrylamides (PAM) are water-soluble straight-chain polymers, whose monomer is acrylamide a compound derived from acrylic acid ($CH_2 = CH - COOH$). Polyacrylamides have a molecular weight in the range of 1 to 8 million g/mol (nowadays 20 million g/mol according to sources from the industry) and are about $0.1 - 0.3$ µm in size. HPAM is obtained by hydrolysing PAM in a caustic water solution. In this process, some of the CONH2 groups react to form carboxyl groups (COOH) (Littmann, 1988 p. 24). The degree of hydrolysis is important in certain physical properties, for example polymer adsorption, shear and thermal stability. Figure 39 illustrates the structure of polyacrylamide (a) and hydrolysed polyacrylamide (b) showing its anionic nature (Sorbie, 1991 p.19). The backbone of the molecule is a -C- single bond rotating freely. HPAM is anionic as a result of its anionic carboxyl group having a negative charge (-COO$^-$) (Lake et al., 2014 p. 282).
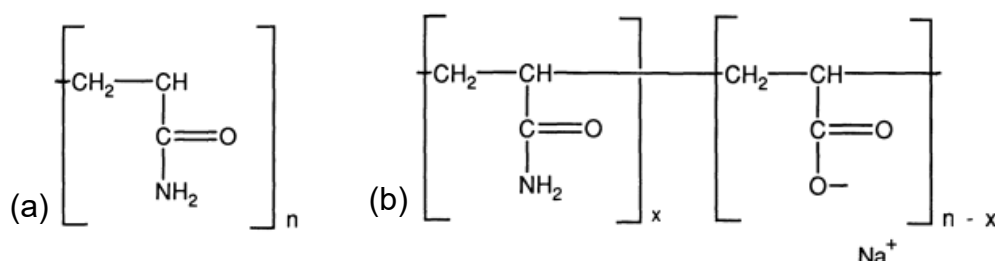
Figure 39: Molecular structure of polyacrylamide (a) and partially hydrolyzed polyacrylamide (HPAM) (Sorbie, 1991).

In a pure distilled water solution, negative charges of the dissociated carboxyl group interact in such a way that molecules of the same charge repulse each other resulting

in a stretched form. This leads to coiling of the molecule that assumes the largest possible volume in the solution. In the presence of low amounts of cations, the negative charges of oxygen are compensated and the molecules tend to curl. The molecule thereby takes a smaller volume in the solution. With increasing amounts of divalent cations, the molecules may be cross-linked leading to the formation of a gel if the polymer concentration is high enough. The effect of water hardness on the viscosity can be seen in Figure 40, which shows, that the higher the valence of the cation the higher the reduction in viscosity with increasing cation concentration (Littmann, 1988 p. 24).
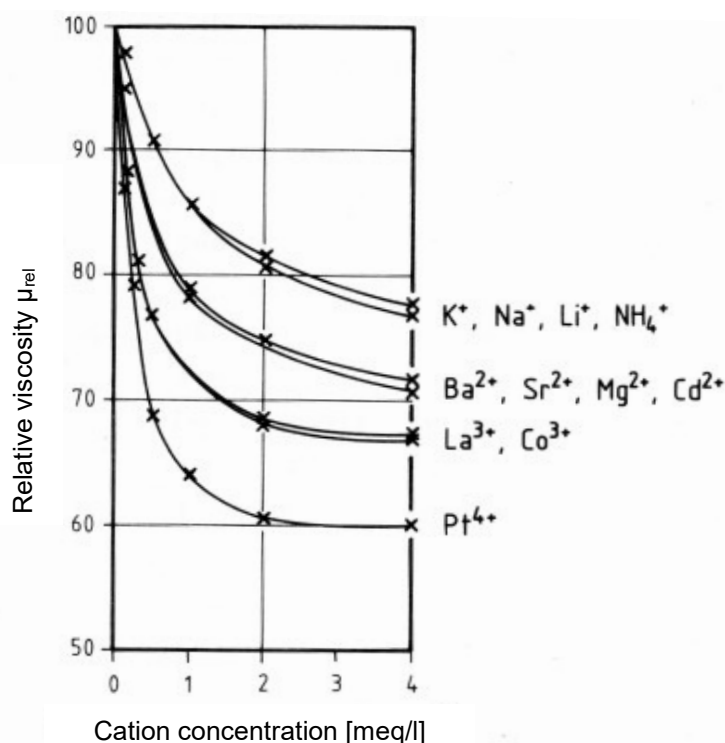
Figure 40: Influence of cations on HPAM viscosity (Littmann, 1988).

4.5.2 Xanthan

Xanthan is a polysaccharide formed by bacterial fermentation process, which make them susceptible to bacterial attack. The backbone of the molecule is a cellulose chain, which has two different side chains. At every second side, there is a glucose ring. Xanthan is less sensitive to salinity, even though like polyacrylamide, also carries electrical charges. This is because of the side chain structure which is stiffer than those in polyacrylamides (Littmann, 1988 p. 30). Another reason is, that xanthan molecule is non-ionic in nature (Lake et al., 2014 p. 283).

Xanthan is more highly branched than HPAM and their oxygen-ringed carbon bond as can be seen in Figure 41 does not rotate fully. Using xanthan in EOR processes does

not significantly reduce the permeability of the reservoir as compared to HPAM. They also do not have significant viscoelastic effects. This provides a good shear stability. Their molecular weight is lower than that of HPAM and are generally in the order of 2 million g/mol (Lake et al., 2014 p. 283).

In polymer flooding, Xanthan is not commonly used because of its expensiveness and therefore, HPAM is widely used. However, in drilling and fracturing operations, they are widely used (Lake et al., 2014 p. 284). According Bragg et al. (1983) Xanthan is not commonly implemented because of microbial degradation leading to loss in viscosity. From their pilot test, laboratory experiments revealed that under anaerobic conditions bacteria culture can cause over 90% loss of Xanthan viscosity within seven days (Bragg et al., 1983).
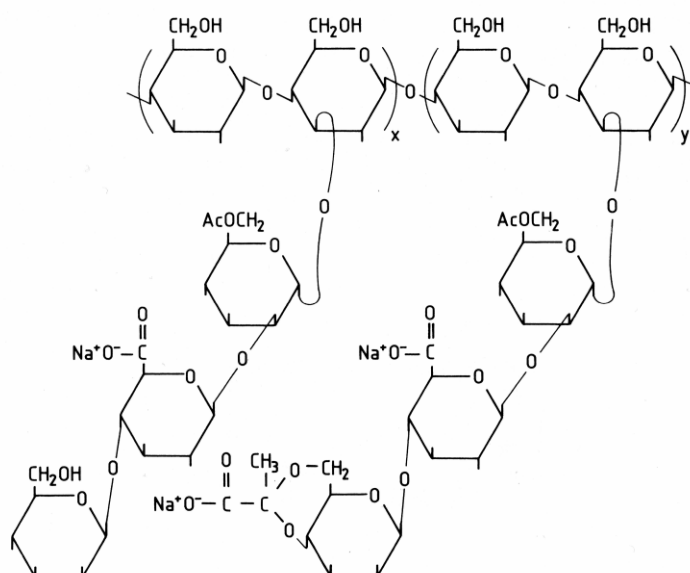
Figure 41: Molecular structure of xanthan (Littmann, 1988).

4.6 Polymer Retention

Polymers experience retention in porous media because of adsorption of the polymer molecules onto the rock surface or being trapped within small pores. The magnitude of retention differs among polymer types and depends on several factors such as concentration of polymer in the solution, molecular weight of the polymer, characteristics and composition of the rock, brine salinity, flow rate and temperature (Lake et al., 2014 p. 289). The adsorption of the polymer molecules on the rock surface leads to a reduction in the apparent permeability of the rock. The reduction in permeability depends on the amount of polymer retained, the pore size distribution and

the average size of the polymer relative to the pores in the rock (Green and Willhite, 1998 p. 111).

Basically, there are three measures used in describing permeability reduction. These are resistance factor (R_F), permeability reduction factor (R_k) and residual resistance factor (R_{RF}). The resistance factor is defined as the ratio of the brine mobility (λ_w) to that of the polymer solution (λ_p) flowing under the same conditions and indicates the polymer contribution to the total mobility reduction. Equation 48 expresses the resistance factor mathematically.

$$R_F = \frac{\lambda_w}{\lambda_p} = \frac{(k_w/\mu_w)}{(k_p/\mu_p)} \qquad\qquad 48$$

The permeability reduction factor (R_k) describes only the reduction effect of the permeability and is defined as the ratio of the brine permeability (k_w) to that of the polymer solution (k_p) as seen in equation 49.

$$R_K = \frac{k_w}{k_p} \qquad\qquad 49$$

The residual resistance factor (R_{RF}) indicates the permanence of the permeability reduction effect caused by the polymer solution and compares the mobility of the brine (λ_w) before and after the polymer solution (λ_{pa}) injection. It is defined as (Lake et al., 2014 p. 289)

$$R_{RF} = \frac{\lambda_w}{\lambda_{pa}} \qquad\qquad 50$$

4.7 Polymer Degradation

Polymers undergo three types of degradation mechanisms, which are mechanical, chemical and biological. Mechanical degradation occurs when, polymer solutions are subjected to high flow velocities, which can be present in surface equipment like valves, tubing etc. and in downhole completions like perforations. Through partial preshearing of the polymer solution, the degree of the polymer to degrade mechanically can be reduced (Lake et al., 2014). Exposing the polymer solution to high flow velocity or high shear conditions cause the molecules to be scissored. On the contrary, to polysaccharides, polyacrylamides are sensitive to mechanical degradation however, not to the extent that they cannot be considered in EOR activities (Littmann, 1988 p. 32).

Figure 42 illustrates the dependency of the polymer viscosity on the shear rate. As stated earlier polymers are non-Newtonian fluids that exhibit shear thinning behaviour. In this figure it can be seen that at low shear rates the, the polymer behaves like a Newtonian fluid and therefore the apparent viscosity is constant – lower Newtonian. With increasing shear rate there is a transition to shear thinning and at high shear rates, there is another transition into the upper Newtonian region. The polymer viscosity declines from the lower Newtonian region to the upper Newtonian region with increasing shear rate (Green and Willhite, 1998 p. 105).
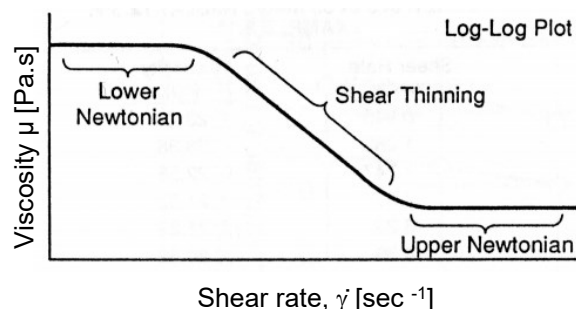

Figure 42: Shear thinning behaviour of polymers (Green and Willhite, 1998).

Chemical degradation of polymers in aqueous solutions is mainly caused by the presence of divalent cations, oxygen and temperature. Divalent cations such as Ca^{2+}, Mg^{2+} and Fe^{2+} affect the hydrolysis of the polyacrylamides and consequently their solution stability. If oxygen is introduced into the solution, in the presence of Fe^{2+} in brines, the Fe^{2+} oxidizes to form Fe^{3+}, which can flocculate both polyacrylamides and polysaccharides (Littmann, 1988 p. 33). Antioxidants like alcohol (isopropanol) and sulphur compounds as well as oxygen scavengers such as hydrazine, sulphur dioxide may be added to prevent or retard these reactions. These mechanisms are accelerated by temperature. Moreover, there are temperatures above which the polymer molecule bonds begin to dissociate. This temperature is fairly high around 127°C. Due to the fact most oil reservoir temperatures are below this temperature, the temperature in concern is the one at which the polymers will break during polymer flooding (Lake et al., 2014 p. 298).

Biological degradation is an issue concerning biopolymers. This is a process whereby bacteria attack and destroy the polymer molecules preferably at low temperatures and salinities. The molecules of xanthan are destroyed under anaerobic conditions through fermentation. The glucose attached to the backbone of the molecule is attacked (Littmann, 1988 p. 33). Biocides such as formaldehyde, sodium dichlorophenol and sodium pentachlorophenol are the commonly used additives in combating bacterial attack (Lake et al., 2014 p. 299).

4.8 Polymer Flooding Process

A typical polymer injection comprises of first an optional preflush, followed by the polymer solution, then an optional fresh water buffer and finally the driving fluid. The preflush generally consists of a low salinity brine (Lake et al., 2014 p. 279). Low salinity is necessary because as discussed earlier the apparent viscosity of the polymer decreases with increasing salinity and especially in the presence of divalent metal ions such as Ca^{2+} and Mg^{2+} (Sheng, 2011). The fresh water buffer is injected after the polymer solution to prevent the backside dilution of the polymer solution. In some cases lower amounts of polymer is added to the fresh water buffer to lower unfavourable mobility ratio between the driving fluid – mostly water – and the polymer solution (Lake et al., 2014 p. 280). Figure 43 illustrates the displacement processes in polymer flooding. This mechanism is however only used in high salinity reservoir and usually not carried out, according to sources from the industry.
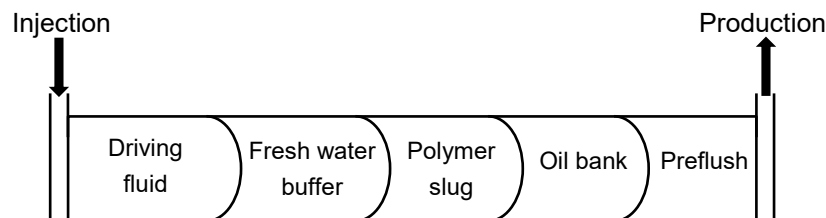
Figure 43: Schematic of polymer flooding process.

Chapter 5:   Polymer Flooding in Horizontal Wells

According to the screening criteria of Dickson et al. (2010), a reservoir with the properties listed in Table 1 make a field an excellent candidate for polymer flooding. Moreover, Taber et al (1997) recommends sandstone reservoirs (Taber et al., 1997) with similar criteria as Dickson et al (2010) for polymer flooding. These criteria qualify the Matzen Field for polymer operations. Indeed, several reservoirs in the Vienna Basin meet these requirements and can therefore profit from polymer flooding as laboratory experiments have confirmed (Poellitzer et al., 2009). Hence several experiments on polymer flooding and some pilot projects have been carried out by OMV in the Vienna Basin since 2011 (Clemens et al., 2013).

Table 1: Screening Criteria for Chemical EOR. (Dickson et al., 2010)

Property	Polymer Flooding
Oil Density (API)	> 15
In-Situ Oil Viscosity (cP)	10 - 1000
Reservoir Depth (ft)	800 - 9000
Reservoir Temperature (°C)	< 77
Oil Saturation (%)	> 30
Formation Salinity (ppm)	< 3000 if ($10 < \mu < 10^2$)

This section of the thesis investigates the optimum well spacing for horizontal wells through a series of simulations using Schlumberger software Petrel and Eclipse 100. The principal idea behind these analyses is to find out the type of geometrical configuration which yields the highest oil recovery. Basically, two sets of geometries are being considered:

1. Constant distance between two producing wells with increasing well length
2. Constant well length with increasing distance between the producing wells.

The injector well lies in the middle of the single pattern in all the geometries under consideration. Simulations are carried out for water flooding as the base case and for polymer flooding for a period of 25 years. Injection begins in January 2017 and ends in January 2042. In the scenarios of polymer flooding, polymer solution is injected after 6 months of water injection at a slug size of 0.8 of the pore volume. After the polymer slug, water injection followed until the end of the injection. Geological models used in the simulation include homogeneous and heterogeneous models. Eight

heterogeneous models with different variogram correlation lengths and azimuth setups were taken into account to find out an optimal placement of the wells – hence which correlation length and azimuth has the best possible oil recovery.

Finally, the economics of such a project is taken into account to find out the relationship between the geometries, oil recovery, utility factor (UF) and discounted oil production. In the economics, drilling and completion costs (capex) and costs of polymer (opex) were considered. Oil price is taken into account as a unit price of 1 $/bbl. The unit technical costs (UTC) is incorporated in these calculations to find out how this relates to the geometries and their corresponding oil recovery.

5.1 Simulation Model and Global Reservoir Properties

The simulation model represents the 8th Tortonian Horizon (8TH) reservoir of the Matzen Field in the Vienna Basin. This is a reservoir, which is made up of sandstone deposits in a shallow marine environment with its porosity ranging from 20 to 30% and an average permeability of about 500 mD. The reservoir is at a depth of 1250 m and has a net thickness of 20 m. Its initial reservoir parameters such as pressure, oil viscosity, temperature and oil density are shown in

Table 2 (Clemens et al., 2013).

Table 2: Initial Reservoir Parameters 8TH Matzen Field. (Clemens et al., 2013)

Initial Conditions	Values
Initial Pressure	113 bar
Initial Temperature	50 °C
In-Situ Oil Viscosity	19 cP
Oil Density	20 API (930 kg/m³)
Formation Salinity	25000 ppm

A box model with a length of 2000 m, width of 1200 m and a height of 11 m was used in the simulations. Figure 44 shows the box model with a gridding of 10 x 10 x 1 m (xyz), hence 264,000 cells.
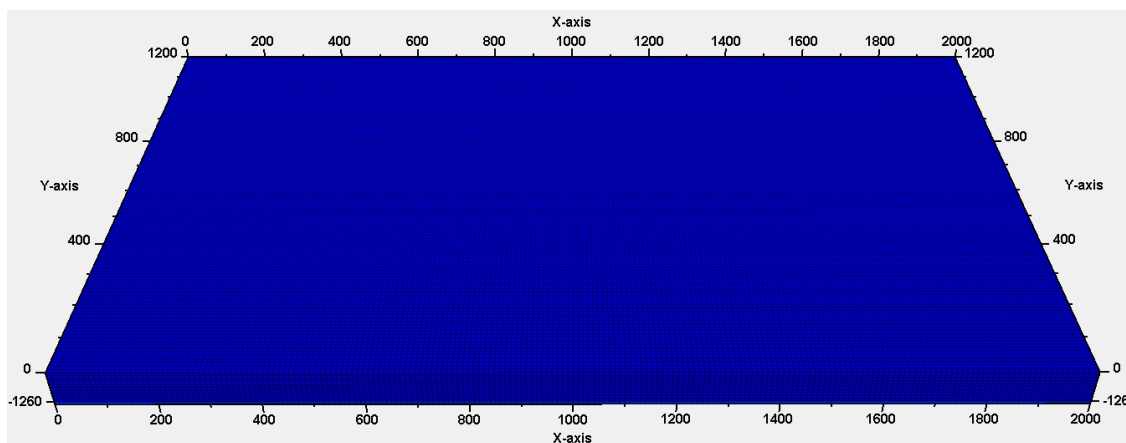
Figure 44: Block Model - 2000 x 1200 x 11 m

The Matzen Field being a matured field has a water cut of about 96%. From the relative permeabilities and fractional flow provided, the oil saturation at 96% water cut is 43%. The model is assumed to be a dead oil model, as the gas production is small. The rock properties assumed are shown in Table 3 and the corresponding relative permeability plot is presented in Figure 45. As can be seen in the plot and in Table 3, the connate water saturation is 0.15 and the irreducible oil saturation is 0.2. The plot also shows that the reservoir is water wet as the intersection of the relative water permeability curve (k_{rw}) and the relative oil permeability curve (k_{ro}) is greater than 0.5.

Table 3: Rock physics functions.

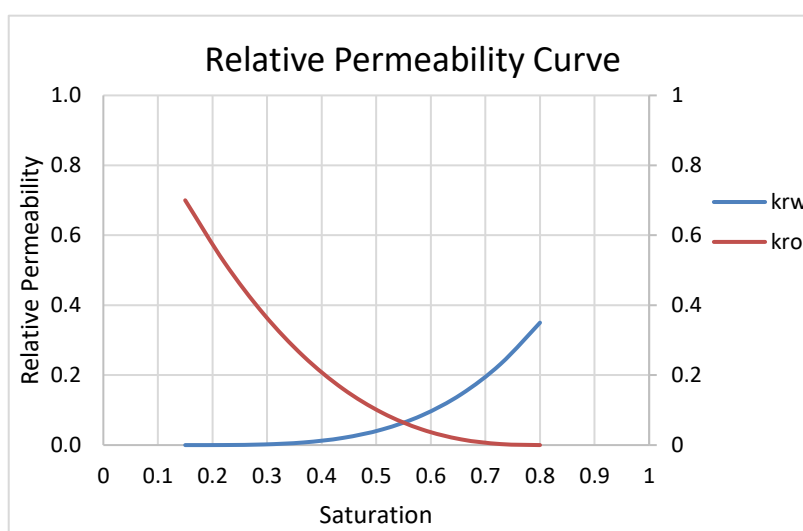| S_{wmin}	0.15	S_{or}	0.20
S_{wcr}	0.15	K_{ro} @ S_{omax}	0.70
Corey Water	3.50	Corey Oil/Water	2.50
K_{rw} @ S=1	1.00	K_{rw} @ S_{orw}	0.35

Figure 45: Relative permeabilities of oil and water saturation.

The boundary conditions include:

- Approximated constant pressure boundary by multiplying the pore volume of the outer most cells of the model by a factor of 10000 mimicking an open boundary.
- Total injection rate equals total production rate giving a voidage replacement ratio of 1.

In order to account for polymer retention, properties of the rock and that of the polymer are incorporated into the simulation model. These properties include rock mass density, the residual resistance factor (R_{RF}) for the rock type and the maximum polymer adsorption for the calculation of the residual resistance factor for the aqueous phase. Their corresponding values are shown in Table 4.

Table 4: Polymer - rock properties.

Property	Value
Sandstone density [kg/m³]	2600
Residual resistance factor (rock type) [/]	2.00
Maximum polymer adsorption [kg/kg]	2.63e-5

The amount of polymer adsorbed is calculated as a function of the in-situ polymer concentration, whereby the amount adsorbed is the mass of polymer adsorbed per unit rock mass. (Schlumberger, 2015 p. 1656). The values are tabulated in Table 5.

Table 5: Polymer adsorption and viscosity as a function of polymer concentration.

Polymer concentration [kg/m³]	Adsorbed Polymer [kg polymer/ kg rock mass]	Polymer concentration [kg/m³]	Polymer Viscosity Multiplier
0.000	0.0000	0.000	1.0000
0.125	1.40e-5	0.500	3.0875
0.250	2.10e-5	0.800	4.5500
0.500	2.50e-5	1.000	5.5250
1.000	2.60e-5	1.500	7.9625
2.000	2.63e-5	2.000	10.400

5.2 Well Configurations

The number of geometrical configurations considered in these simulations include two vertical five- spot patterns and nine horizontal well patterns. The two vertical configurations serve as a comparison to horizontal wells to confirm the advantages of the horizontal wells over vertical wells as stated by Joshi (1991a) – hence the differences in injection pressure distribution in the near well bore region. The focus of this work however is on the horizontal wells. Table 6 shows the dimensions and area of the geometrical patterns, whereby the area represent the area between the producer wells as for example can be seen in Figure 46 through to Figure 49. Figure 46 illustrate a vertical well whilst Figure 47 to Figure 49 show exemplarily horizontal wells with increasing distance between the producers with the wells at a depth of 1256 m.

Table 6: Well Dimensions and Area.

Model	Geometry		Area (m²)
	x [m]	y [m]	
Vert_small	340.00	340.00	115600
Vert_large	480.00	480.00	230400
Hori_3	530.00	210	111300
Hori_4	770.00	210	161700
Hori_5	1030.00	210	216300
Hori_6	530.00	310	164300
Hori_7	770.00	310	238700
Hori_8	1030.00	310	319300
Hori_9	530.00	410	217300
Hori_10	770.00	410	315700
Hori_11	1030.00	410	422300

From the Table 6, it can be seen that vert_large is twice as large as vert_small and the distances between the producing horizontal wells are 210, 310 and 410 m. The lengths of the horizontal wells increase from 530 to 770 and 1030 m.
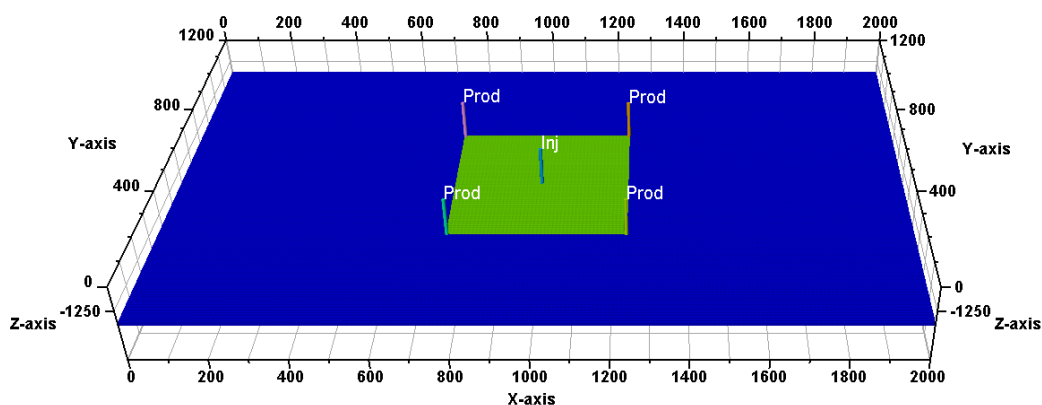

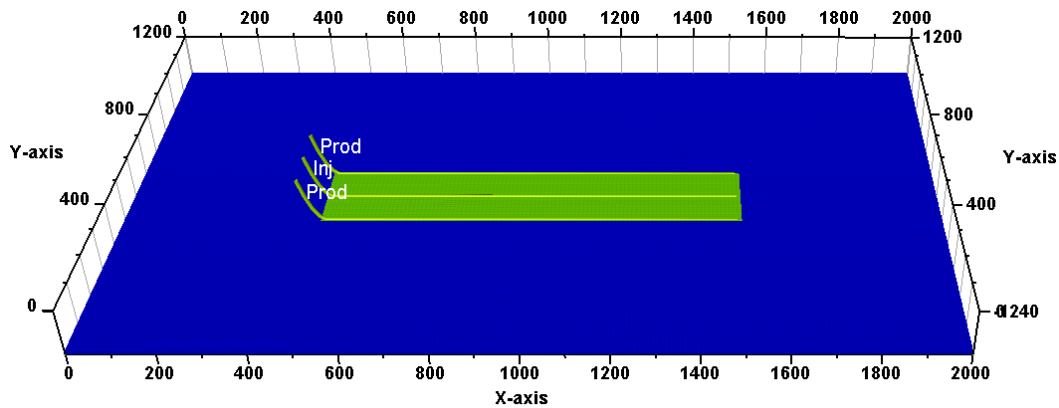Figure 46: vert_large (480 m x 480 m) – vertical wells.

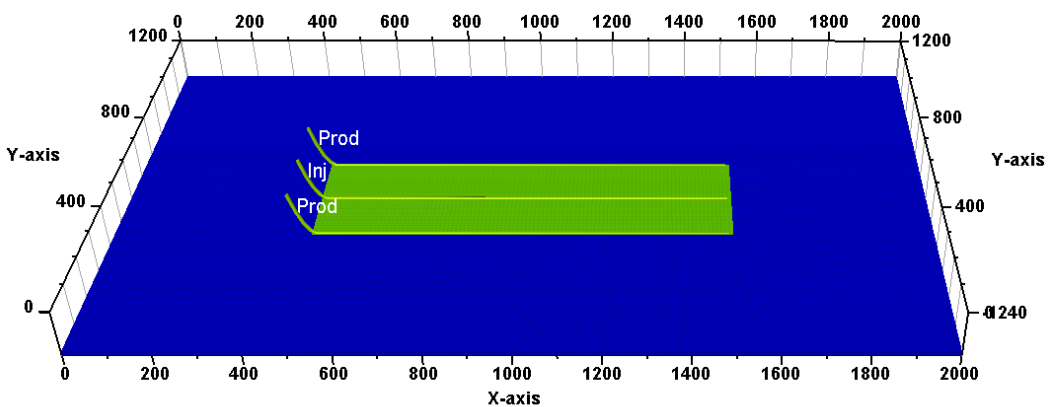Figure 47: Hori_5 (1030 m x 210 m) – horizontal wells.

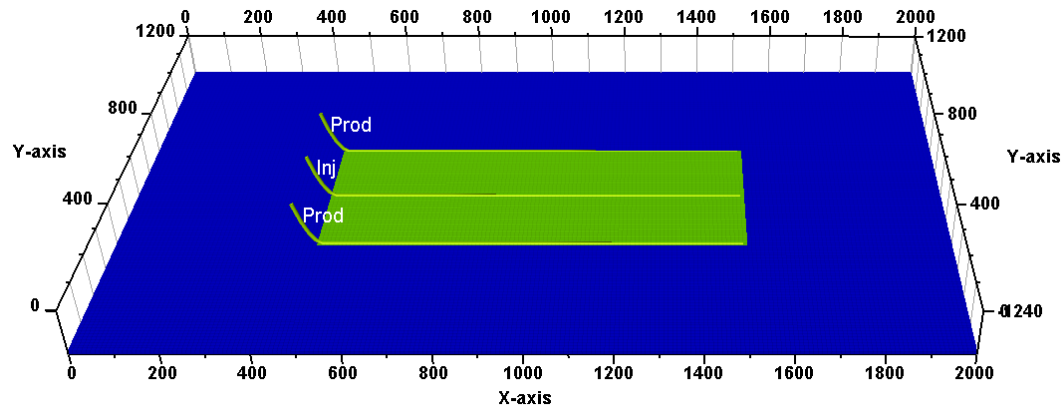Figure 48: Hori_8 (1030 m x 310 m) – horizontal wells.

Figure 49: Hori_11 (1030 m x 410 m) – horizontal wells.

The area of the various configurations multiplied with the reservoir height and average porosity give the reservoir volume. However in order to prevent misunderstanding in relation to the total reservoir, in these investigations, the volume made up of the product of the geometrical pattern area, the reservoir height and porosity is going to be termed Chemical Affected Reservoir Volume (CARV). Sieberer et al., 2016, introduced this term to describe the volume of an injection pattern.

5.3 Model Description

5.3.1 Homogeneous Case

The homogeneous case assumes constant permeability of the model. This implies that the permeability in the x-direction (perm-x) is equal to that in the y-direction. The permeability in the in the z-direction (perm-z), thus between two layers, is assumed to be a tenth of that of permeability in the x- and y- direction (perm-y) and therefore enabling crossflow between the layers. The porosity of the model is set to be 25%, resembling the average porosity of the 8th reservoir. The minimum pressure, thus the pressure in the top layer is 100.05 bar and the maximum at the base layer is 101.00 bar. The water saturation at a water cut of 96% is 0.57. These properties have been tabulated in Table 7. The polymer concentration considered in the homogeneous simulations is 800 ppm.

Table 7: Geological model properties.

Reservoir Property	Value
Perm-x [mD]	1000
Perm-y [mD]	1000
Perm-z [mD]	100.0
Porosity [%]	25.00
Oil Saturation [/]	0.430
Pressure @ 1250 m [bar]	100.05
Pressure @ 1261 m [bar]	101.00

5.3.2 Heterogeneous Case

Using a variogram with different correlation lengths (CL), porosity is assigned to the models. The correlation length, as shown in Figure 50, hast two main parameters, the lengths of the ellipsoid and the direction, i.e. azimuth. The major axis of the ellipsoid dictates its direction. It is assumed that a correlation length with an azimuth of 0° has its major axis at 0° and an azimuth of 90° has it major axis at 90° clockwise from north. In respect to the direction of the horizontal wells, a correlation length of 0° lies perpendicular to the wells and an azimuth of 90° lies parallel to the horizontal wells as can be seen in Figure 50. The models are named to reflect their variogram correlation lengths and azimuth. For example, CL500_250_AZ90 would mean a correlation length with a major axis of 500 m, a minor axis of 250 m and an azimuth of 90° as illustrated in Figure 50.
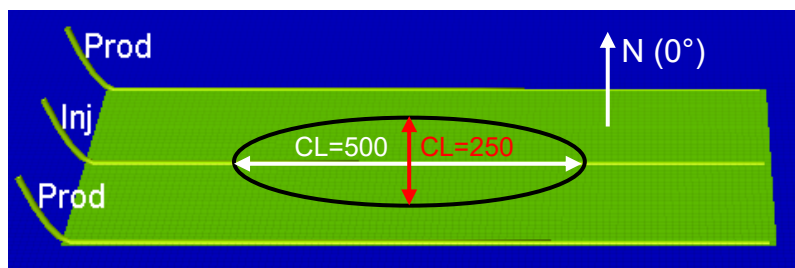
Figure 50: Correlation lengths and azimuth of variogram [CL500_250_AZ90].

From the porosity distribution, which is assigned using variograms, the permeability of the models are calculated. The permeability is calculated using equation 51, where k represent the permeability and ϕ the porosity. In sum, eight correlation lengths are used to generate eight geological models. The correlation lengths represent channel bars.

$$k = 10000^{\phi}$$ 51

In these models, similarly to the homogeneous case, the permeability in x-direction equals that in the y-direction and the permeability of the z-direction is also a tenth of perm-x. For a given heterogeneous model, simulations were carried out for the nine horizontal configurations, hence Hori_3 – Hori_9. The list of the eight heterogeneous models, i.e. geological realizations, with their corresponding correlation lengths, azimuth, mean porosity (ϕ), permeability (k) and standard deviations (σ) of the permeability have been tabularized in Table 8.

Table 8: Heterogeneous models.

Model	CL [m]		Azimuth	Mean ϕ [/]	Mean k [mD]	Standard Deviation (σ) of k [mD]
CL500_250_90	500	250	90°	0.181	214.6	272.2
CL250_125_90	250	125	90°	0.185	256.5	353.7
CL500_125_90	500	125	90°	0.181	231.2	314.6
CL500_250_00	500	250	00°	0.168	143.5	214.2
CL250_125_00	250	125	00°	0.178	190.5	261.8
CL500_125_00	500	125	00°	0.180	213.2	309.2
CL125_62.5_90	125	62.5	90°	0.188	237.0	302.6
CL125_62.5_00	125	62.5	00°	0.186	240.7	319.7

Figure 51 illustrate exemplarily the permeability distribution of CL500_250_AZ90 model and Figure 52 that of its counterpart CL500_250_AZ00. The permeability and

porosity distribution of these models are shown in the form of a histogram in Figure 105 in Appendix C.
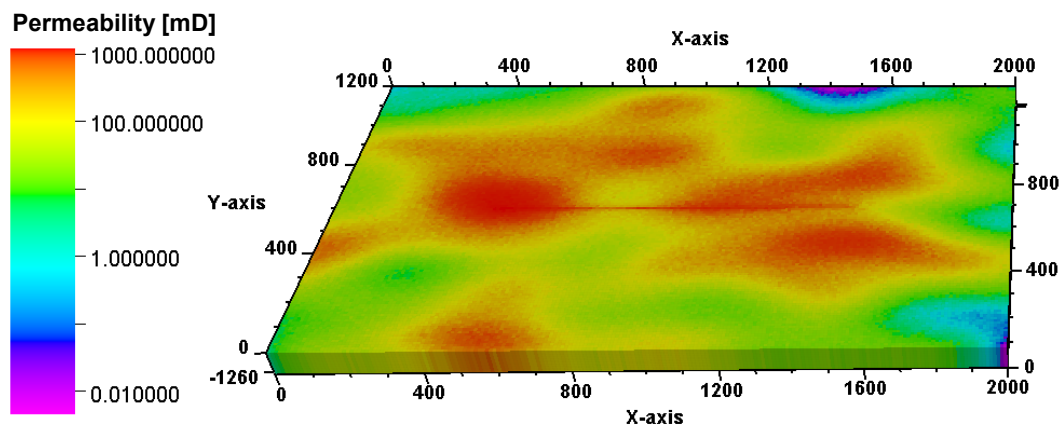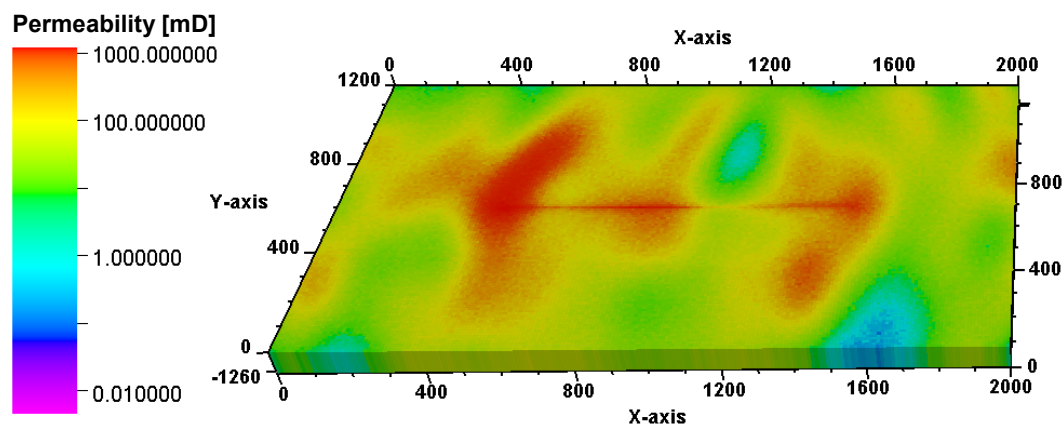

Figure 51: Heterogeneous model - CL500_250_AZ90.

Figure 52: Heterogeneous model - CL500_250_AZ00.

Chapter 6:   Results and Observations

6.1 Homogeneous Case

6.1.1 Injection Pressure Distribution

During injection, the pressure around the injector changes. Comparing the changes in the base case – water injection – to that of the polymer solution, the polymer solution as a result of its higher viscosity and thus reduction in mobility causes higher injection pressure in the near wellbore region. In the polymer scenario, the injection pressure development for the first 6 months behaves like that of the base case and starts increasing from this period on at the start of the polymer injection. The injection pressure increases to a maximum and after the polymer slug size has been displaced by the driving fluid, the injection pressure falls again.

In vertical wells, higher injection pressures are expected as compared to horizontal wells. This can be seen in Figure 53 and Figure 54. In Figure 53, the range of the injection pressure in the base case of the vertical wells can be seen, with 110 bar being the highest and 101 bar the lowest for this specific well configuration. In the case of polymer solution, the injection pressure propagation rises as much as up to 145 bar, which is below the formation parting pressure as non-Newtonian effects are neglected. Thus, considering non-Newton effects frequently lead to fracturing in the vertical well.
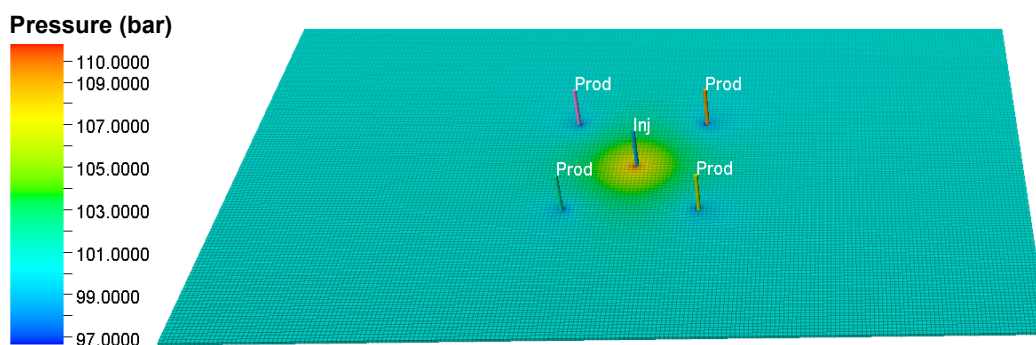

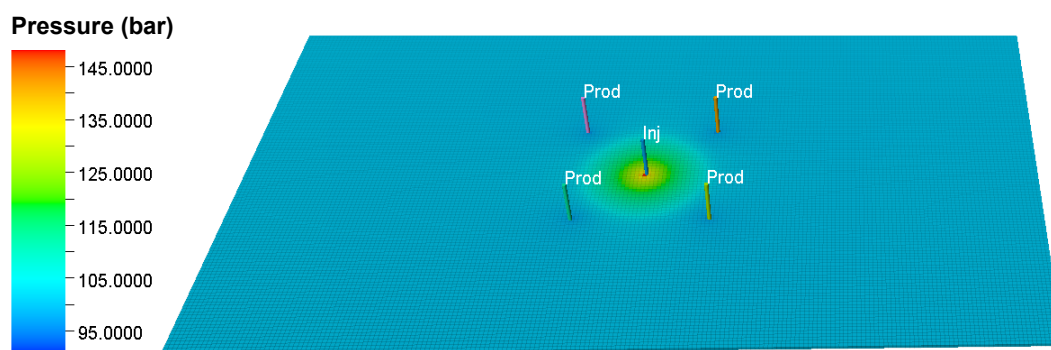Figure 53: Injection pressure, vert_small – base case – 2017.

Figure 54: Injection pressure, vert_small - polymer solution – 2017.

A clearer picture of the injection pressure distribution can be obtained by narrowing the pressure range from 97 bar - 110 bar in the base case and 95 bar - 145 bar in polymer flooding to 101 bar – 105 bar range. Figure 55 illustrates the injection pressure distribution around the injector with a range of 101 to 105 bar for the base case and Figure 56 for the polymer solution. In these figures, the top and the front views are shown.
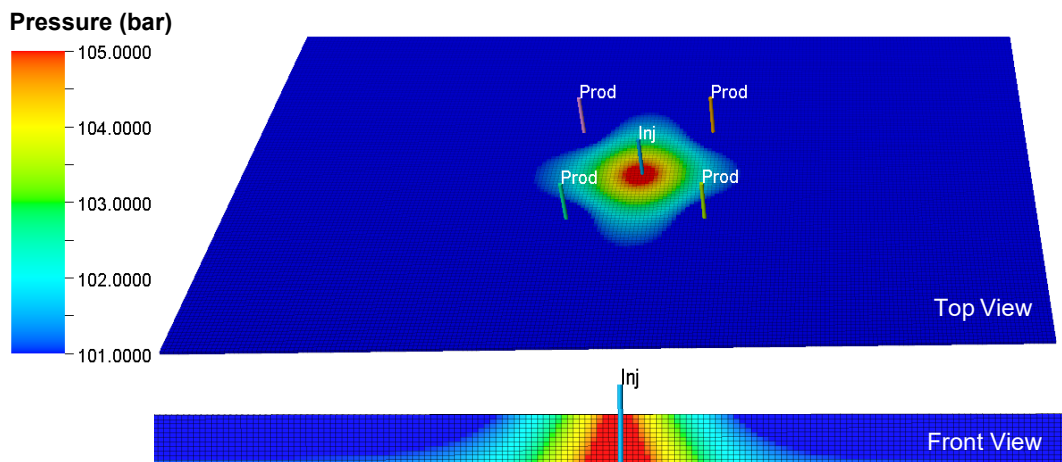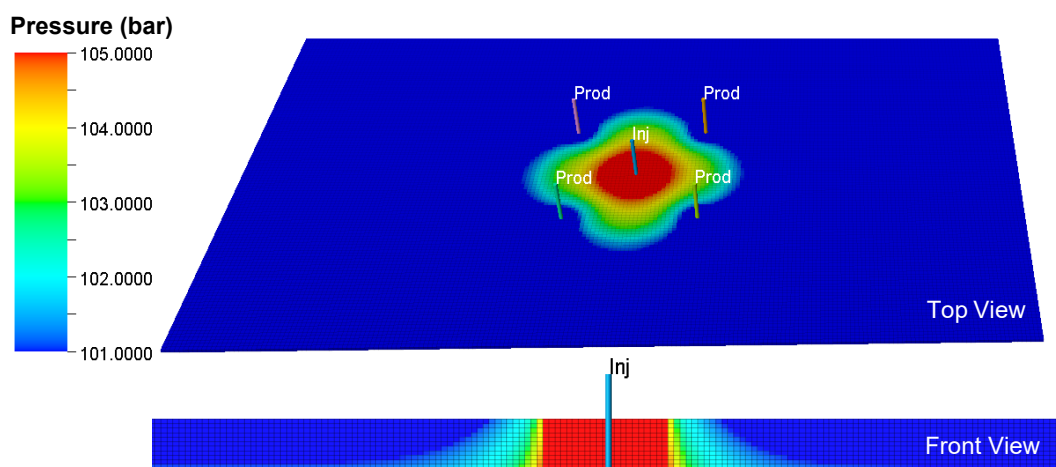

Figure 55: Injection pressure distribution, vert_small - base case – 2022.

Figure 56: Injection pressure distribution, vert_small - polymer solution – 2022.

Comparing these two cases indicate that the injection pressure propagation around the injector with polymer solution is farther, thus higher than that of the base case. The injection pressure however reduces farther away from the near wellbore region as the polymer flows towards the producers, equalizing with the reservoir pressure.

In the horizontal wells, lower injection pressure distributions are encountered compared to vertical wells as can be seen in Figure 57. The lower injection pressure is a result of the large contact area of the injector compared to that the vertical well. The maximum injection pressure of the base case for the horizontal well is 102.75 bar and

that for the polymer solution is 112.00 bar as can be seen in Figure 57 and Figure 58. In the polymer solution case, non-Newtonian effects are neglected. If the non-Newtonian effects are considered in the horizontal well, the effect will not be as strong as in vertical wells due to the lower flow rates in horizontal wells.
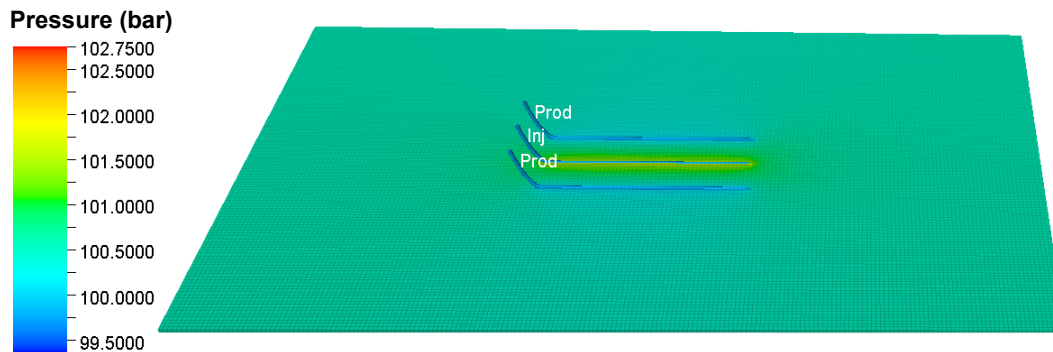

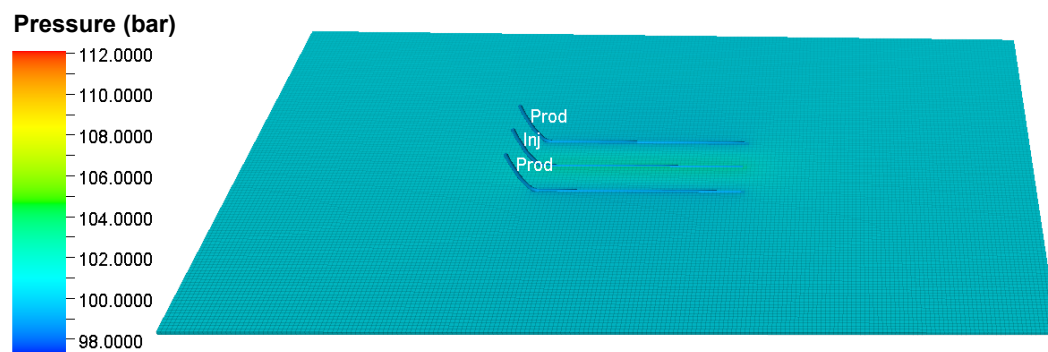Figure 57: Injection pressure, Hori_3 – base case – 2042.

Figure 58: Injection pressure, Hori_3 – polymer solution – 2042.

The injection pressure distribution of the polymer solution directly around the injector are clearly shown in Figure 59 (front view) and in Figure 60 (side view) with a range of 101 to 105 bar. Directly along the injector higher pressures are encountered as shown in these figures.
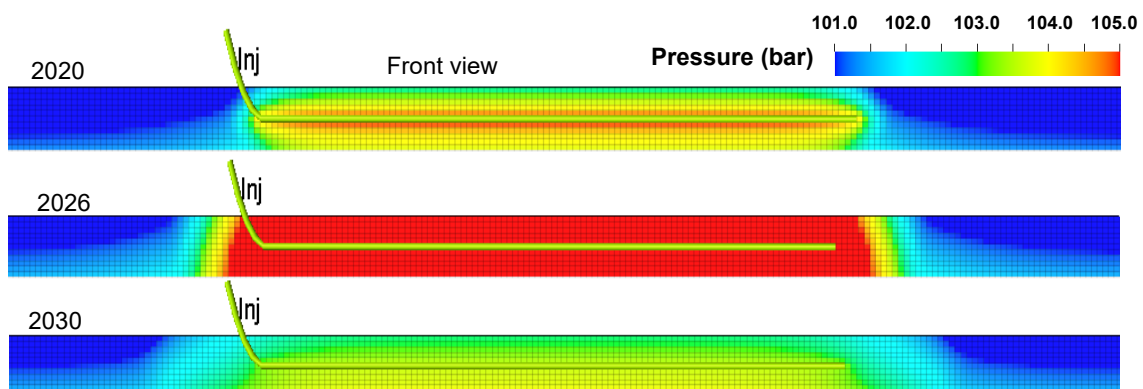

Figure 59: Injection pressure distribution along the injector - Hori_11 – polymer solution.

The injection pressure however declines with time as illustrated in Figure 60 at 2030. This figure shows the injection pressure distribution in relation to time, hence at year 2020, 2026 and 2030. The injection pressure declines after the slug size of the polymer solution has been injected and the polymer has dispersed. The driving fluid, which is injected after the polymer slug is water having a lower viscosity than polymer solution, hence a lower injection pressure propagation.
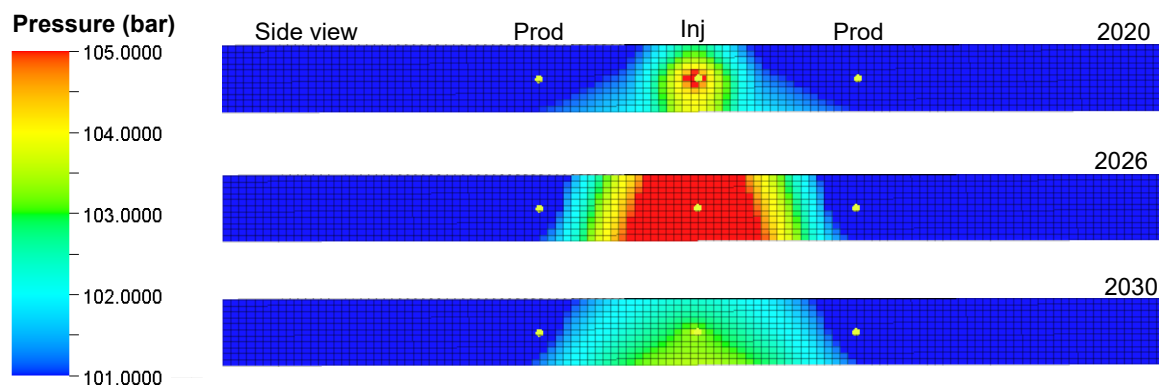

Figure 60: Injection pressure distribution across the wells - Hori_11 – Polymer solution.

6.1.2 Oil Saturation Distribution

In the course of displacement of oil by water and polymer solution, an oil bank is formed in front of the water and the polymer slug respectively. In water flooding, water easily bypasses oil because of its higher mobility. This leads to earlier water breakthrough. The polymer solution on the other hand targets the oil, which would be bypassed by water. However, since the polymer does not alter the residual oil saturation, the ultimate oil recovery of the moveable oil should be the same for both water and polymer flooding but over different timescales.(Sorbie, 1991 p. 250)

The lower mobility of the polymer solution generates a stable flooding front, which leads to the building of a steady oil bank – hence a piston-like displacement. This improves the areal sweep leading to a higher sweep efficiency. The polymer solution oil bank is more stable than that of water flooding. As a result, for a given timescale oil recovery is higher with polymer solution. This can be observed in the simulations with the oil saturation of the oil bank in the polymer flooding being higher than that of water flooding – base case. Figure 61 illustrates the oil saturation of the base case and Figure 62 that of polymer solution at 2022. The oil bank in front of the polymer slug can be seen clearly as the oil is swept in the direction of the producers.
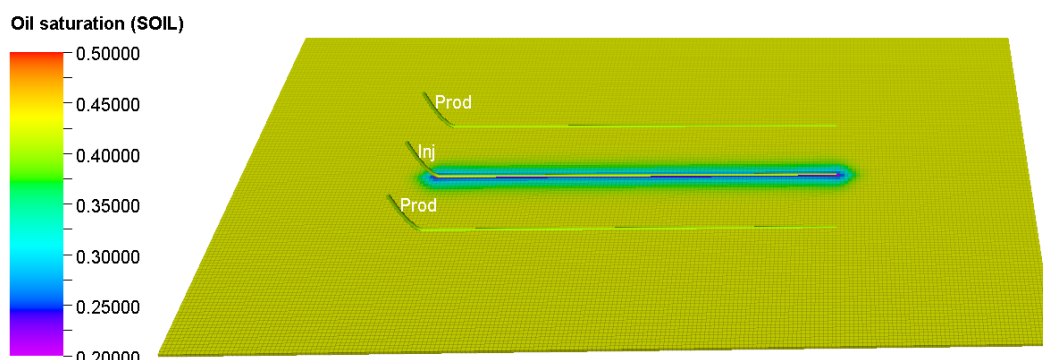

Figure 61: Oil saturation distribution, Hori_11 – base case – 2022.
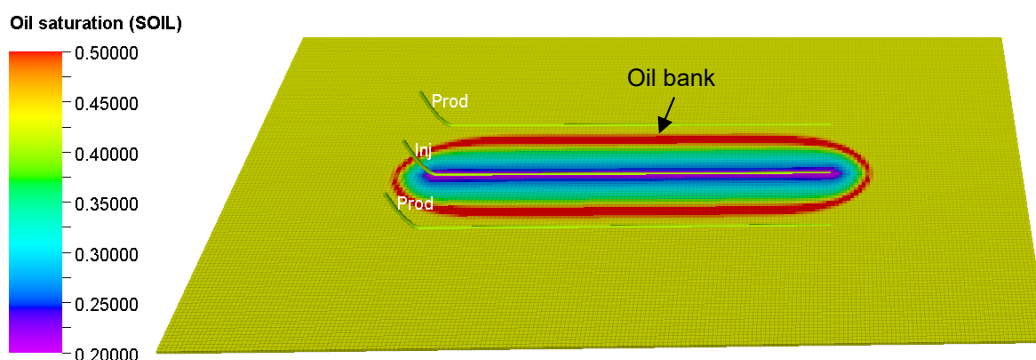

Figure 62: Oil saturation distribution, Hori_11 - polymer solution – 2022.

Figure 61 and Figure 62 show the magnitude of the oil saturation for both the base case and the polymer solution. It can be seen that the oil saturation in front of the polymer slug is much higher than that of the water flood. The oil bank in front of the polymer has a saturation of 0.5. Figure 63 show the cross section of the oil displacement through the polymer for the years 2020, 2026 and 2030.
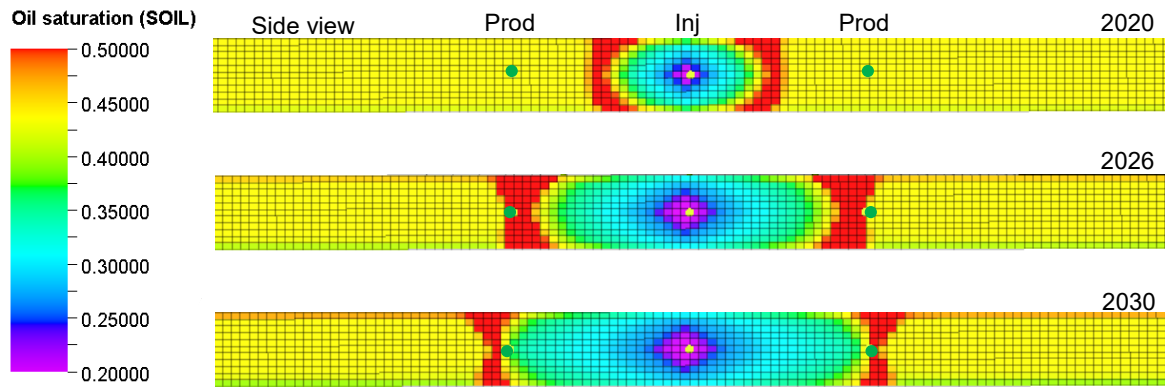
Figure 63: Oil displacement, Hori_11 - polymer solution – side view.

In Figure 63 the stable flooding front caused by the polymer solution can be seen boldly – hence piston like displacement, which compared to the water flooding as illustrated in Figure 64, is not the case. However, the lower oil saturation at the water flooding front can be attributed to dilution effects.
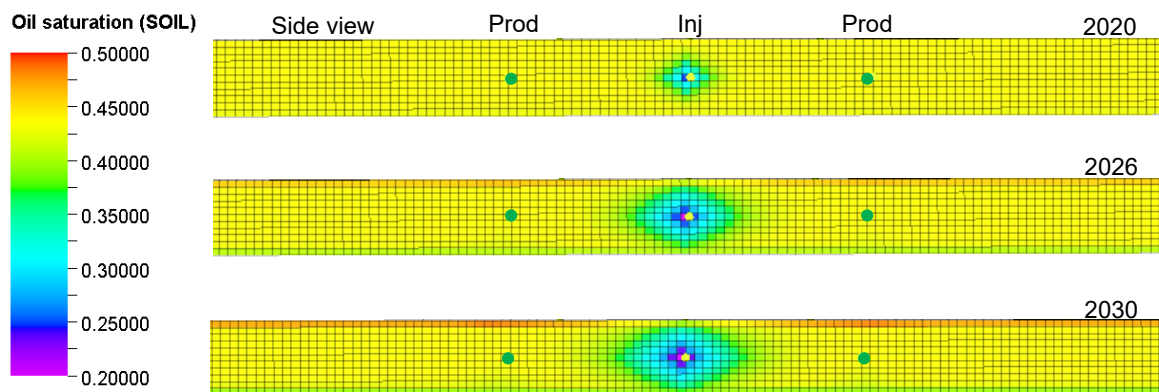
Figure 64: Oil displacement, Hori_11 – base case – side view.

6.1.3 Water Cut

The water cut, thus fraction of water produced relative to the total volume of liquids produced, for both water and polymer flooding can be seen in Figure 65 and Figure 66 respectively. It is observed that in the base case the water cut increases steadily, whilst in polymer flooding the water cut decreases initially before it starts to increase. This reduction in water cut is a result of the lower mobility ratio of the polymer solution, which enhances the sweep efficiency. Thus, in the base case, the mobility ratio of water higher, which accounts for the poor sweep efficiency. The reduction in the fraction of water during polymer flooding implies that, the oil saturation increases accounting for the higher oil production rate as can be seen in Figure 74.
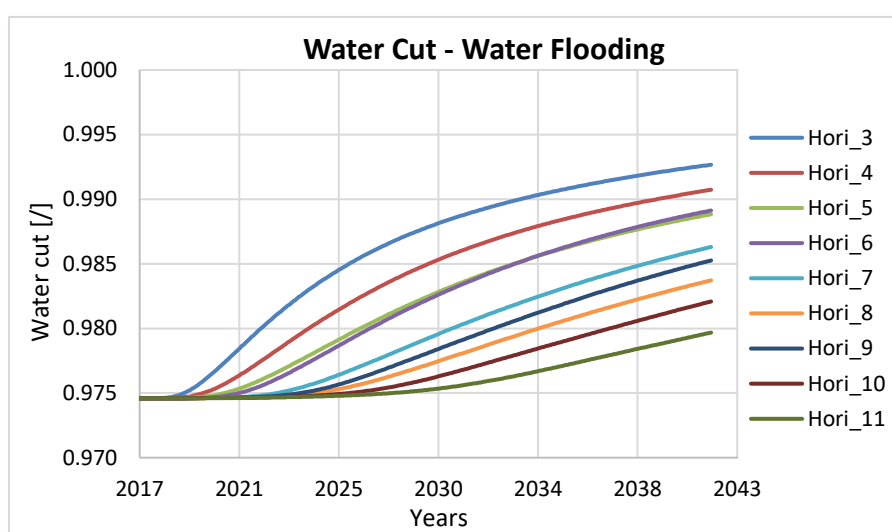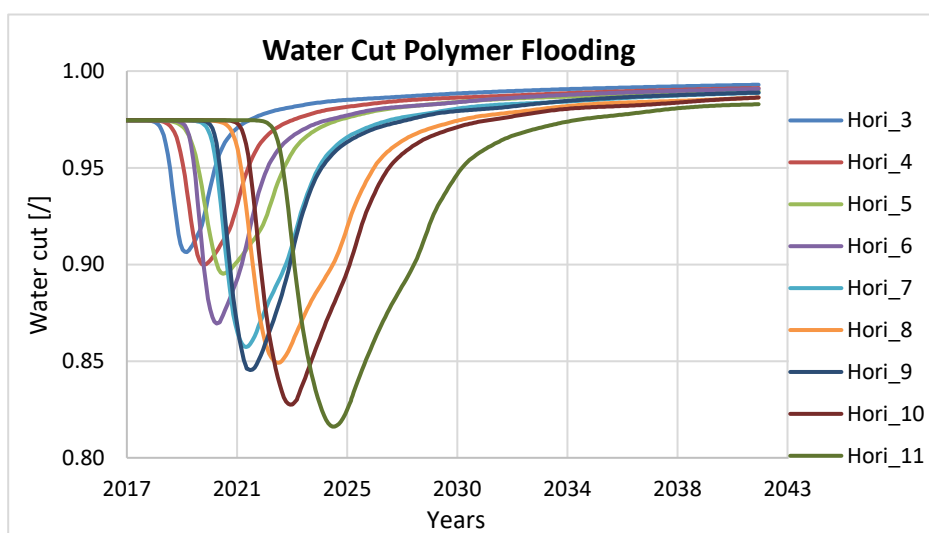

Figure 65: Water cut - water flooding.

Figure 66: Water cut - polymer flooding.

6.1.4 Polymer Cell Concentration and Adsorption

Through the interaction of the polymer with the rock surface, the polymer molecules are adsorbed onto the rock surface. This leads to a decrease in the in-situ polymer concentration and subsequently viscosity and water relative permeability reduction. Figure 67 illustrates the concentration of the polymer in the cells at year 2024. The polymer solution front can be seen clearly. The front possesses a transition zone where the polymer solution disperses with the reservoir fluid, hence lower concentration in this zone.
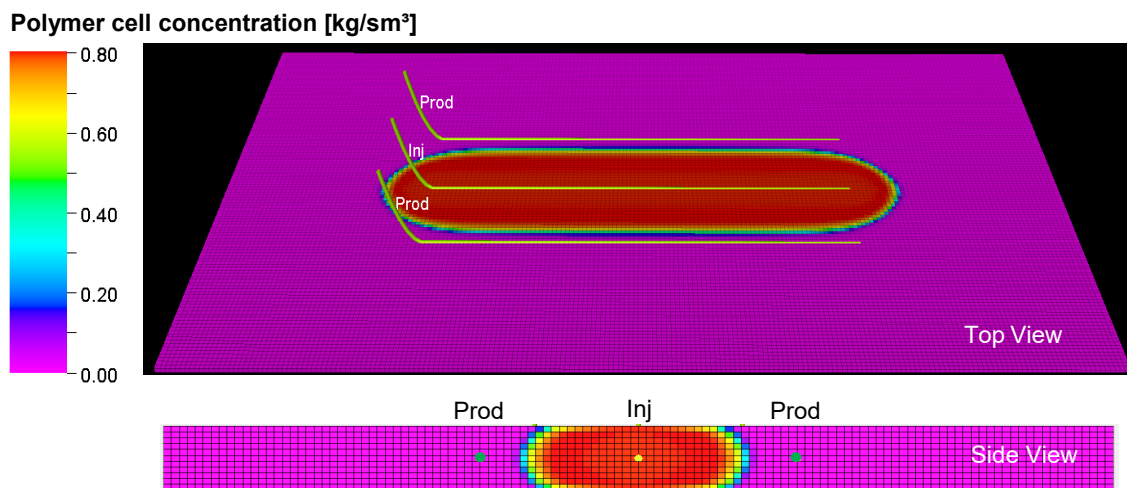

Figure 67: Polymer cell concentration, Hori_11 – 2024.

In 2026, as shown in Figure 68, the end of the of the polymer slug can be seen and simultaneously indicating the front of the driving fluid which contains no polymer. At the driving fluid front, there is also a transition zone where the polymer concentration is reduced through dispersion.
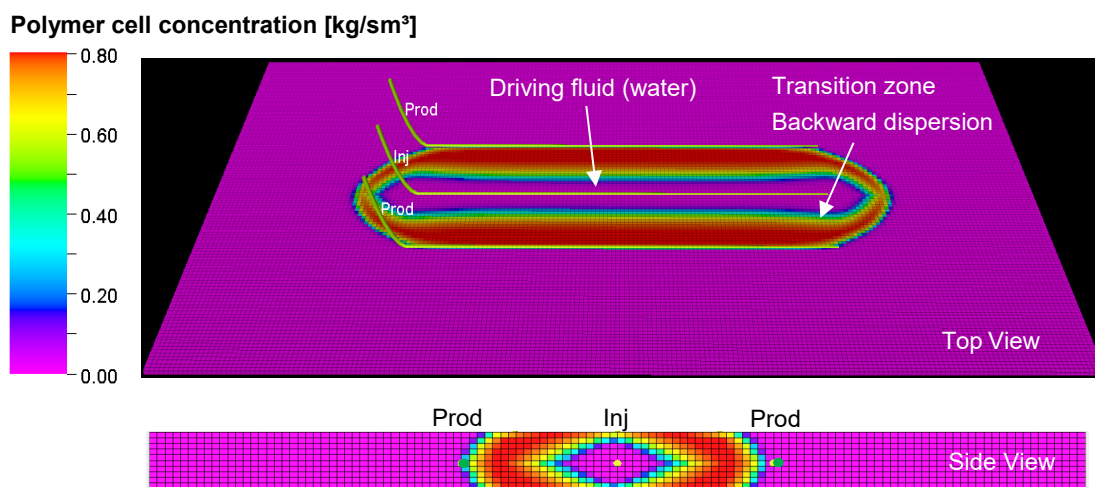

Figure 68: Polymer cell concentration, Hori_11 – 2026.

Figure 69 illustrates the mass polymer adsorbed per unit rock mass. Thereby through the adsorption shown in this figure, the flow path of the polymer solution can be observed. The mass of polymer adsorbed between the two producers depict that the maximum mass of adsorption has been reached. When the maximum mass of adsorption per unit rock mass is reached there is no more adsorption occurring. Desorption is not considered in these calculations.
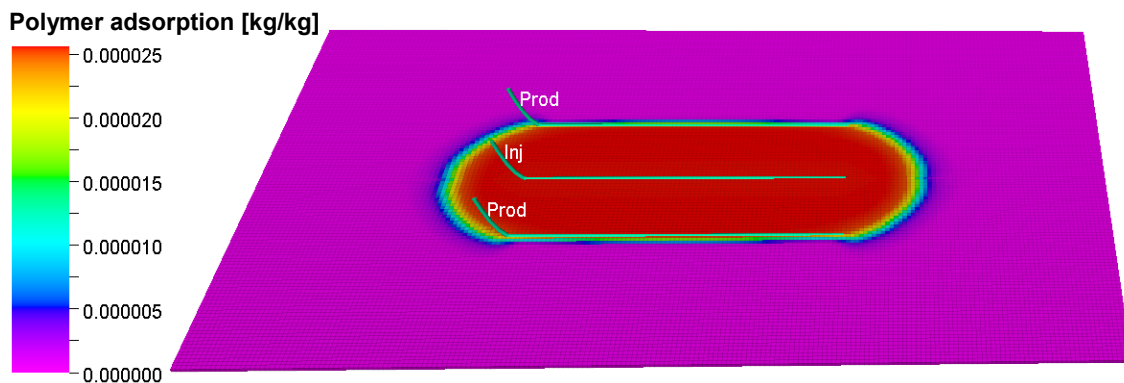

Figure 69: Polymer adsorption, Hori_11 - 2042

The total mass of polymer adsorbed per configuration increases linearly with increasing chemically affected reservoir volume (CARV). The total mass of polymer adsorbed for the horizontal wells are illustrated in Figure 70.
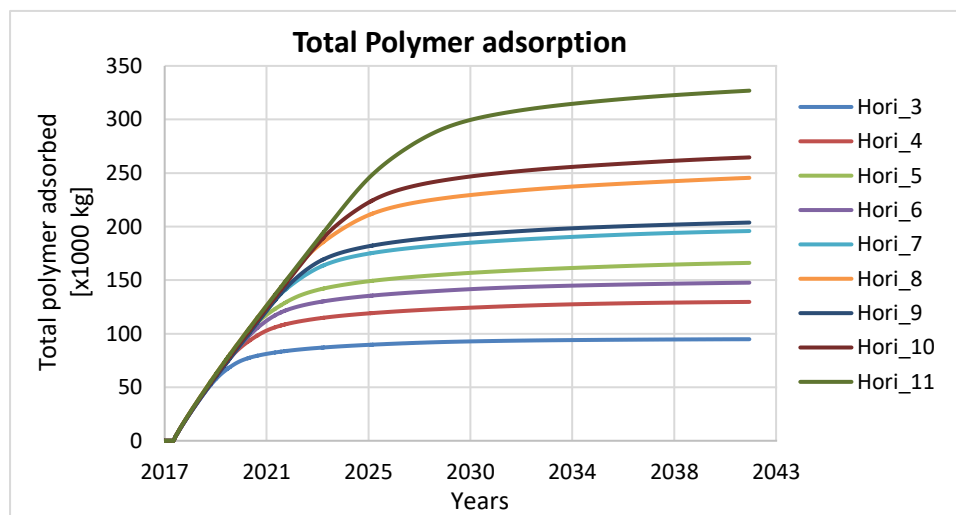

Figure 70: Total polymer adsorption.

Figure 71 shows the mass of polymer in the solution over time. The mass of the polymer in the solution decreases over time through adsorption and production. At the end of the injection, i.e. in 2042, there are residual polymers in the solution. In the larger configurations – Hori_8, Hori_10 and Hori_11 – the residual mass of polymer in

the solution is quite significant. In Hori_8 and Hori_10 the residual mass of polymer is about 35,000 kg and in the largest configuration, Hori_11, about 90,000 kg.
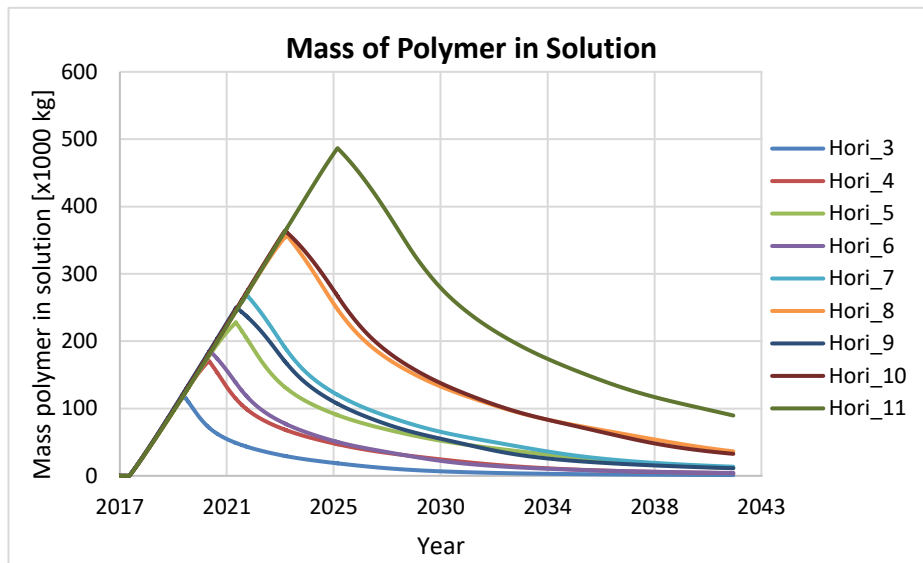

Figure 71: Mass of polymer in solution.

Figure 72 and Figure 73 show the cumulative mass of polymer injected and produced respectively. With an injection rate of 300 m³/day and a polymer concentration of 800 ppm, the mass of polymer injected per day is 240 kg. The duration of the polymer injection depends on the pore volume of the configuration. The pore volume of polymer injected is 0.8. In the smallest configuration, Hori_3, the amount of polymer injected is about 196,000 kg, whilst in the largest, Hori_11, about 743,000 kg is injected.
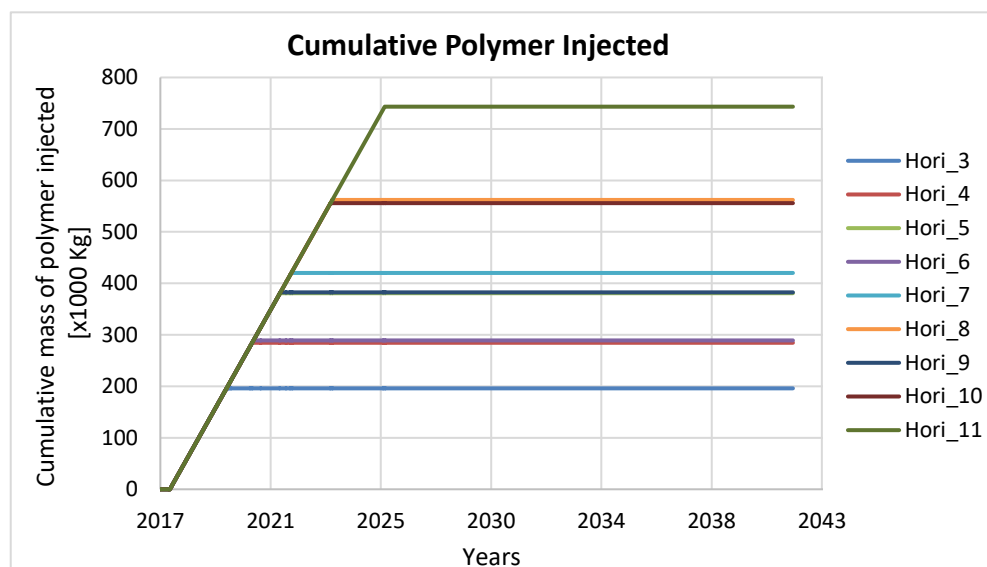

Figure 72: Cumulative mass of polymer injected.

The time of polymer production begin and the amount of polymer produced also depend on the pore volume, polymer adsorption and the mass of polymer remaining

in the solution. In Figure 73, it can be seen that, the polymer production response time in Hori_3 is the earliest at year 2019 and the latest is in Hori_11 at year 2025 after injection begin. Cumulative polymer production of Hori_3 is about 100,000 kg and that of Hori_11 about 326,000 kg. Comparing these to the amount of polymer injected, indicate that 51% of the injected mass is produced in Hori_3 and about 44% in Hori_11 over the 25 years of flooding. The difference owes to polymer adsorption and mass of polymer in the solution. It should be noted however, that the smaller configurations reaches their production plateaus earlier than then larger ones accounting for the lower percentage polymer production within the 25 years.
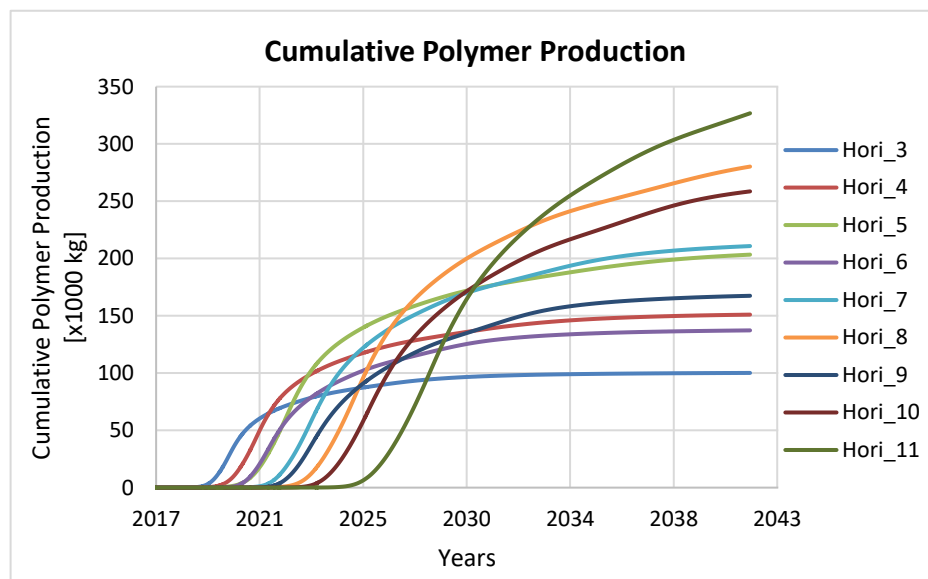

Figure 73: Cumulative mass of polymer produced.

6.1.5 Incremental Oil Recovery

The incremental oil recovery is used in assessing the improvement of oil recovery efficiency of polymer flooding over water flooding. As stated earlier, theoretically both flooding mechanisms would produce all the moveable oil however, on different time scales. (Sorbie, 1991 p. 250) Consequently, at a given time or pore volume (PV) of injection, the increase in oil recovery through polymer over water flooding describes the incremental oil recovery. Figure 74 compares the cumulative oil production and oil production rate of water and polymer flooding as a function of pore volumes injected for Hori_9.
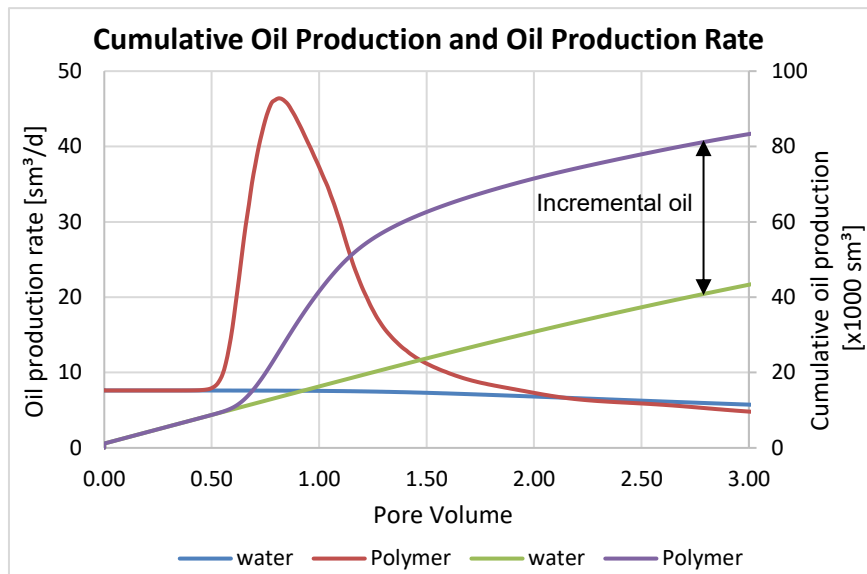
Figure 74: Cumulative oil production and oil production rate, Hori_9.

The differential oil production rate between the base case and polymer flooding as a function of PV injected can be seen in Figure 75. As can be seen in Figure 74 from 2 PV till 3 PV the difference in oil production rate between the base case and polymer flooding becomes negative because the polymer oil production rate declines below that of water flooding after a certain amount of pore volume has been flooded. Therefore, from the economic point of view and the fact that flooding is typically limited by time, it is ideal to flood until 3 PV is reached.
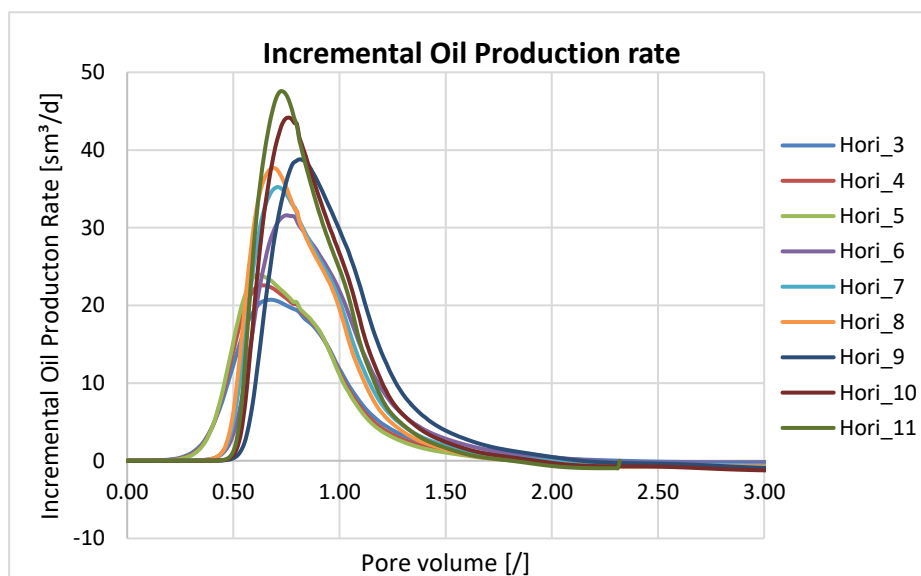

Figure 75: Incremental oil production rate between polymer and water flooding.

The incremental oil production rate, as seen in Figure 75, increases with increasing CARV. Within a set of configuration (Hori_3, Hori_4 and Hori_5) however, the difference in incremental oil production rate is not as significant as between two

configuration sets. For example, the difference in incremental production rate at peak production between Hori_5 and Hori_8 is about 14 sm³/d and between Hori_8 and Hori_11 is about 10 sm³/day. The difference however, between Hori_3, Hori_4, and Hori_5 within the same configuration set is about 1 sm³/d.

In Figure 76, the incremental oil recovery of the configurations can be seen as a function of the pore volume injected. Hori_11 could only be flooded for 2.32 PV in the 25 years as seen in this figure. This is because of its relatively large volume. It is observed that the lowest incrmental oil recovery is obtained in the smallest configuration (Hori_3) or CARV and the highest in the largest configuration (Hori_1).
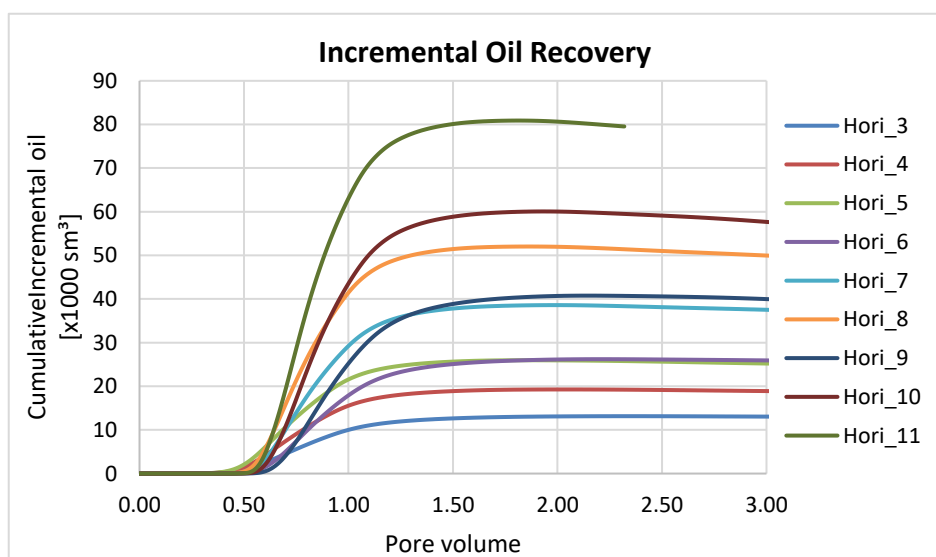

Figure 76: Incremental oil recovery of the configurations.

It is expected that under the circumstance that all reservoir parameters being equal with the exception of the CARV, that the oil recovery should increase proportionally with increasing CARV. Investigations in 1D confirm this, however, it is not true in 3D. In order to find out how the CARV relates to the oil recovery, two approaches are considered. In the first approach, the distances between the wells are fixed (210, 310 and 410 m), and the lengths varied. In the second, the well lengths are fixed and the distances varied. The pore volumes of the smallest configuration in the set of the three models are then set in relation to the other two PVs of the configurations in the set. Hence, the lager PVs are normalised on the smallest PV in a configuration set. The same is also done for the respective oil recovery. Table 9 illustrates the results of the first approach, whilst Table 10 shows the results of the second. Np in the tables represent incremental oil recovery and Npi the smallest incremental oil recovery. PVi represent the smallest PV in the configuration set and Npi the corresponding incremental oil recovery.

Table 9: PV and oil recovery, normalized for fixed well distance and varying lengths.

Model	PV	Np* (1D) [sm³]	Np* (3D) [sm³]	PV/PVi**	Np/Npi*** (1D)	Np/Npi*** (3D)
Hori_3	306,075	1899	20,369	1.00	1.00	1.00
Hori_4	444,675	2743	29,038	1.45	1.44	1.43
Hori_5	594,825	3648	38,281	1.94	1.92	1.88
Hori_6	451,825	2845	31,818	1.00	1.00	1.00
Hori_7	656,425	4121	45,305	1.45	1.45	1.42
Hori_8	878,075	5481	59,514	1.94	1.93	1.87
Hori_9	597,575	3857	43,958	1.00	1.00	1.00
Hori_10	868,175	5501	61,362	1.45	1.43	1.40
Hori_11	1161,325	6030	65,701	1.94	1.56	1.49

Table 10: PV and oil recovery, normalized for fixed well length and varying distances.

Model	PV	Np* (1D) [sm³]	Np* (3D) [sm³]	PV/PVi**	Np/Npi*** (1D)	Np/Npi*** (3D)
Hori_3	306,075	1898.572	20,369	1.00	1.00	1.00
Hori_6	451,825	2844.56	31,818	1.48	1.50	1.56
Hori_9	597,575	3857.032	43,958	1.95	2.03	2.16
Hori_4	444,675	2743.421	29,038	1.00	1.00	1.00
Hori_7	656,425	4120.589	45,305	1.48	1.50	1.56
Hori_10	868,175	5500.843	61,362	1.95	2.01	2.11
Hori_5	594,825	3648.226	38,281	1.00	1.00	1.00
Hori_8	878075	5481.252	59,514	1.48	1.50	1.55
Hori_11	1161325	6030.001	65,701	1.95	1.65	1.72

* Incremental oil recovery

** Smallest pore volume in configuration set

*** Smallest incremental oil recovery

The corresponding plots of the first and second approach can be seen in Figure 77. The points marked 2.32 PV represent Hori_11 where only 2.32 of the pore volume could be injected within 25 years, whilst the rest are at 3.0 PV.
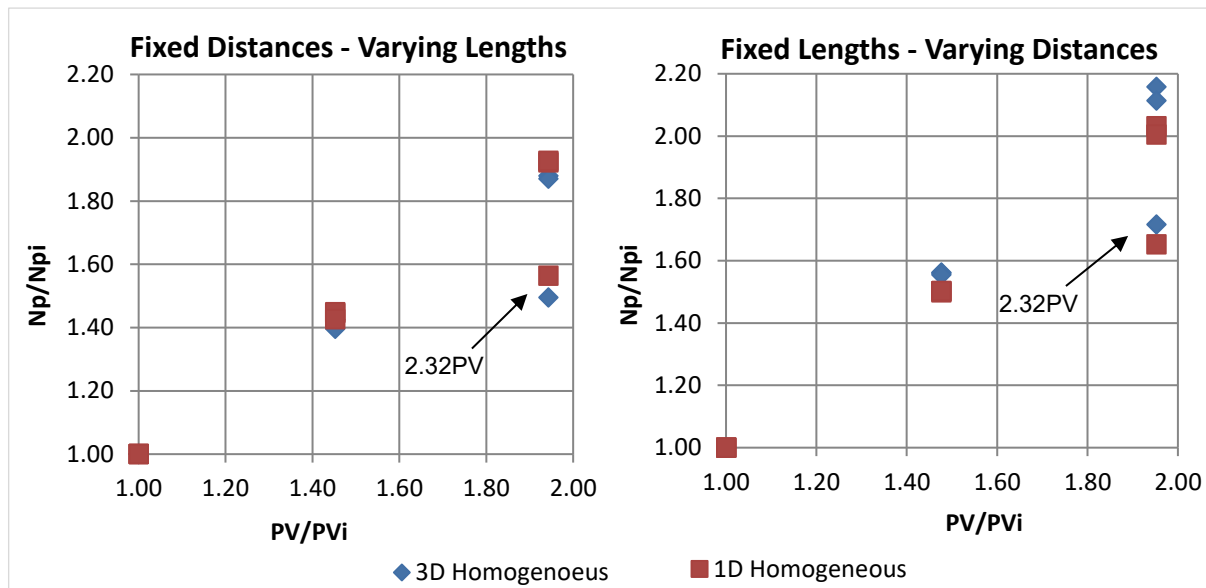
Figure 77: Trend of varying well lengths and distances.

From these plots, it can be seen, that incremental oil scales linearly with CARV. These two plots depict clearly as can be seen, that in 1D, the incremental oil in both approaches is almost the same. However, in 3D there is a significant difference between the two. It is observed, that higher incremental oil is achieved in the second approach – fixed lengths with varying distances – than in the first. This would mean that recovery is higher in well configurations with larger distances. The reason is the drainage area, which in this work is approximately the area between the producers. However, in reality the drainage area has an elliptical shape and increases faster when the distance between the wells increases compared to increasing the well length. By setting the permeability in y - and z – direction to zero, thus 1D, the drainage area becomes rectangular and therefore both approaches converge. This means for a given CARV, without the consideration of economics, it is better to keep the wells short and design the distance larger than drilling a longer well with a smaller distance.

6.2 Heterogeneous Case

The results in this section are based on the high permeability contrast models described under heterogeneous model description. Furthermore, the results presented here are limited to well configuration Hori_10 at polymer concentration of 800 ppm, if not stated otherwise. Simulations were also carried out for 1200 ppm and 1600 ppm.

Different permeability distributions generate different injection pressure propagation in the reservoir. As observed earlier in the homogeneous calculations, the injection pressure distribution induced by water flooding is likewise lower than those induced by the polymer solution. However, in the case of the heterogeneity, the injection pressure distributions experienced here are much higher than those of the homogeneous cases. Because of the high permeability contrast, the influx of polymer solution in high permeability areas causes higher pressure drops in these areas leading to crossflow. The maximum and minimum pressures of the eight different geological realizations developed in Hori_10 can be seen in Table 11 and in Figure 78 in a cluster column.

Table 11: Minimum and maximum injection pressure distribution – 800 ppm.

Model	Injection Pressure Distribution [bar]			
	Base Case		Polymer Solution	
	Minimum	Maximum	Minimum	Maximum
CL500_250_AZ90	95	107	85	131
CL250_125_AZ90	94	105	80	125
CL500_125_AZ90	93	104	95	125
CL500_250_AZ00	92	112	80	154
CL250_125_AZ00	94	110	85	140
CL500_125_AZ00	95	106	90	128
CL125_62.5_AZ90	92	108	80	137
CL125_62.5_AZ00	96	106	90	127

From Table 11 and Figure 78, comparing the models, each model with its specific counter-model, it can be observed that the models with variogram having an azimuth of 0° have higher injection pressure distributions than those with 90°, with the exception of CL125_62.5. The reason might be due to the aspect ratio between the well length and the distance between the wells. Thus, with the variograms or channel bars lying parallel to the wells, lower pressures occur as compared to channels perpendicular to the wells as the polymer solution flows along the longer lengths of the well.

Furthermore, the maximum injection pressures reached are all below the formation parting pressure of 180 bar and hence allowing flooding under matrix conditions as expected.
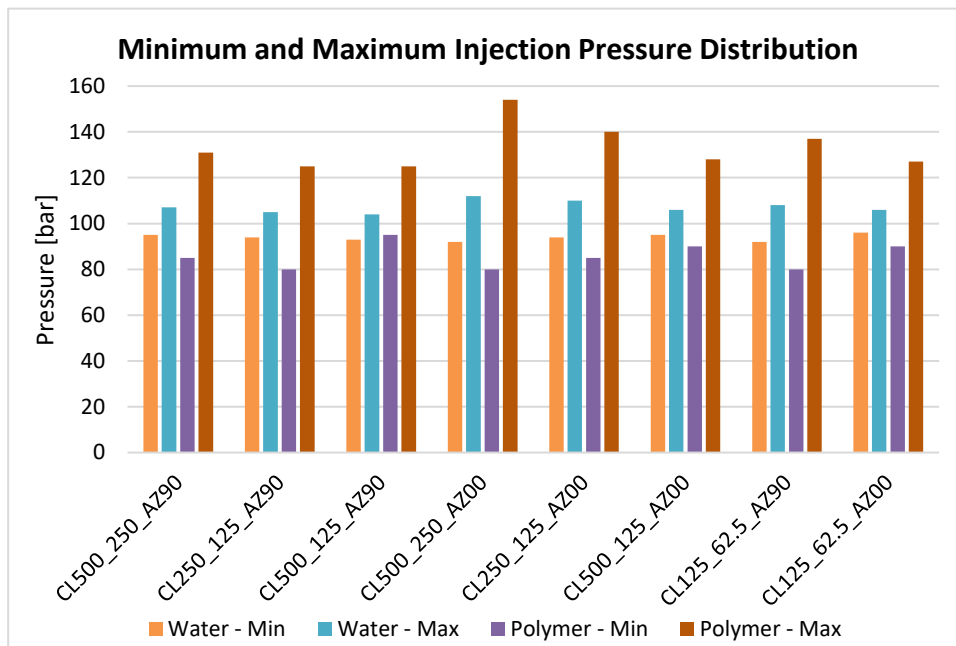

Figure 78: Minimum and maximum pressure distribution - high permeability contrasts.

Figure 79 and Figure 80 illustrate the polymer solution injection pressure distribution of CL500_250_AZ90 and CL500_250_AZ00 between the range of 101 and 105 bar at 2030, comparing the injection pressure propagation of the model with an azimuth of 90° and to that of 0°.
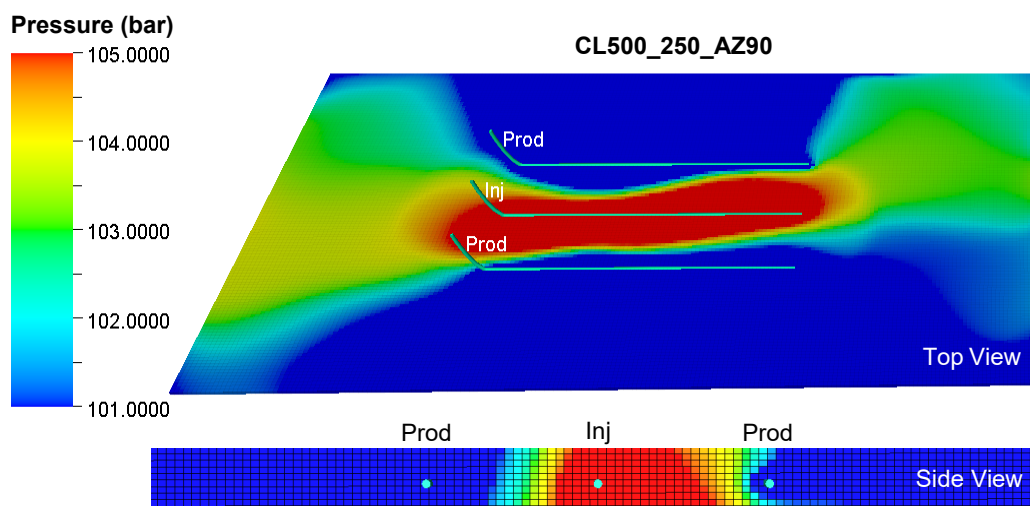
Figure 79: Injection pressure distribution, Hori_10 – CL500_250_AZ90 – 2030.
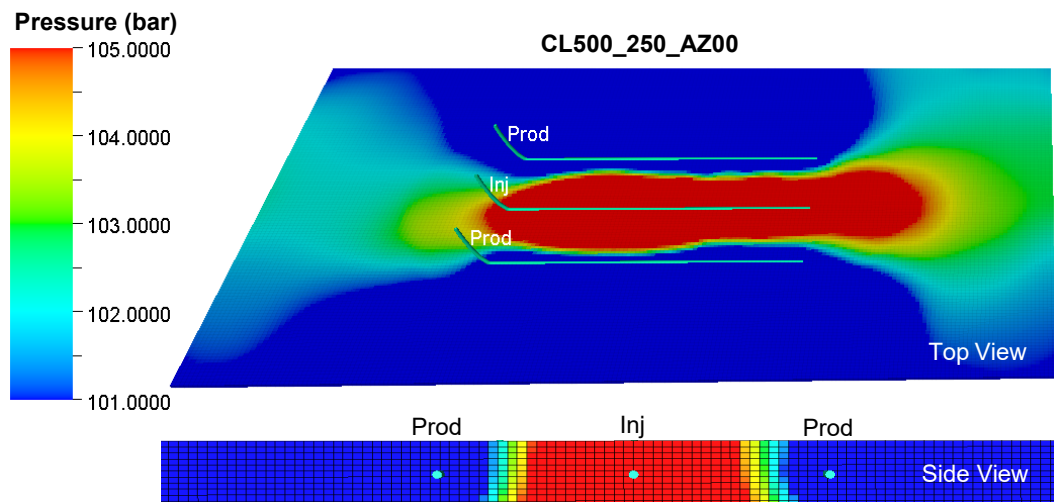
Figure 80: Injection pressure distribution, Hori_10 – CL500_250_AZ00 – 2030.

The oil saturation, water cut, polymer cell concentration and the polymer adsorption of the investigated heterogeneous models follow similar trends as observed in the homogeneous cases. Their corresponding distributions can be found in Appendix D.

The incremental oil recovered in the eight geological models can be seen in Figure 81, Figure 82 and Figure 83. From these plots, it is observed that, the geological models with an azimuth of 90°, thus the correlations lengths or the channel bars parallel to the wells, yielded higher incremental oil than those with 0° azimuth.
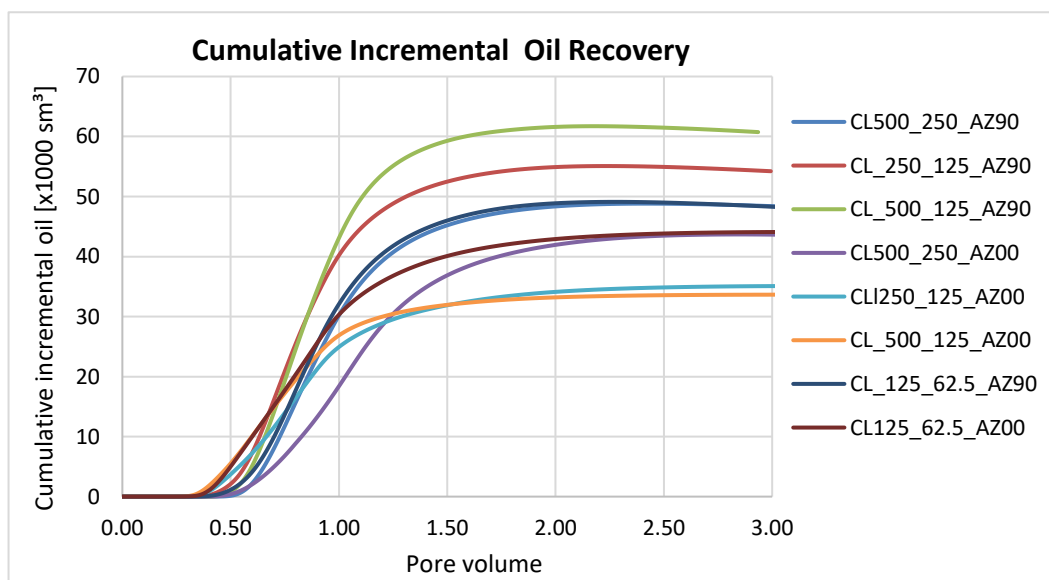
Figure 81: Incremental oil recovery at 3 PV, 800 ppm.

In the base case, thus water flooding, as expected, the geological models with azimuth 0° have lower oil production due to earlier water breakthrough. During polymer injection, it is observed that the incremental oil recovery in the models with azimuth 90° are also higher than those with azimuth 0°.

However, by increasing the polymer concentration, from 800 ppm to 1200 ppm and to 1600 ppm, it can be seen that the difference in recovery between azimuth 0° and 90° decreases as can be seen in Figure 84. In Figure 82, the incremental oil recovery factor of the geological models with their respective azimuth can be seen. This plot shows that with the exception of CL500_250_AZ00 all of the models with 90° azimuth have higher incremental oil recovery.
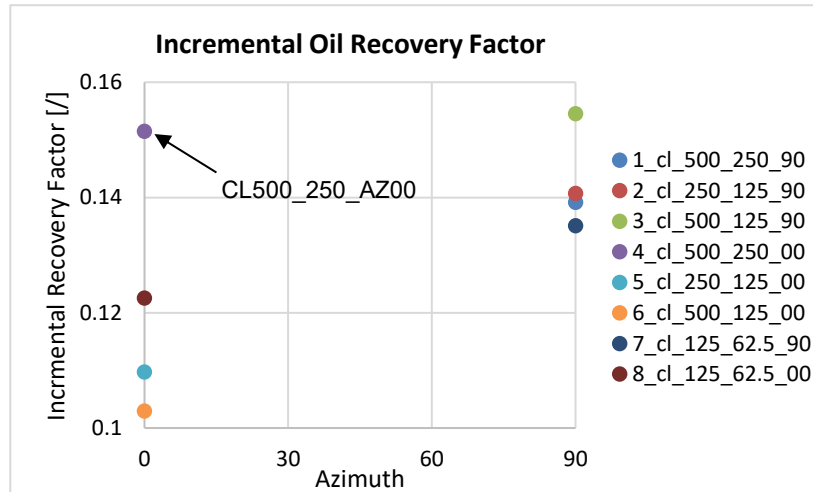

Figure 82: Incremental oil recovery against azimuth for 800 ppm polymer concentration.

Figure 83 compares the cumulative incremental oil recovery for 800, 1200 and 1600 ppm polymer concentration. It can be observed that increasing the polymer concentration increases the incremental oil recovery. Increasing the polymer concentration increases the viscosity of the solution and thereby further decreases the mobility ratio, providing a more stable front as well as acceleration and thereby accounting for the much better displacement.
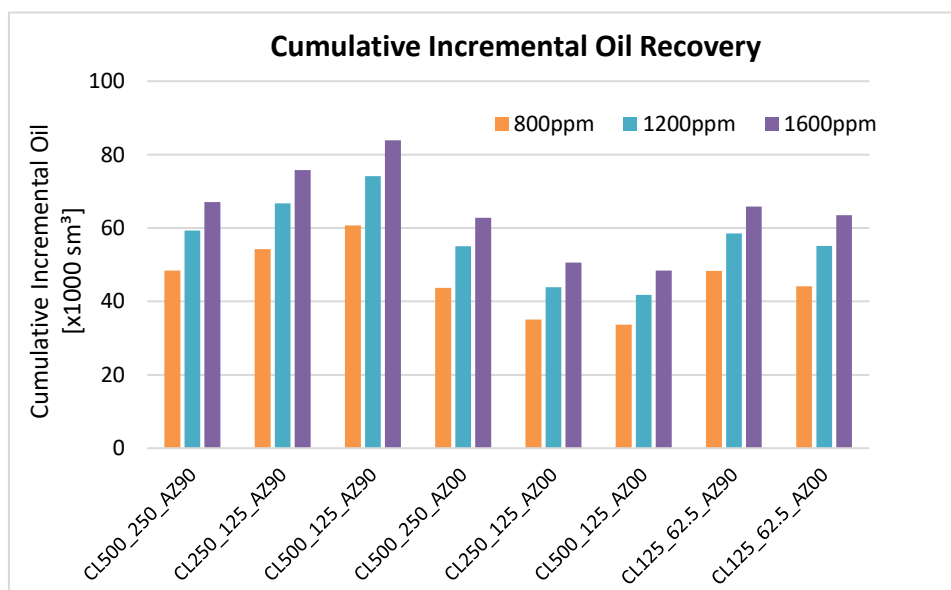
Figure 83: Cumulative incremental oil recovery at different polymer concnetrations.

The incremental oil recovery factor – ratio of the cumulative incremental oil recovery to the oil initially in place – achieved with the three different polymer concentrations can be seen in Figure 84. This plot shows that the incremental oil recovery factor increases with increasing polymer concentrations. The effect of the incremental oil recovery factor for higher concentrations is not as strong as that of lower concentrations. This can be observed by comparing the slope between 800 ppm and 1200 ppm to the slope of 1200 ppm and 1600 ppm. The slope between 1200 ppm and 1600 ppm is not as steep as that between 800 ppm and 1200 ppm.
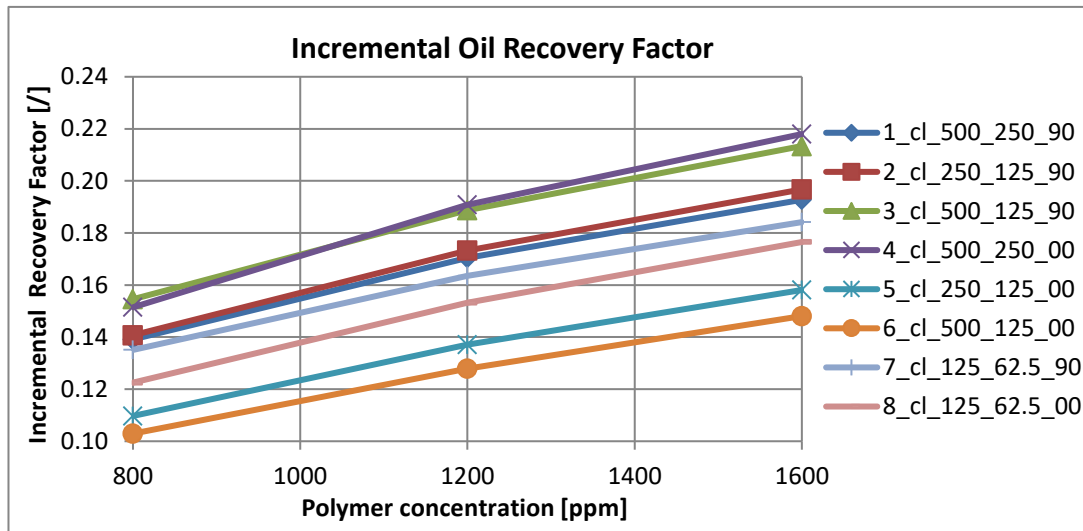
Figure 84: Incremental recovery factor - 800, 1200 and 1600 ppm.

Figure 85 compares the incremental oil recovery factor of the models with their corresponding azimuth for 800, 1200 and 1600 ppm. It can be observed that all three polymer concentrations have higher oil recovery in azimuth 90° with the exception of geological model CL500_250_AZ00 being the only outlier in in all three polymer concentrations. The points in the plot for each polymer concentration represent the eight different geological realizations.
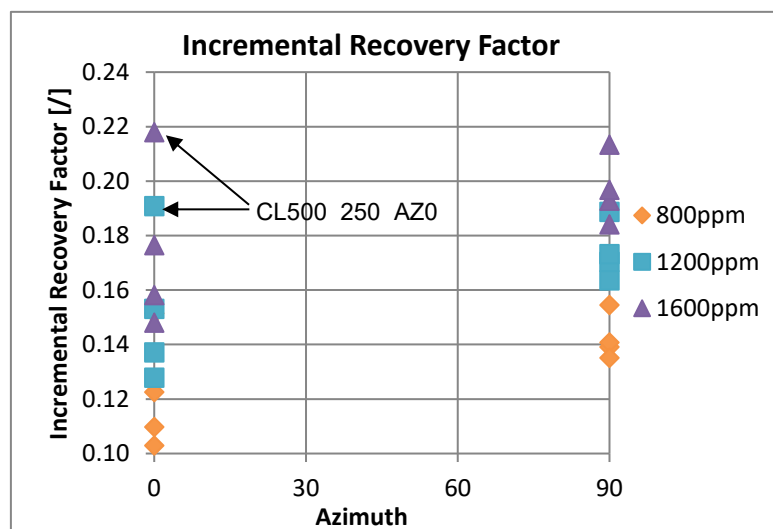

Figure 85: Incremental recovery factor against azimuth.

Considering the geological configurations with varying distances and well lengths of the horizontal wells, separate simulations with moderate permeability contrasts were carried out. Using the same approaches as shown in Table 9 and Table 10 – fixed well distance varying lengths and fixed well lengths varying distances – the results are can be seen in Figure 86. In this plot it can be clearly seen that increasing the distance between the wells leads to higher oil recovery in heterogeneous cases as well. Thus as explained in the homogeneous case under incremental oil recovery, the elliptical shape of the drainage area of horizontal well increases more rapidly with increasing well distance as compared to increasing well length. This implies that it is better to go for wells with increasing distances than those with longer wells. The encircled points represent the largest well configuration (Hori_11), which within the 25 years of injection reached a PV of 2.32. The rest of the points are related to oil recovery at 3 PV.
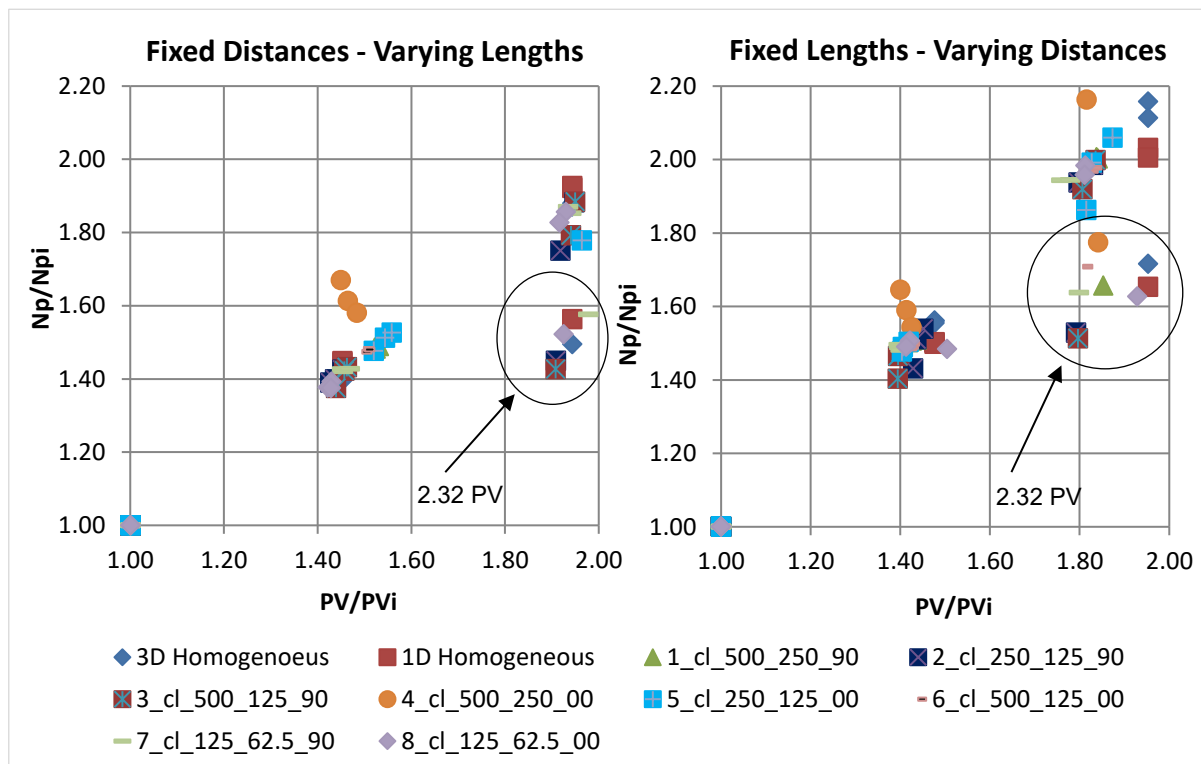
Figure 86: Trend of varying well lengths and distances.

Chapter 7:   Economics

Results from the homogeneous and heterogeneous simulations have shown that horizontal well configurations with increasing distances between the producers generate higher oil recoveries. The calculations in this section are based on the results of the homogenous simulations. It has also been observed that the incremental oil scales linearly with the chemically affected reservoir volume (CARV). However, the amount of polymer consumed in producing the incremental oil has not yet been discussed. The efficiency of the polymer injected can be rated using the utility factor (UF), which is the mass of polymer injected per incremental oil produced in bbl. The aim is to achieve an UF as low as possible.

Figure 87 shows the utility factor calculated for the homogeneous cases at 800 ppm polymer concentration for the different well configurations and the duration of the polymer injection in years. It can be seen that the UF decreases with increasing CARV and within a set of configuration, for example Hori_3, Hori_4 and Hori_5, the UF stays almost constant. The duration of polymer injected however, increases with increasing CARV – hence the polymer slug is linearly proportional to the pore volume. Therefore, the shortest polymer injection is Hori_3 with 2.24 years and the longest injection duration in Hori_11 with 8.5 years.
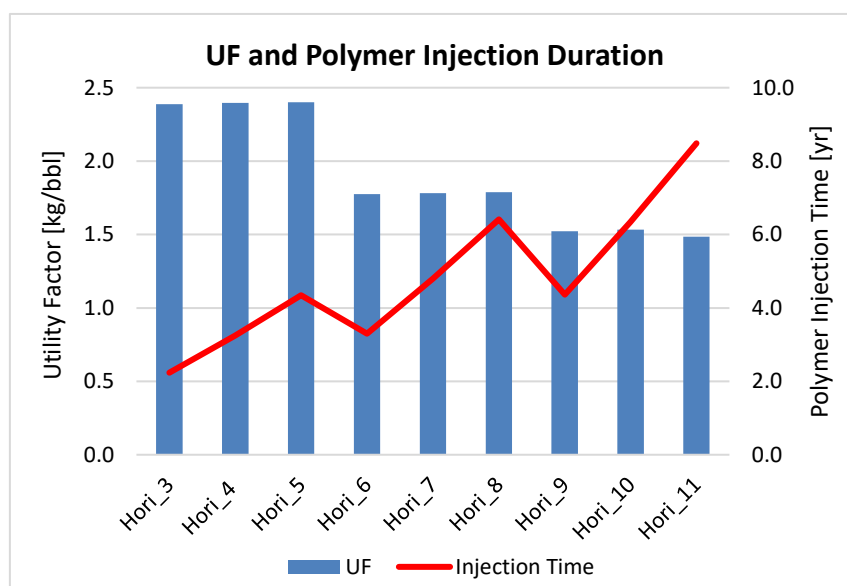

Figure 87: Utility factor (UF) - homogeneous cases

Incorporating economic aspects into the calculations requires the consideration of the capital (capex) and operational expenditure (opex) as well as the present value of the produced oil. The present value requires the produced oil to be discounted over the 25 years of flooding. Discounting is essential because of the loss in value of the production in the future from today's standpoint. The capital expenditures considered here are mainly the drilling and completion costs whilst under operational costs only the cost of

polymer is taken into account. The sum of the capex and opex is the technical cost. The total technical cost per cumulative incremental oil produced gives the unit technical cost (UTC). Using the results of the homogeneous simulations, the oil produced is discounted at a rate of 10% for 25 years. By means of equation 52 the present value (PV) of the production is calculated.

$$PV = \frac{FV}{(1+i)^t} \qquad\qquad 52$$

where FV is the future value, i the discount rate and t the number of years to be discounted (Newendorp and Schuyler, 2014). Figure 88 illustrates the discounted cumulative incremental oil produced in barrels, which is achieved by cumulating the present values at a unit dollar per barrel oil. Figure 89 shows the undiscounted cumulative incremental oil production in barrels.
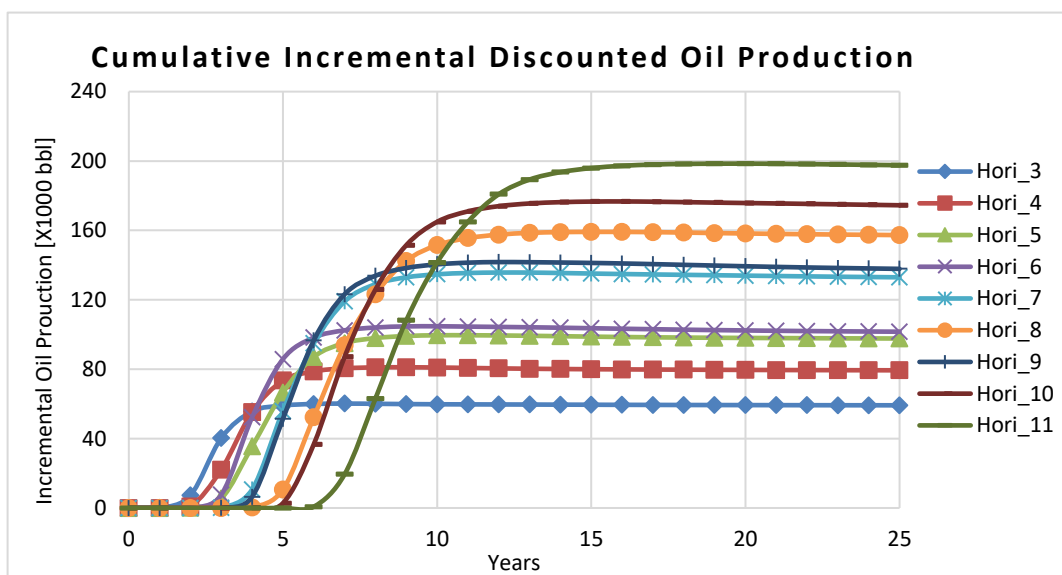
Figure 88: Cumulative incremental discounted oil production
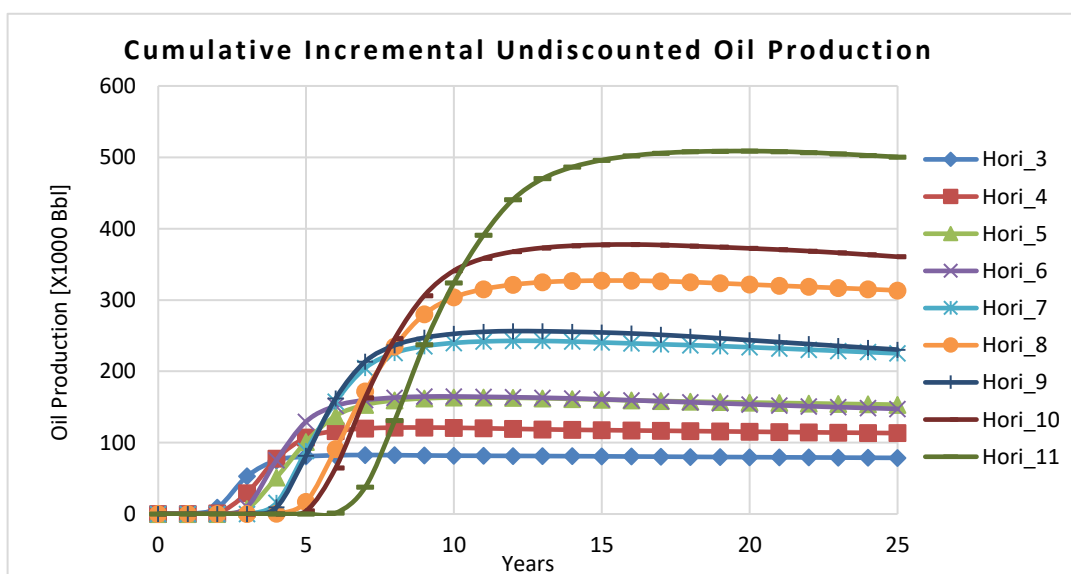
Figure 89: Cumulative incremental undiscounted oil production.

Figure 90 shows the percentage difference between cumulated incremental undiscounted and discounted oil production. It can be seen that the larger the CARV the higher the loss in value due to discounting. The percentage difference is at lowest at 24.8% for the smallest CARV, thus Hori_3, and the highest at 60.5% for the largest configuration – Hori_11.
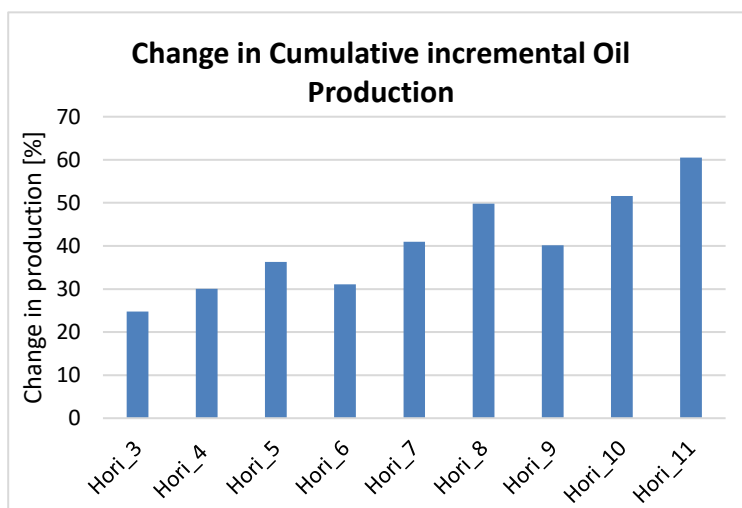

Figure 90: Percentage change between undiscounted and discounted cumulative incremental oil production.

At a polymer price of 3$ per kilogram, the undiscounted opex in injecting the 0.8 PV polymer slug at a concentration of 800 ppm are in the order of $590,000 for the smallest CARV and $2.2 million for the largest. Discounting the polymer costs by calculating the future value causes an opex in the order of $617,000 for the smallest and $2.3 million for the largest. The drilling and completion costs, making up the capital costs, are estimated to be $1200 per running meter. The costs involved in drilling and completion range from $7.6 million for the smallest CARV and $9.4 million for the largest. Figure 91 illustrates the technical cost - the sum of opex and capex - of the different configurations.
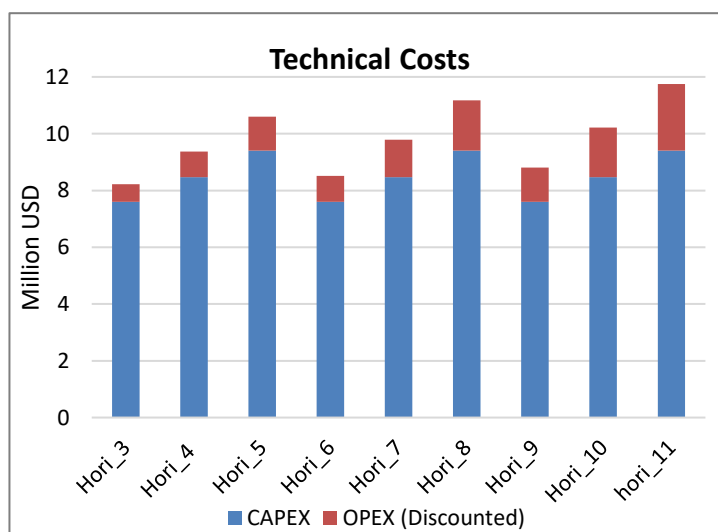

Figure 91: Technical costs of the configuration

Relating the technical costs to the cumulative incremental barrels of oil gives the unit technical cost, which indicates the cost it takes to produce a barrel of oil. Plotting the unit technical cost against the lengths of the wells, shows that the UTC declines with increasing well length as seen in Figure 92 for the three distances between the wells.
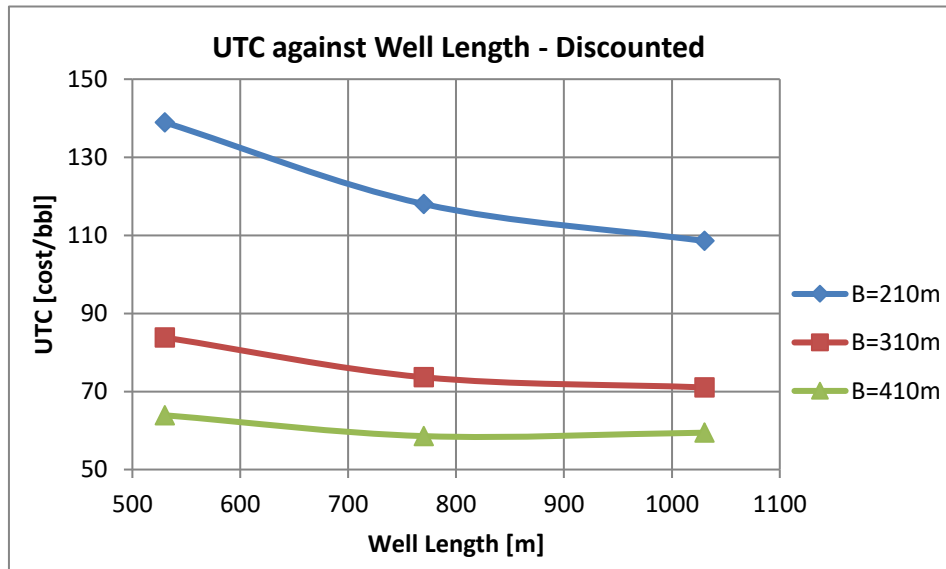

Figure 92: Unit technical cost versus the length of well - discounted.

Comparing the UTC on the basis of discounted cumulative incremental oil production to the undiscounted UTC, it is observed in Figure 93 that, the undiscounted UTC per well length is lower than the discounted. This is because the undiscounted incremental oil is much higher than the discounted and moreover the difference between the undiscounted and discounted technical costs is practically insignificant. As a result, the undiscounted UTC becomes lower than the discounted. The difference is in the order of 30$/bbl.
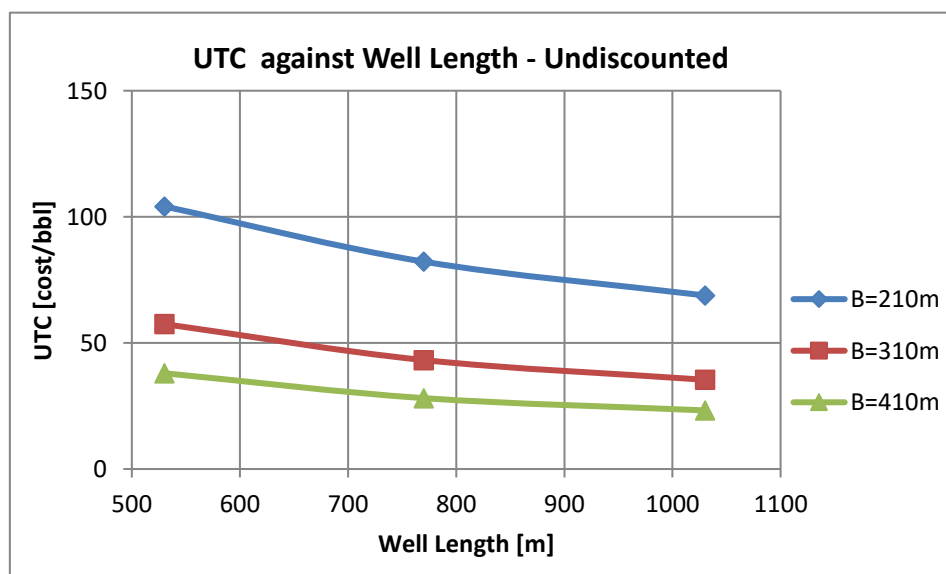
Figure 93: Unit technical cost versus well length – undiscounted.

In Figure 92, it can be seen that the discounted UTC reduces with increasing well length for all the three distances (210 m, 310 m and 410 m). However, the discounted UTC of the green curve with 410 m well distance upon declining until a well length of 770 m, the curve increases slightly again at the well length of 1030 m. It can therefore be assumed that the discounted UTC declines until it reaches a minimum at a certain well length, from where it might increase again, if the well length increases further. Thus, the optimum well length in relation to discounted UTC is this reversal point. Disintegrating the UTC into its components, hence opex and capex, and plotting each against the well length should clarify which of these two parameters has the highest influence on this trend. Figure 94 and Figure 95 illustrate the UTC – capex and UTC – opex against the well lengths respectively.
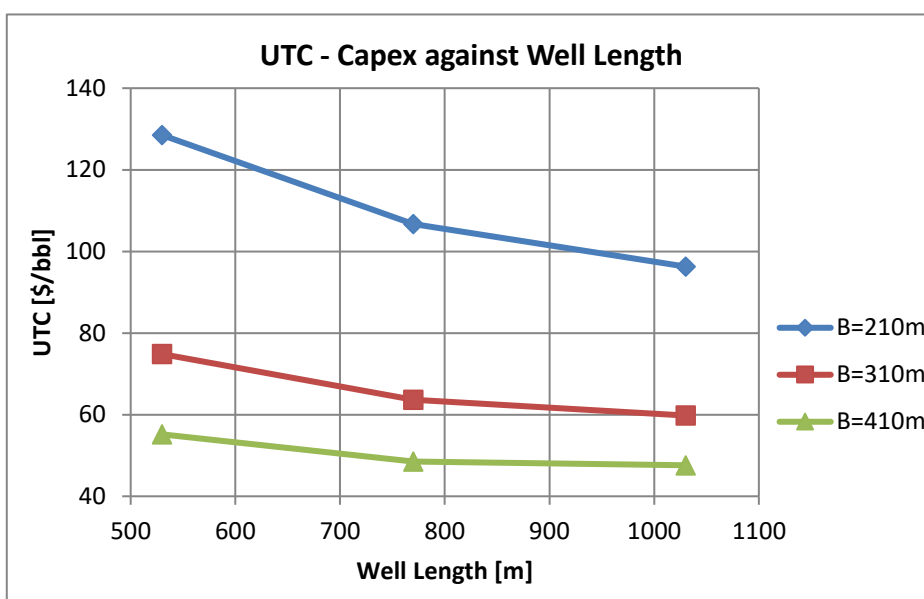
Figure 94: UTC - capex versus length of wells – discounted.
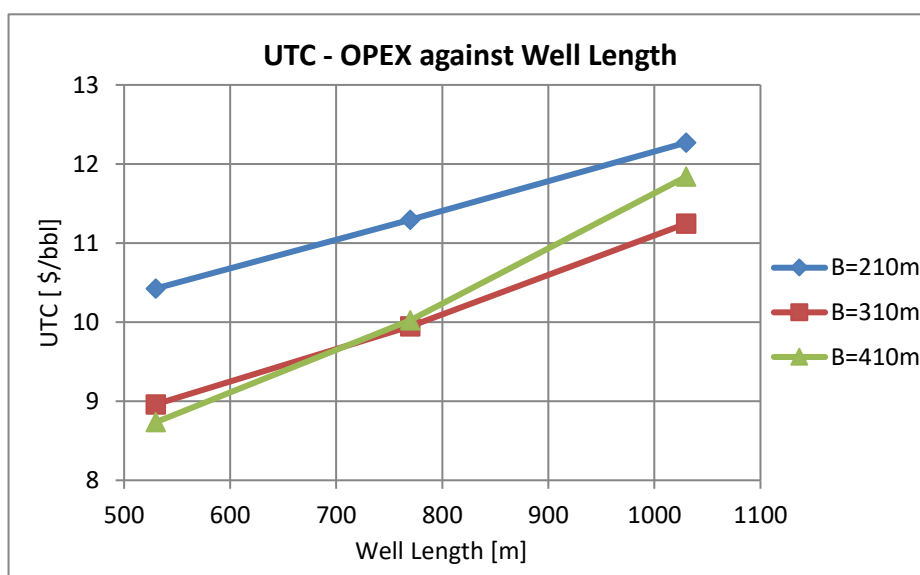
Figure 95: UTC - opex versus length of wells - discounted

Considering Figure 94, it can be seen that the discounted UTC – capex is in favour of drilling longer and larger spaced wells as the UTC declines with increasing well length and distance until the reversal point is reached. However, as can be seen in Figure 95 the discounted UTC - opex is in favour of drilling shorter wells. The magnitudes of the capex and opex UTC, reveal that, the drilling costs make up the highest cost factor with the best case (well length 1030 m and 410 m well spacing) around 47.60$/bbl whilst the best case of opex (well length 530 m and 410 m spacing) lies around 8.7$/bbl.

Chapter 8: Conclusion – Polymer Flooding in Horizontal Wells

Based on the results, observations and discussions on the polymer solution injection into horizontal wells with the aim of finding out an optimal well geometry with an optimum sweep efficiency, the following conclusions can be made:

The polymer injection in horizontal wells achieved lower injection pressures than verticals wells, making it possible to flood at higher injection rates under matrix conditions. The injection pressure is higher in polymer flooding than in water flooding in both, homogeneous and heterogeneous models and increases with increasing polymer concentration. However, the injection pressure distribution of polymer solutions are higher in heterogeneous models than in homogeneous ones depending on the average permeability of the heterogeneous models.

Increasing the polymer concentration increases the viscosity of the polymer solution. This leads to higher displacement efficiency however; the limiting factor is the injection pressure, which can exceed the formation parting pressure at higher polymer concentrations. Thus higher polymer concentrations should be preferred over lower ones if there are no injectivity problems.

In the heterogeneous models, the models with their major axis of correlations lengths lying parallel to the wells have better sweep efficiency in both water and in polymer flooding. The models with their major axis of correlation lengths perpendicular to the wells had poor sweep efficiency in both water flooding and in polymer flooding. The higher incremental oil recovery in the models with their major axis of correlations length parallel to the wells suggest that, the wells should be placed parallel to the geological channels to achieve higher recovery.

Incremental oil scales linearly with the chemically affected reservoir volume (CARV). Horizontal wells with larger spacing have shown to achieve higher incremental oil than smaller well spacing because of the faster increase in the elliptical drainage area of the larger spacing compared to that of the smaller well spacing. Therefore, larger horizontal well spacing should be preferred over smaller well spacing however, at limited spacing, smaller spacing with longer wells should be preferred.

The utility factors calculated decrease with increasing CARV however, stays approximately constant within a configuration set which would suggest, that for the same utility factor of a set of configuration, the shorter wells should be preferred to longer wells in the case of homogeneous reservoirs. The discounted unit technical costs on the other hand imply that, longer wells with larger distances should be preferred over shorter smaller wells until the reversal point is reached.

References

Ahmed, T.H., 2006. Reservoir engineering handbook, 3rd ed. Gulf Professional; Elsevier/Gulf Professional, Oxford, Amsterdam, London, 1377 pp.

Ahmed, T.H., 2010. Reservoir engineering handbook, 4th ed. Gulf Professional Pub, Amsterdam, Boston, xvi, 1454.

Ahmed, T.H., Meehan, D.N., 2012. Advanced reservoir management and engineering, 2nd ed. Gulf Professional Pub, Amstedam, Boston, MA, 1 online resource (ix, 702.

Bragg, J.R., Maruca, S.D., Gale, W.W., Gall, L.S., Wernau, W.C., Beck, D., Goldman, I.M., Laskin, A.I., Naslund, L.A., 1983. Control of Xanthan-Degrading Organisms in the Loudon Pilot: Approach, Methodology, and Results. 10.2118/11989-MS.

Clemens, T., Abdev, J., Thiele, M.R., 2010. Improved Polymer-Flood Management Using Streamlines. 10.2118/132774-MS.

Clemens, T., Deckers, M., Kornberger, M., Gumpenberger, T., Zechner, M., 2013. Polymer Solution Injection - Near Wellbore Dynamics and Displacement Efficiency, Pilot Test Results, Matzen Field, Austria. 10.2118/164904-MS.

Craft, B.C., Hawkins, M.F., Terry, R.E., 1991. Applied petroleum reservoir engineering, 2nd ed. Prentice Hall, Englewood Cliffs, N.J., 226 pp.

Dickson, J.L., Leahy-Dios, A., Wylie, P.L., 2010. Development Of Improved Hydrocarbon Recovery Screening Methodologies. 10.2118/129768-MS.

Emami Meybodi, H., Kharrat, R., Ghazanfari, M.H., 2008. Effect of Heterogeneity of Layered Reservoirs on Polymer Flooding: An Experimental Approach Using 5-Spot Glass Micromodel. 10.2118/113820-MS.

Garland, T.M., 1966. Selective Plugging of Water Injection Wells. Journal of Petroleum Technology 18 (12), 1550–1560. 10.2118/1431-PA.

Goodwin, J.W., Hughes, R.W., 2008. Rheology for chemists: An introduction / Jim W. Goodwin, Roy W. Hughes, 2nd ed. RSC Publishing, Cambridge, 277 pp.

Green, D.W., Willhite, G.P., 1998. Enhanced oil recovery. Society of Petroleum Engineers, Richardson, Tex.

Gumpenberger, T., Deckers, M., Kornberger, M., Clemens, T., 2012. Experiments and simulation of the near-wellbore dynamics and displacement efficiencies of polymer injection, Matzen Field, Austria. 10.2118/161029-MS.

HEINEMANN, Z.E., Mittermeir, G., 2013. FLUID FLOW IN POROUS MEDIA, Leoben, 206 pp.

Irgens, F., 2014. Rheology and non-Newtonian fluids. Springer, Cham, New York, ix, 190 pages.

Joshi, S.D., 1991a. HORIZONTAL WELL TECNOLOGY, 287 pp.

Joshi, S.D., 1991b. Thermal Oil Recovery With Horizontal Wells (includes associated papers 24403 and 24957). Journal of Petroleum Technology 43 (11), 1302–1304. 10.2118/21751-PA.

Joshi, S.D., Ding, W., 1996. Horizontal Well Application: Reservoir Management. 10.2523/37036-MS.

Khan, K., 2015. Fluid mechanics and machinery. Oxford University Press, New Delhi, 1 online resource (1 volume).

Lacy, S., Ding, W., Joshi, S.D., 1992. Horizontal Well Applications and Parameters for Economic Success. 10.2118/23676-MS.

Lake, L.W., Johns, R.T., Rossen, W.R., Pope, G.A., 2014. Fundamentals of enhanced oil recovery. Society of Petroleum Engineers, Richardson Texas, x, 479 pages.

Littmann, W., 1988. Polymer flooding, 223 pp.

Mott, R.L., Untener, J.A., 2015. Applied fluid mechanics. Pearson, Boston, xv, 531 pages.

Newendorp, P.D., Schuyler, J.R., 2014. Decision analysis for petroleum exploration, 3rd ed. Planning Press, Aurora, Colorado, xx, 567.

Osswald, T.A., Rudolph, N., 2015. Polymer rheology: Fundamentals and applications. Hanser Publications, Cincinnati, 225 pp.

Poellitzer, S., Florian, T., Clemens, T., 2009. Revitalising a Medium Viscous Oil Field by Polymer Injection, Pirawarth Field, Austria. 10.2118/120991-MS.

Pope, G.A., 1980. The Application of Fractional Flow Theory to Enhanced Oil Recovery. Society of Petroleum Engineers Journal 20 (03), 1–15. 10.2118/7660-PA.

Ramirez, B., Kazemi, H., Ozkan, E., Al-Matrook, M., 2007. Non-Darcy Flow Effects in Dual-Porosity, Dual-Permeability, Naturally Fractured Gas Condensate Reservoirs. 10.2523/109295-MS.

Reiss, L.H., 1980. The reservoir engineering aspects of fractured formations. Technip; London : Marketed and distributed by Graham & Trotman, Paris, 110 pp.

Saavedra, N.F., Reyes, D.A., 2001. Drainage Area for Horizontal Wells With Pressure Drop in the Horizontal Section. 10.2523/69431-MS.

Schlumberger, 2015. Eclipse - Industry Reference Reservoir Simulator: Reference Manual Version 2015.2.

Sheng, J., 2011. Modern chemical enhanced oil recovery: Theory and practice / James Sheng. Gulf Professional Pub, Amsterdam, Boston, Mass., 632 pp.

Sieberer, M., Jamek, K., Clemens, T., 2016. Polymer Flooding Economics, from Pilot to Field Implementation at the Example of the 8 TH Reservoir, Austria. 10.2118/179603-MS.

Sorbie, K.S., 1991. Polymer-Improved Oil Recovery. Springer Netherlands; Imprint; Springer, Dordrecht, 1 online resource (XII, 359.

Taber, J.J., Martin, F.D., Seright, R.S., 1997. EOR Screening Criteria Revisited - Part 1: Introduction to Screening Criteria and Enhanced Recovery Field Projects. SPE Reservoir Engineering 12 (03), 189–198. 10.2118/35385-PA.

Taber, J.J., Seright, R.S., 1992. Horizontal Injection and Production Wells for EOR or Waterflooding. 10.2118/23952-MS.

Tadros, T.F., 2010. Rheology of dispersions: Principles and applications / Tharwat F. Tadros. Wiley-VCH, Weinheim, 218 pp.

van Golf-Racht, T.D., 1982. Fundamentals of fractured reservoir engineering. Elsevier Scientific, Amsterdam, Oxford, 729 pp.

Vlachopoulos, J., 2016. Fundamenmtals of Fluid Mechanics. POLYDYNAMICS INC, Dundas, ON, CANADA, 815 pp.

Wang, Y., Seright, R. Correlating Gel Rheology With Behavior During Extrusion Through Fractures.

Warren, J.E., Root, P.J., 1963. The Behavior of Naturally Fractured Reservoirs. Society of Petroleum Engineers Journal 3 (03), 245–255. 10.2118/426-PA.

Zechner, M., Buchgraber, M., Clemens, T., Gumpenberger, T., Castanier, L.M., Kovscek, A.R., 2013. Flow of Polyacrylamide Polymers in the Near-Wellbore-Region, Rheological Behavior within Induced Fractures and Near-Wellbore-Area. 10.2118/166085-MS.

Chapter 9: Appendices

Appendix A – Moody Diagram
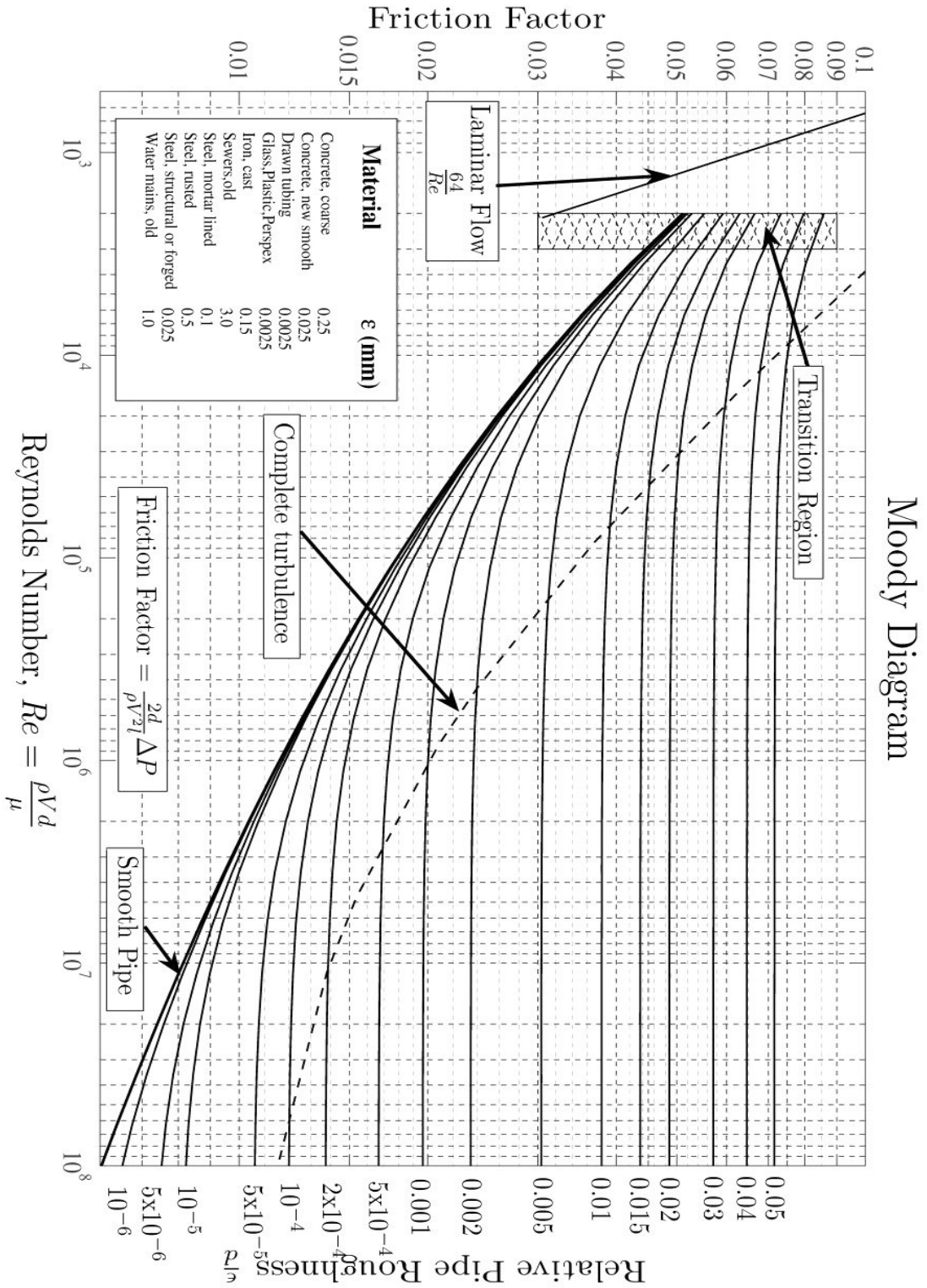
Figure 96: Moody Diagram (Moody, 1944)

Appendix B – High Permeability Contrast Models
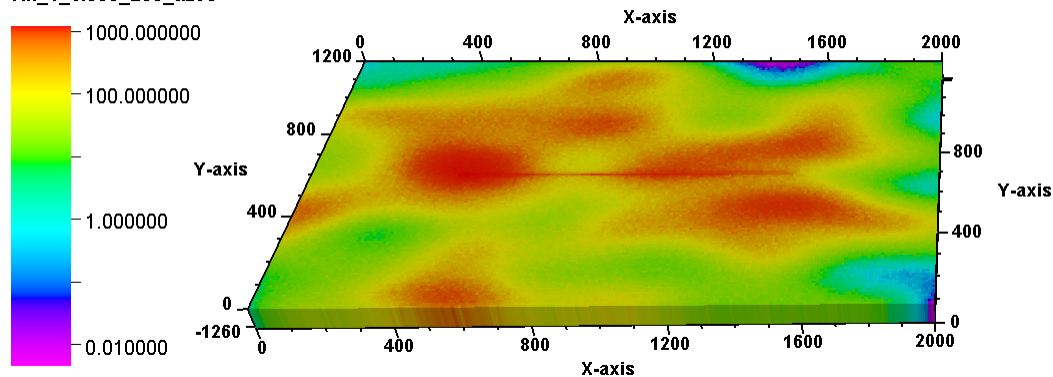
Figure 97: Heterogeneous Model – CL500_250_AZ90
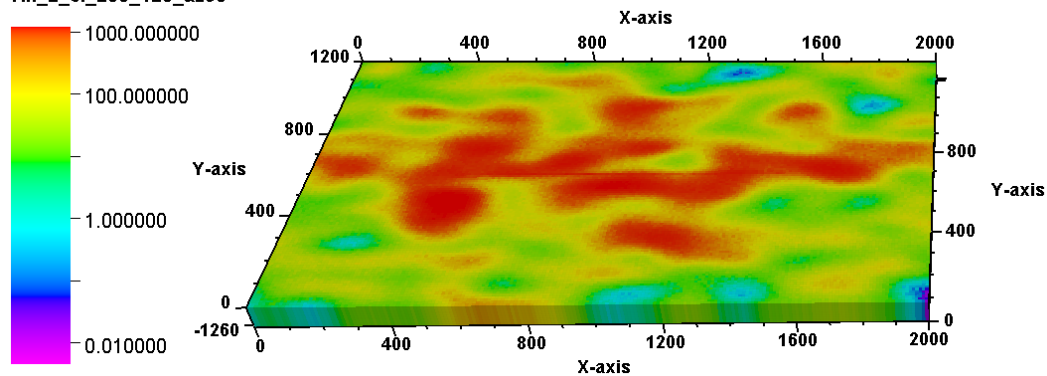
Figure 98: Heterogeneoous Model - CL250_125_AZ90
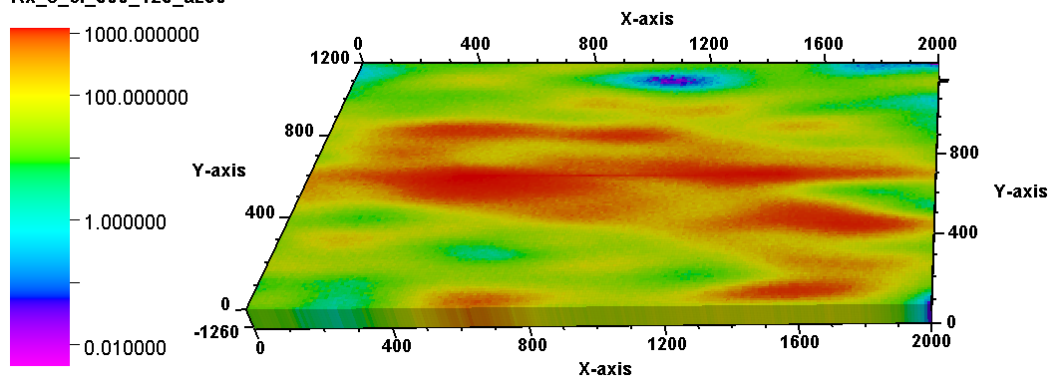
Figure 99: Heterogeneous Model - CL500_125_AZ90
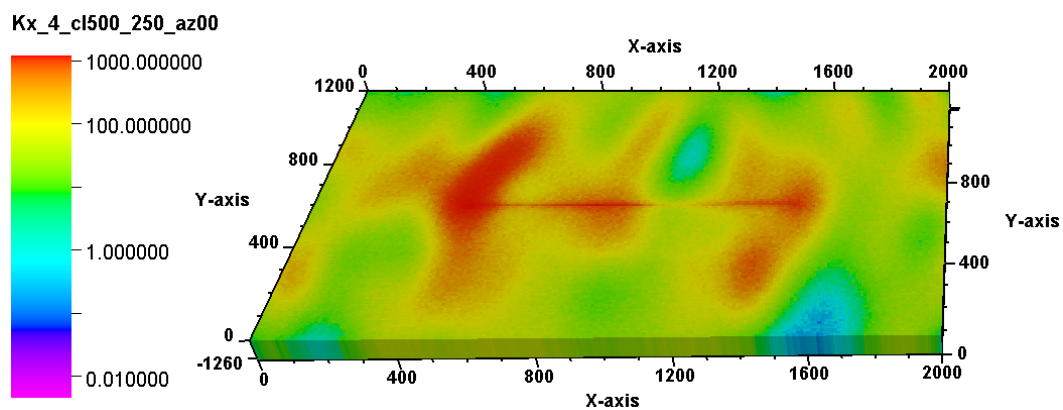
Figure 100: Heterogeneous Model - CL500_250_AZ00
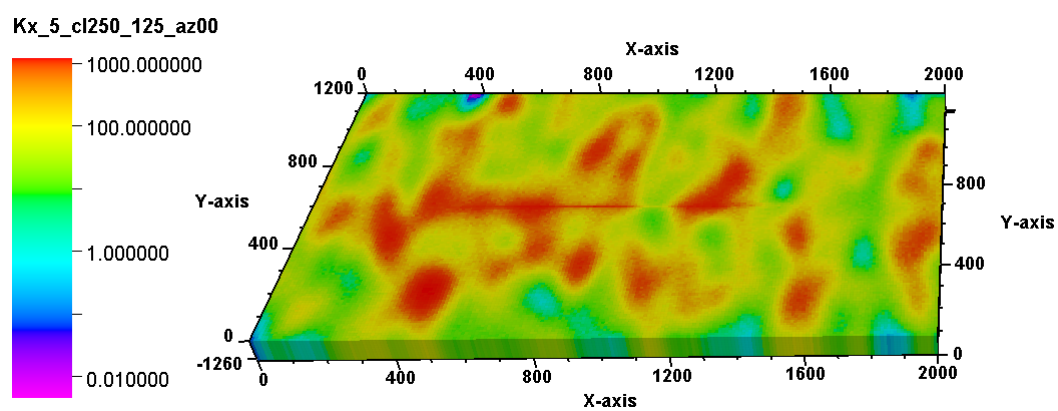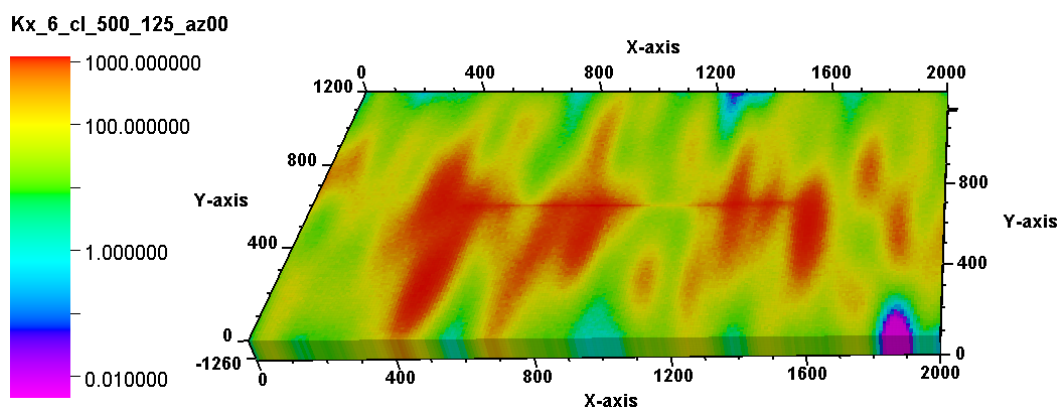

Figure 101: Heterogeneous Model - CL250_125_AZ00
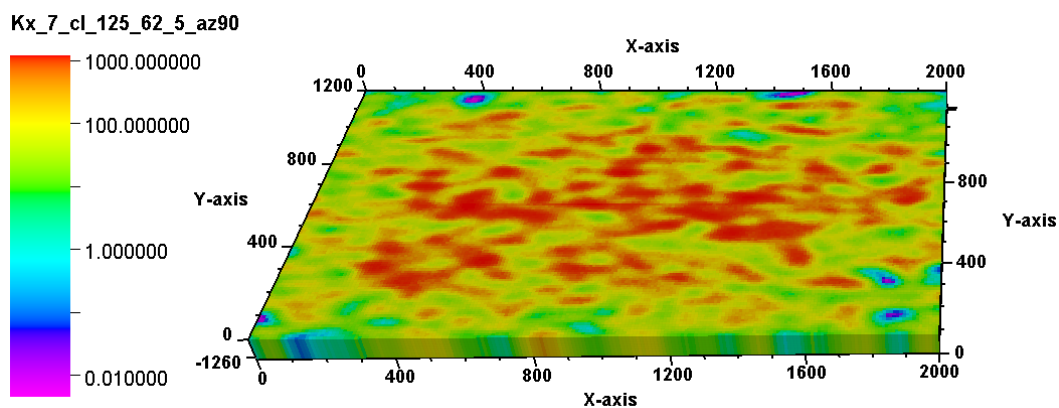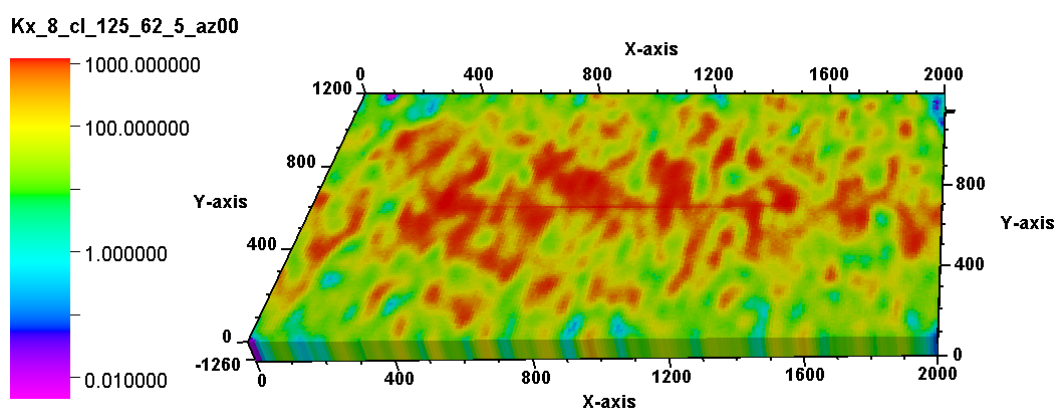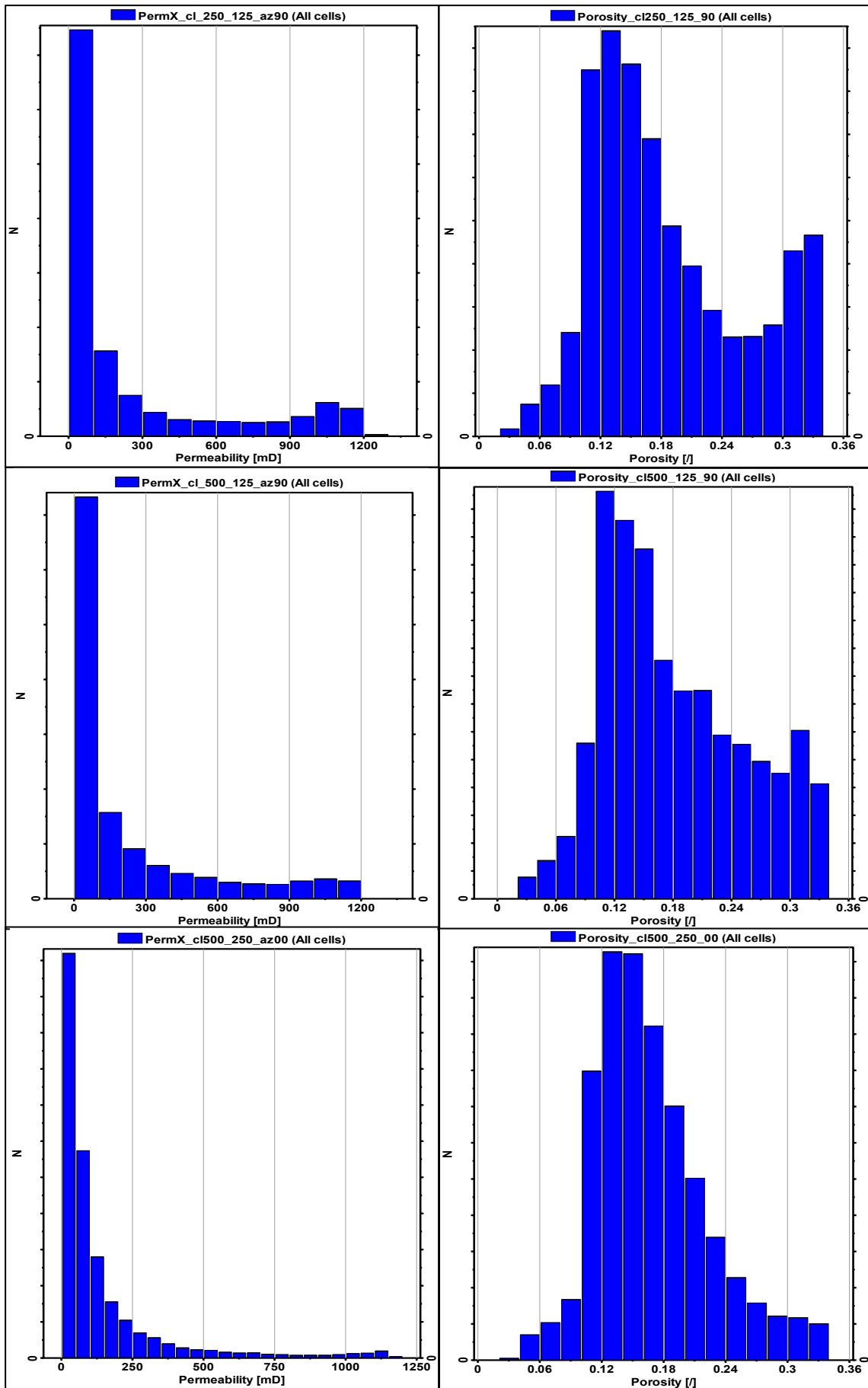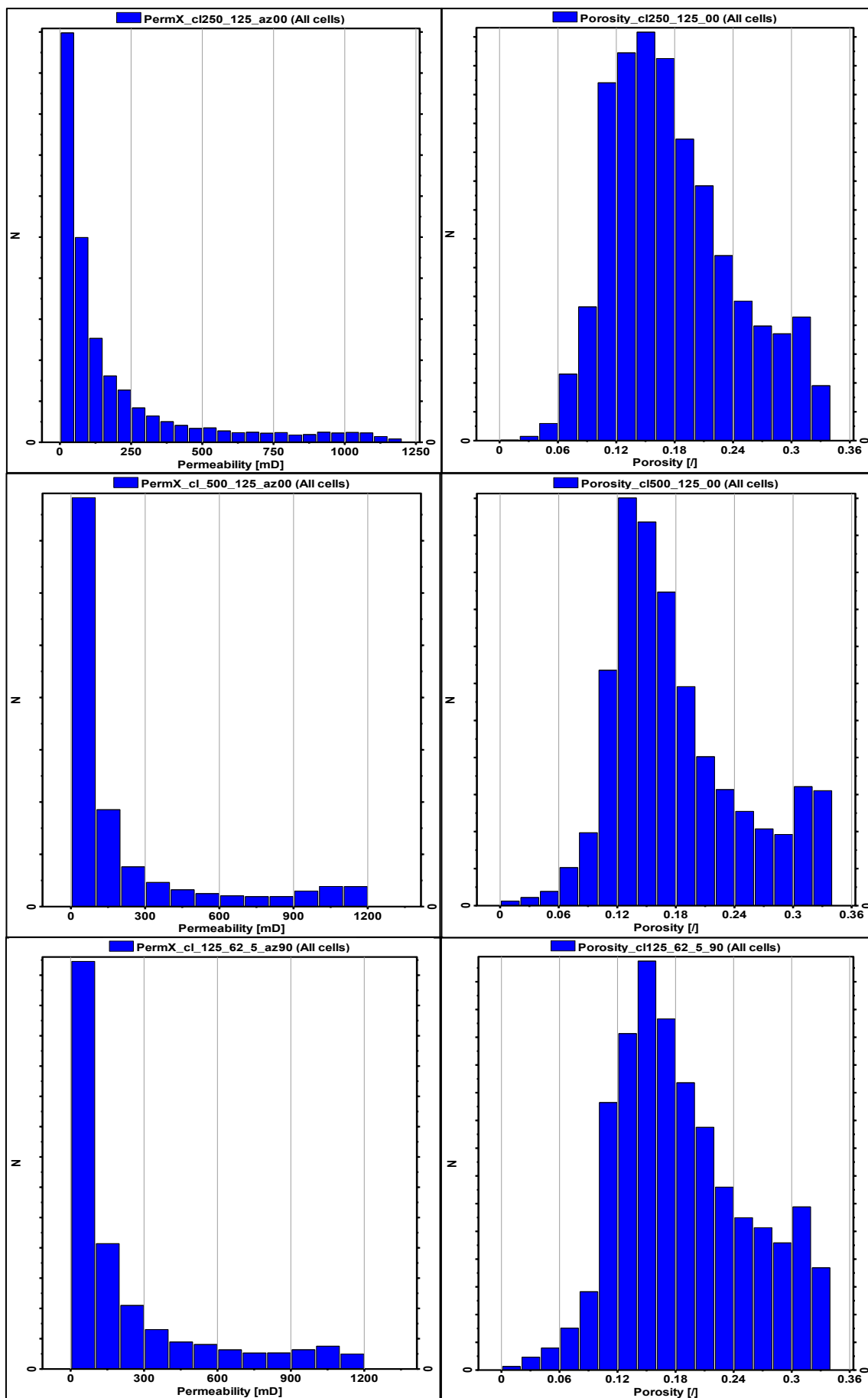

Figure 102: Heterogeneous Model - CL500_125_AZ00

Figure 103: Heterogeneous Model - CL125_62.5_AZ90

Figure 104: Heterogeneous Model - CL125_62.5_AZ00

Appendix C – Permeability and Porosity Histograms
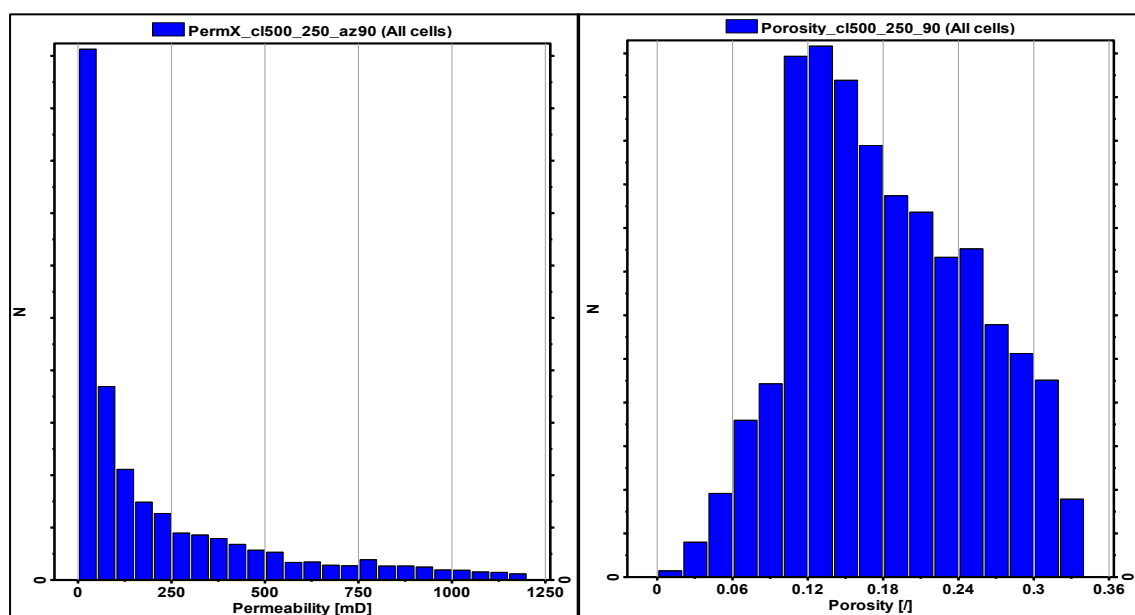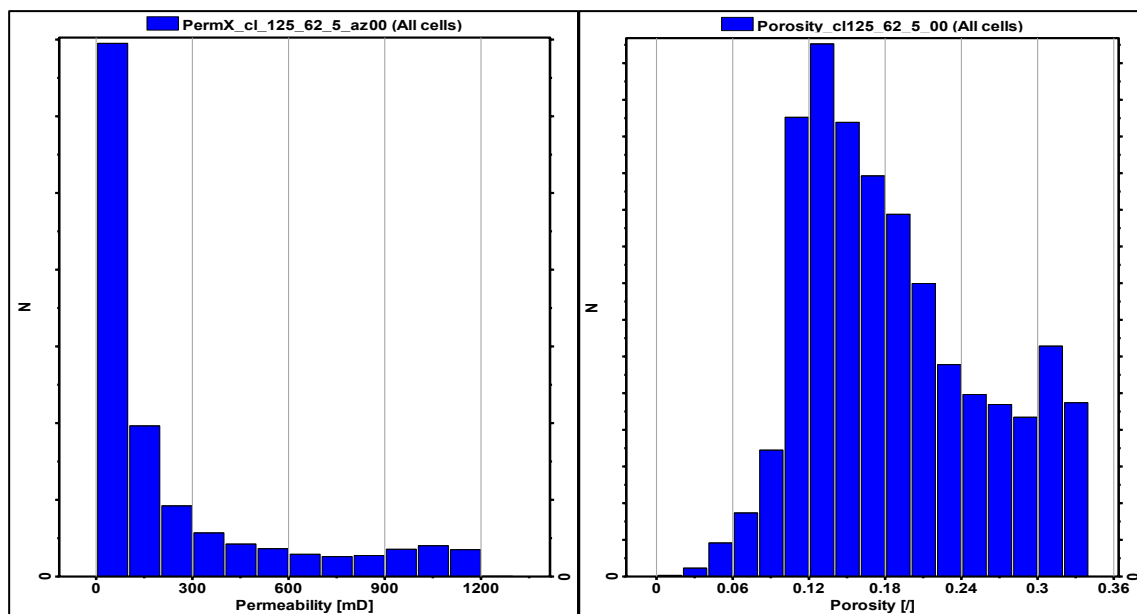
Figure 105: Permeability and porosity distribution of the heterogeneous models

Appendix D – High Permeability Contrast – Property Results
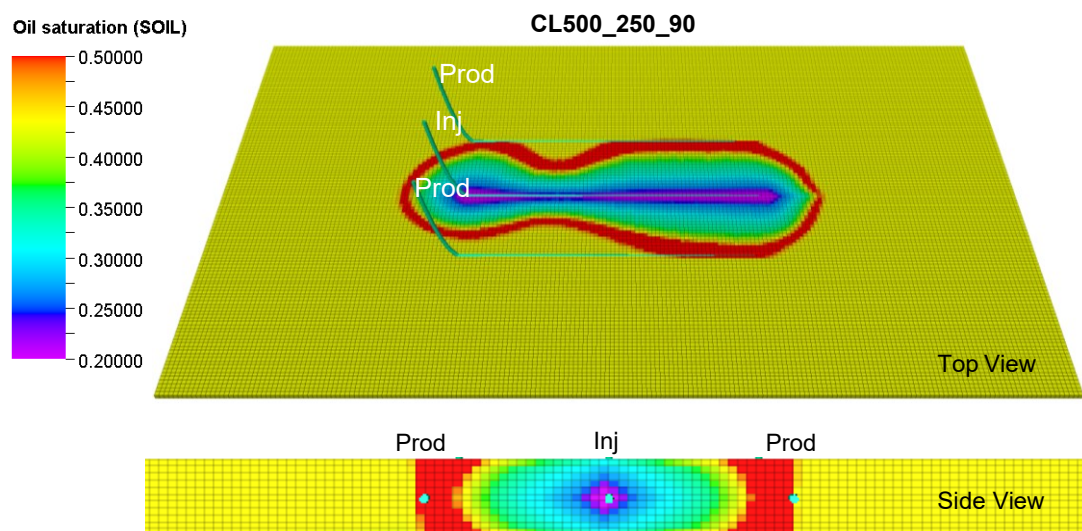
Figure 106: Oil saturation distribution, Hori_10 – polymer solution - 2022
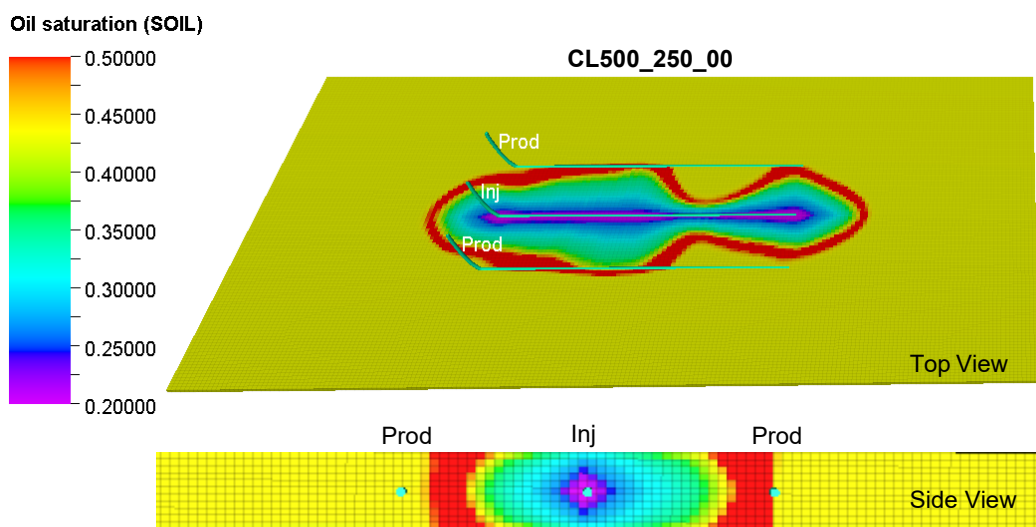
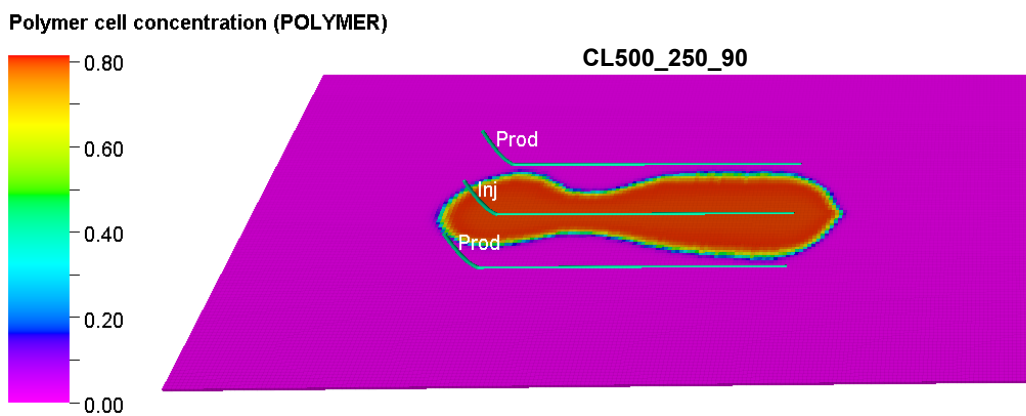Figure 107: Oil saturation distribution, Hori_10 – polymer solution - 2022

Figure 108: Polymer cell concentration, Hori_10 – polymer solution - 2022
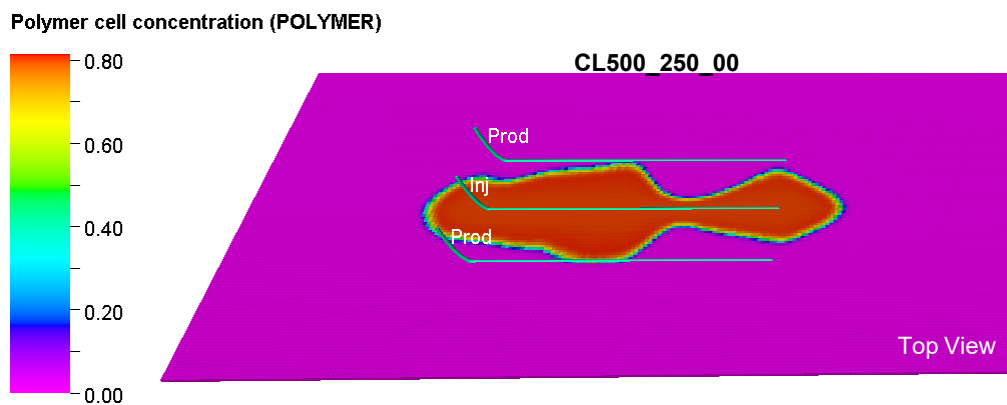
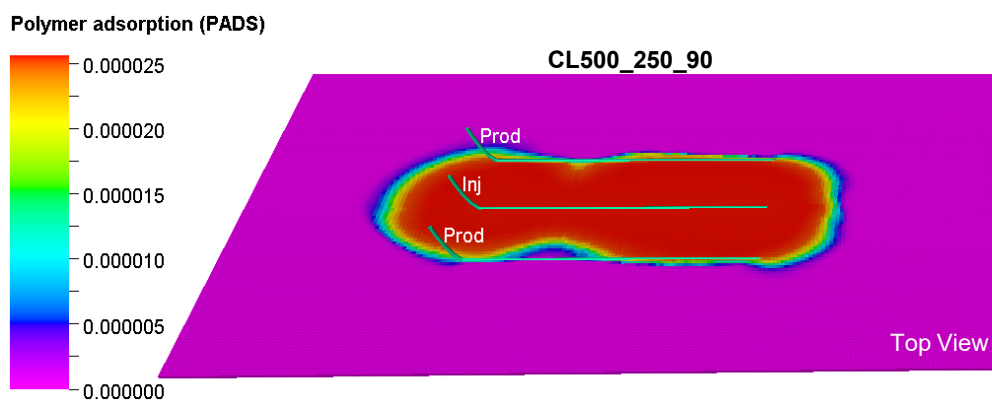Figure 109: Polymer cell concentration, Hori_10 - polymer solution - 2022

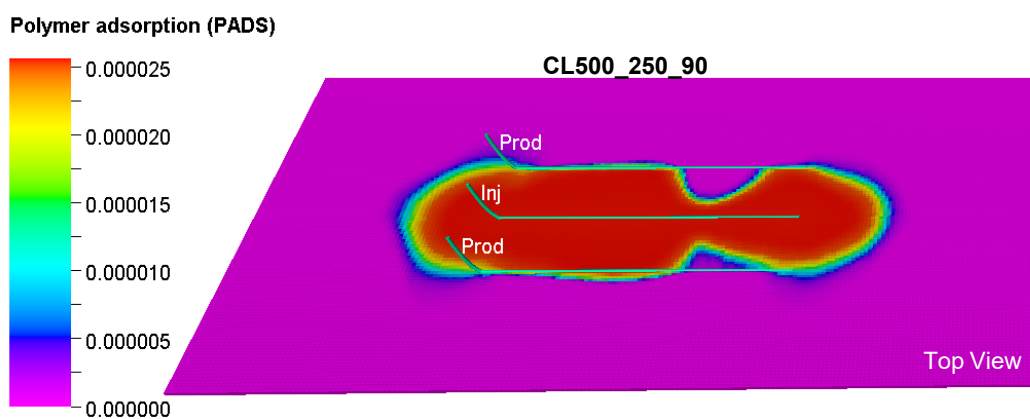Figure 110: Polymer adsorption, Hori_10 – CL500_250_AZ90 - 2042

Figure 111: Polymer adsorption, Hori_10 – CL500_250_AZ00 - 2042